The Structural Evolution of the MoO_3(010) Surface during Reduction and Oxidation Reactions.

Richard L. Smith
Department of Materials Science and Engineering
Carnegie Mellon University
Pittsburgh, PA 15213-3890

May 13, 1998

Advisor: Professor Gregory S. Rohrer

Submitted to Carnegie Institute of Technology in partial fulfillment of the requirements for the degree of

Doctor of Philosophy
in
Materials Science and Engineering

Abstract

Scanning probe microscopy (SPM) has been used to study the surface structure of selected binary molybdenum oxides and the structural evolution of the MoO_3(010) surface during gas phase redox reactions. These observations have been used to develop an improved understanding of the relationship between the structure and reactivity of molybdenum trioxide. The structural evolution of the MoO_3(010) surface was studied as a function of time, temperature, and gas phase atmosphere during the following reactions: reduction with H_2, CO, and N_2 gases with known humidities ($200 \leq T \leq 500$ ˚C), oxidation of virgin and H_2-reduced surfaces at 400 ˚C with static air at ambient humidity, and reactions with air-N_2-alcohol (methanol, ethanol, 2-propanol) mixtures with air:N_2 ratios ranging from 0:100 to 100:0 ($200 \leq T \leq 400$ ˚C). The influence of undercoordinated surface Mo sites on the chemisorption of methanol was explored by studying the structural evolution of MoO_3(010) surfaces with different morphologies and site populations during reactions with MeOH-N_2 mixtures between 300 and 330 ˚C.

The study of the binary molybdenum oxide cleavage surfaces - α-MoO_3(010), $Mo_{18}O_{52}$(100), Mo_8O_{23}(010), and η-Mo_4O_{11}(100) - demonstrated that the atomic scale contrast in SPM images of anisotropically bonded oxides can often be interpreted based on a simple model that assumes cleavage occurs at the longest, weakest bonds normal to the surface. The SPM contrast signatures of two types of surface/crystallographic shear (CS) plane intersections in molybdenum suboxides have been identified. When the CS planes have a component of shear normal to the surface, as in $Mo_{18}O_{52}$(100), the CS planes are marked by a step at the interface. In Mo_8O_{23}(010), the CS planes intersect the surface such that the shear lies entirely in the surface plane and line of intersection is marked by dark contrast in STM images.

During reduction in the presence of H_2O above 350 ˚C, the MoO_3(010) surface is modified by the introduction of two defects: CS planes and surface pits. At temperatures greater than 350 ˚C, atmospheric water impurities catalyze the volatilization of MoO_3(010) where strain is concentrated in the crystal. Under oxidizing conditions, volatilization is confined to step edges and dislocation/surface intersections. In reducing atmospheres, CS planes provide an abundant source of strain and volatilization leads to the nucleation and growth of a large population of surface pits bounded by {101}. These processes are facilitated by volatile Mo oxide-hydroxides that form when MoO_3 reacts with H_2O. Reoxidation of reduced surfaces in air proceeds more slowly than reduction in

10%H_2-N_2 at the same temperature. For example, at 400 ˚C, it takes up to 60 min to annihilate the CS planes created in only 8 min during reduction. The observed difference in reaction kinetics is probably due to the difference in the chemical potential gradient during the two processes. When pitted surfaces are oxidized above 350 ˚C, the pits grow and their bounding edges eventually reorient to <001> and <100>. As a result, thermal treatments can be used to alter and control the morphology of the MoO_3(010) surface.

During gas phase reactions with N_2-alcohol mixtures ($200 \leq T \leq 400$ ˚C), MoO_3 intercalates H and protonation leads to the precipitation of a well known hydrogen molybdenum bronze, H_xMoO_3 ($0.23 \leq x \leq 0.4$). The acicular precipitates of H_xMoO_3 form topotactically and are aligned along the <203> directions of the MoO_3(010) surface plane. Because the intercalating H is formed during the initial dissociative chemisorption of the alcohol, the H_xMoO_3 density provides a quantifiable indicator of the chemisorption process. Identical H_xMoO_3 precipitates form when MoO_3(010) surfaces are reacted with atomic H produced by spill over from supported Pt particles. During reactions with N_2-MeOH mixtures ($300 \leq T \leq 330$ ˚C), H_xMoO_3 precipitates preferentially at {h0l} planes which bound the MoO_3(010) surface. As the density of {h0l} surface sites is increased (by introducing pits), more hydrogen is intercalated during the reaction. The observed increase is greater than can be explained by changes in the absolute surface area of the samples or by potential increases in the surface vacancy concentration. This result, taken together with the observation that H_xMoO_3 precipitates emerge from intentionally introduced and native {h0l} surfaces, leads to the conclusion that the undercoordinated surface Mo afforded by {h0l} planes dominate MeOH chemisorption at typical reactor temperatures.

The morphology of the MoO_3(010) surface is modified during the partial oxidation of methanol. During reactions with air-N_2-MeOH mixtures above 250 ˚C, closed step loops, bounded by undercoordinated surface Mo sites, nucleate and grow as the MoO_3(010) surface volatilizes in a nearly layer-by-layer fashion. The density and crystallography of the new surface sites depend on the composition of the gas mixture in the reactor. In air rich environments, the step loops have a rectangular shape and are elongated along <001>. At any instant, only the top-most one or two {010} layers are affected by the process. As the concentration of O_2 in the feed is reduced, the shape evolves to elongated triangles oriented along <100> and the loops exist on multiple layers simultaneously. During these reactions, the density of undercoordinated surface Mo sites can increase from $1 \times 10^{10}/cm^2$ to more than $1.5 \times 10^{12}/cm^2$. The possible roles that this process may play in the observed structure sensitivity of MeOH oxidation on MoO_3 are discussed.

Acknowledgments

I would first like to thank my advisor, Greg Rohrer, for the opportunity to conduct this research and the constant support and attention that he has given me over the past six years. I really can't thank Greg enough for the guidance, advice, inspiration, and friendship he has given me. The time and effort of my thesis committee, Andrew Gellman, Prashant Kumta, and Tony Perrotta, is gratefully acknowledged. I owe additional thanks to Dr. Kumta for his guidance and the use of his lab facilities and to Tony for the support and opportunities he has provided. The financial support of the NSF, Alcoa, and DuPont and the assistance of the staff of the MSE department are also gratefully acknowledge.

I can't begin to thank all of the people at CMU who have provided friendship, assistance, and stimulating discussions. Mandyam Sriram, Scott Weil, and Dave "The Dog" Saylor, have been a constant source of all of these. Sriram and Dave's willingness to venture to the PHI-bar or to Joe's has also been much appreciated. Numerous people have made life at CMU enjoyable and memorable. Among them, Trevor Smith, Alex Rutkowski, Luana Iorio, Chun-Chieh "Jimmy" Chang, Eric Ott, Bill Slye, Ellen Cerreta, Bahri Ozturk, Jennifer Giocondi, Jason Wolf, Weier Lu, and Jin Yong Kim. I would especially like to thank "Sweet, Sweet" Shiela Woodard for her constant friendship, support, attention, and patience.

Finally, I would like to thank my family for the love, support, and guidance they have given me through out my life. Thank you - Mom, Dad, Kristen, Amanda, Bernie, Grandma and Grandpap Smith, Grandma and Grandpap O'Leary, and all of the O'Learys, Smiths, Fehls, Dahars, and Bordognas.

Table of Contents

List of Figures

List of Tables

1

Introduction

1.1 Motivation

Few bulk or specialty organic chemicals are produced without the aid of heterogeneous catalysts and, in most cases, commercially viable yields can only be attained through catalytic routes [1]. In selective oxidation reactions, a solid catalyst is used to facilitate the oxidation of a hydrocarbon to a less saturated organic product. Although oxidized products are always thermodynamically favored, by using a catalyst and a low reaction temperature, the kinetics of the conversion can be controlled such that the organic is only partially oxidized rather than being converted to water and carbon oxides (deep oxidation). Industrially important intermediates produced through partial oxidation routes include tetrahydrofuran, acrylonitrile, formaldehyde, maleic anhydride and most of the monomers from which synthetic fibers and plastics are produced [2]. The complex multicomponent catalysts used for these reactions are almost exclusively transition metal oxides [3,4].

While experimental results have demonstrated that the catalytic properties of many transition metal oxides are surface structure sensitive [4-7], reliable structure-reactivity relationships to account for these observations have not been established. The development of structure-property relationships rests on the ability to both accurately measure properties and adequately describe structure. Increasingly, it is apparent that the greatest obstacle to establishing structure-reactivity relationships is developing a complete and reliable description of the catalyst's surface structure [4]. Attempts to relate catalytic properties directly to one aspect of the surface, such as composition or termination, have largely been unsuccessful. In light of the role defects are now thought to play in the process, these failures are not so surprising [2-5].

This thesis is motivated by the current lack of accurate and reliable descriptions of the surface structures of model transition metal oxide catalysts. The necessary description must specify not only the periodic components of the surface (i.e., composition and atomic structure), but also the population and configuration of

nonperiodic defects at the interface. Steps, point defects, and the intersections of extended defects with the surface can all potentially influence surface properties and, in some cases, may be the source of the active sites [2-5]. Because few real surfaces are atomically flat, surface morphology will influence the population and geometry of the available reaction sites. Finally, it must be recognized that while the catalyst is in service, the conditions within the reactor may lead to changes in the surface structure. These can include gross microstructural changes (such as, particle coarsening, faceting, and volatilization) as well as more subtle modifications on the atomic scale (changes in stoichiometry and defect structure).

1.2 Objectives

The objective of this research is to develop a detailed description of the surface structure of molybdenum trioxide and its morphological evolution during redox reactions. MoO_3 has been studied as a model partial oxidation catalyst in the past and its reactivity has been characterized by a number of groups. However, while a limited amount of bulk structural data exists, the dynamics of the surface structure have been overlooked entirely in previous studies. Scanning probe microscopy (SPM) is ideally suited to provide the desired information and is the principal experimental technique used in this study.

The first goal of this work was to characterize the microscopic and atomic scale surface structure of MoO_3 and the molybdenum suboxides. Because oxygen stoichiometry compensating defects are thought to be continuously created and annihilated during the catalytic process [6], the second goal was to investigate surface structural evolution during the reduction and reoxidation cycle. The third goal was to identify the structural changes that accompany reactions with alcohols. The next goal was to test the influence of undercoordinated surface sites on alcohol oxidation. The final goal was to determine how the surface structure of MoO_3 evolves during the partial oxidation of methanol and to correlate the catalyst's surface structure with the reactor environment (temperature and gas composition).

1.3 Approach

While most industrial catalysts are used in particulate form, fine particles and polycrystalline samples are not convenient for controlled SPM studies. Single crystal samples, on the other hand, are ideal because they provide relatively flat, reproducible surfaces. Furthermore, surface crystallography is unambiguous. There is every reason to believe that an appropriate model catalyst can be selected and studied with SPM so that our observations can be extended to real catalysts. For example, MoO_3 is typically used

in the form of a bulk powder with relatively large (100 μm) crystallites and, therefore, the use of single crystal samples in this case is reasonable. Most of the observations described here are of the {010} cleavage surfaces of large single crystals grown by chemical vapor transport. However, additional experiments have been performed on the growth surfaces of crystals grown by sublimation, a technique which has been employed in the past to synthesize MoO_3 catalysts [7]. The influence of nonbasal surface orientations was examined indirectly by studying the {010} surfaces in the vicinity of the edges of the crystal or surface steps. Furthermore, controlled populations of morphological defects bounded by {h0l} (lateral) facets were introduced to the {010} surfaces with high temperature treatments.

The virgin surfaces were thoroughly characterized so that the modifications resulting from the reactions could be easily identified. The structural evolution of the MoO_3(010) surface was then studied as a function of time, temperature, and gas phase composition. The gas phase in a typical reactor is a complex, multicomponent mixture and a single component may initiate modifications in the catalyst's surface structure. For example, at a fixed temperature, the partial pressure of oxygen in the reactor will fix the equilibrium stoichiometry and defect structure of the catalyst. The experiments described here were designed to allow for the influence of individual constituents to be identified, as well as the effect of the overall reaction mixture.

1.4 Organization

The background information and previous work relevant to this thesis are presented in Chapter 2. In Chapter 3, the experimental techniques and procedures used are outlined. The results of SPM studies of the virgin cleavage surfaces of the molybdenum oxides are presented and discussed in Chapter 4. The evolution of the MoO_3(010) surface during the reduction and oxidation cycle is described in Chapter 5. In Chapter 6, the surface structural evolution of MoO_3 during reactions with N_2-alcohol mixtures is described. In Chapter 7, the results of experiments designed to determine how undercoordinated surface Mo sites influence reactions with methanol are presented and discussed. In Chapter 8, the evolution of the MoO_3(010) surface during the partial oxidation of methanol is characterized. Finally, Chapter 9 provides a summary of the major conclusions that can be drawn from this investigation and proposals for future study.

1.5 References

[1.] P. M. Rylander *in* "Catalysis Science and Technology", (J.R. Andreson and M. Boudart, eds.), p. 1, Springer Verlag, NY (1983).

[2.] J. Haber *in* "Solid State Chemistry in Catalysis", (R.K. Grasselli and J.F. Brazdil, Eds.), p. 1, American Chemical Society, Washington D.C. (1985).

[3.] D.B. Dadyburjor, S.S. Jewur, and E. Ruckenstein, *Catal. Rev.-Sci. Eng.* **19** (1979), 293.

[4.] A.W. Sleight *in* "Solid State Chemistry Compounds", (A.K. Cheetham and P. Day, eds.), p. 166, Oxford University Press, NY (1992).

[5.] M.A. Barteau, *J. Vac. Sci. Tech. A* **11** (1993) 2162.

[6.] W.E. Farneth, R.H. Staley, and A.W. Sleight, *J. Am. Chem. Soc.* **108** (1986) 2327.

[7.] J.M. Tatibouët and J.E. Germain, *J. Catal.* **72** (1981) 375.

2

Background and Review of Previous Work

2.1 Introduction

In this chapter, the background relevant to this thesis is presented. First, transition metal oxide catalysts and partial oxidation reactions are described. Next, the role that catalyst surface structure may play in partial oxidation reactions is addressed through the presentation of a few simple, experimental examples and a brief description of some of the models that have been developed to account for the observed structure sensitivity of oxidation reactions. The structural chemistry of the molybdenum oxides is then described. Finally, previous work pertaining to the partial oxidation of methanol (MeOH) on MoO_3 is reviewed with particular emphasis on previous studies of the bulk structural evolution of MoO_3 during redox processes.

2.2 Transition Metal Oxide Catalysts

2.2.1 Partial Oxidation Reactions

The catalysts employed most frequently for the partial (or selective) oxidation of hydrocarbons are transition metal oxides. The utility of these reactions rests on the catalyst's ability to controllably oxidize a hydrocarbon (for example, insert O, abstract H, or cleave C-C bonds) rather than completely oxidize (burn) it to water and carbon oxides. Because transition metal oxides are able to easily exchange oxygen, electrons, and protons with their surroundings, they are ideally suited for partial oxidation conversions and can catalyze both redox and acid-base type reactions. Examples of industrially important partial oxidation reactions include: propene oxidation to acrolein with Bi-Mo-O catalysts,

$$CH_2CHCH_3 + O_2 \rightarrow CH_2CHCHO + H_2O$$

butane oxidation to maleic anhydride with V-P-O catalysts,

$$n-C_4H_{10} + \frac{1}{2}O_2 \rightarrow C_4H_2O_3 + 4H_2O$$

and methanol oxidation to formaldehyde with Fe-Mo-O catalysts,

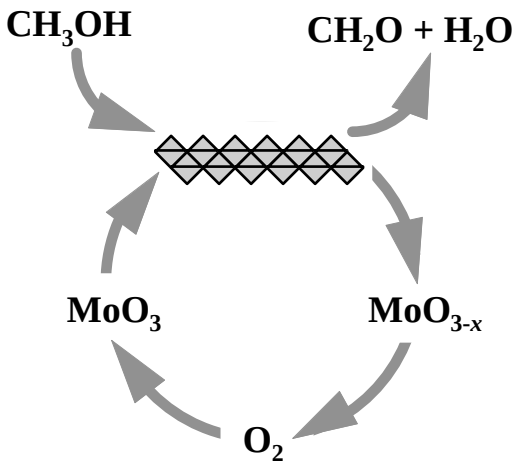

Figure 2.1 Schematic representation of the Mars - van Krevelen redox cycle for methanol oxidation on MoO_3. The oxygen used to abstract H, is lattice oxygen, O_O. The oxygen vacancies, V_O, created during the process are eliminated by reoxidation with gas phase O_2.

$$CH_3OH + \frac{1}{2}O_2 \rightarrow CH_2O + H_2O.$$

Contrary to the traditional definition of a catalyst, partial oxidation catalysts are modified as a result of the reaction they catalyze. This is because the oxygen that is inserted into the hydrocarbon or used to abstract hydrogen is lattice oxygen (O_O) from the surface of the catalyst. The removal of lattice oxygen leads to the creation of oxygen vacancies (V_O) and, therefore, the catalyst is left oxygen deficient (reduced) after an organic molecule is oxidized at the surface. To complete the redox cycle and regenerate the surface of the catalyst, oxygen sites are replenished through a combination of O diffusion from the bulk and reaction with gaseous O_2. In many cases, surface reoxidation and hydrocarbon oxidation are thought to occur at crystallographically distinct sites [1]. This concerted reduction and oxidation of the catalyst during partial oxidation reactions, known as the Mars - van Krevelen mechanism (cycle), is shown schematically in Fig. 2.1 [2].

There are alternate sources of oxygen in the reactor. Because O_2 is usually fed into the reactor along with the hydrocarbon, the organic can be oxidized homogeneously in the gas phase above the catalyst [3]. Other sources are electrophilic species, such as O_2^- and O^-, that may be chemisorbed on the oxide's surface [4]. These alternate mechanisms are usually only of secondary importance, however, and oxygen isotope studies have demonstrated that in most cases the oxygen incorporated into partial oxidation products is lattice oxygen from the surface of the catalyst [4,5].

2.2.2 Catalytic Properties

Three primary properties are used to describe and evaluate the performance of a catalyst: *activity*, *selectivity*, and *life* [6]. Activity (**a**) is a measure of the catalysts ability

to convert feedstocks to various products and is defined as the percentage (molar) of reactants (**R**) converted to products during the course of reaction:

$$\mathbf{a\ (\%)} = \frac{\mathbf{R_{converted}}}{\mathbf{R_{total}}} \times \mathbf{100}$$

Many different products can be formed during the partial oxidation of any given hydrocarbon. For example, propene may be oxidized (to various degrees) to form acrolein, acrylic acid, acetic acid, carbon monoxide, carbon dioxide, and/or water. For a partial oxidation catalyst to be useful, it must oxidize the feedstock predictably and consistently. Selectivity (**s**) is a measure of the catalyst's ability to produce a specific product (**i**) and is typically defined as the percentage of that product produced out of the total products ($\mathbf{n_{total}}$) of the reaction:

$$\mathbf{s_i\ (\%)} = \frac{\mathbf{n_i}}{\mathbf{n_{total}}} \times \mathbf{100}$$

While the definitions of activity and selectivity are straightforward, the interpretation of these quantities is not always unambiguous. For example, the activity of a catalyst will be a function of its surface area as well as the flow rate of the reactor. Therefore, care must be taken when comparing the catalytic properties of different materials, especially if their properties were not determined in the same manner or if they were determined under different experimental conditions. Finally, the life of the catalyst is the time period over which the catalyst maintains a sufficient level of activity and selectivity to be cost effective.

2.2.3 Intrinsic Structure and Properties of Oxide Catalysts

There are a number of properties and parameters intrinsic to a metal oxide that will contribute to its ability to catalyze partial oxidation reactions. Because charge transfer between reactant molecules and the catalyst is a necessary step in the redox process, the bulk and surface electronic structures of the catalyst are expected to play a role in the oxidation reaction. After oxygen atoms are removed from the surface, the vacancies left behind must be reoxidized before another reactant molecule can be converted [1,5]. Therefore, oxygen mobility within the lattice and at the surface can influence the reoxidation rate and possibly determine the overall reaction rate. Finally, it is important to recognize that the structure and chemistry of the oxide will influence all of these properties.

Because the reaction occurs at the surface of the catalyst, the structure and properties of the interface are perhaps more important than those of the bulk [1,7]. However, the mechanisms by which the surface structure of oxides influence their

catalytic properties are poorly understood. While there must be special locations on the surface where the desired reactions occur, the structure and chemical nature of these so-called 'active sites' are not well known. We assume, however, that both the chemical identity and geometric configuration of the atoms which terminate the surface are important.

2.2.4 Environmental Influences on the Catalyst.

While the catalyst may determine the products of the oxidation reaction, the environment established inside the reactor will influence the structure and properties of the oxide catalyst. For example, the partial pressure of oxygen and temperature will determine the equilibrium stoichiometry and defect structure of the oxide [8]. Although structural equilibrium might never be achieved within the lifetime of the catalyst, any change in the reactor environment will lead to changes in the stoichiometry and defect structure of the catalyst. These changes will be accompanied by changes in the structure (bulk and surface) and transport properties (charge and mass) of the solid. Because it is impossible to alter any of these properties or parameters without modifying the others, narrowly controlled studies on the role of any one parameter in the catalytic process are difficult to design.

While the stoichiometry and defect structure of the catalyst may reach a dynamic equilibrium once a steady state pO_2 is established, other processes may operate throughout the lifetime of the catalyst. For example, the active catalyst is often utilized in the form of fine particles and exposure to the high temperatures of the reactor will, invariably, lead to coarsening of theses particles. Other perpetual processes which are documented to occur include: volatilization of one or more components, 'coking' of the catalyst's surface, and poisoning due to the incorporation of impurities [1,6].

2.3 The Structure Sensitivity of Partial Oxidation Reactions

It is generally recognized that the catalytic properties of transition metal oxides are influenced by their surface structure and there is a considerable body of experimental evidence supporting this concept. Theoretical considerations, based on both simple and complex models, also provide compelling arguments for the existence of a link between structure and reactivity. However, the surface structures of even the simplest partial oxidation catalysts have yet to be described in detail. As a result, the underlying mechanisms of surface structure sensitivity have yet to be identified. What is meant by structure sensitivity and how important is it? In the following sections, structure sensitivity is addressed through the presentation of a few simple, experimental examples

and a brief discussion of some of the explanations developed to account for experimental observations.

2.3.1 Examples of Structure Sensitivity

Catalytic Anisotropy. The concept of catalytic anisotropy provides a simple example of the intimate role that surface structure may play in catalysis. It is based on the experimental observation that crystallites with the same composition, but different habits, behave differently during redox reactions. α-MoO_3 has been the subject of many investigations, and it has been proposed that the oxide exhibits catalytic anisotropy in a number of partial oxidation reactions [9-14]. Through the preparation of powdered catalysts with different crystallite morphologies and crystallographic distributions of the surface area, it has been demonstrated that the products formed during the oxidation of methane [14], propene [10,12,13], methanol [9] and butenes [11] can depend on which planes bound the MoO_3 crystallites. For example, experimental results indicate that during the oxidation of methane at 650 ˚C, {h0l} surfaces favor the partial oxidation of methane to formaldehyde while the basal {010} facets favor deep oxidation to CO_2 and H_2O [14]. Similarly, {100} facets are thought to be most selective for the oxidation of 1-butene to butadiene while the {010} facets favor deep oxidation [11]. Catalytic anisotropy has been demonstrated for a number of other oxides, including V_2O_5 [15] and ZnO [16].

Polymorph Reactivity. Experimental results have shown that oxide polymorphs can have different catalytic properties. An investigation of the surface chemistry of the layered α phase of MoO_3 and the synthetic, pseudo-cubic β phase has shown that the β phase has a significantly higher capacity for the chemisorption of alcohols [17]. It was also shown that the β phase was better able to dissociate these chemisorbed alcohols and partially oxidize them to aldehydes. Differences in polymorph reactivity have also been reported during the oxidation of butene and butadiene over the Mo_4O_{11} polymorphs [18] and the oxidation of methanol over the orthorhombic and hexagonal polymorphs of MoO_3 [19].

Supported Catalysts. Comparison of the catalytic properties of supported and unsupported oxide catalysts provides additional evidence for the structure sensitivity of partial oxidation reactions. The catalytic properties of many oxides are enhanced when they are supported on another oxide. For example, V_2O_5 supported on the anatase polymorph of TiO_2, V_2O_5/TiO_2(a), is more selective to pthalic anhydride during the

oxidation of o-xylene than V_2O_5 alone [20]. Furthermore, the selectivity and activity of V_2O_5/TiO_2(a) catalysts are superior to those of vanadia supported on γ-alumina, V_2O_5/Al_2O_3(γ) [21]. This synergistic effect is a clear demonstration of structure sensitivity and has been exploited commercially in numerous oxide systems [22] .

"Highly-Crystalline" Oxides. Catalysts with a high surface area are desirable because they offer increased efficiency by maximizing the number of possible reaction sites while minimizing the total volume of the catalyst. While this generally enhances the activity of the oxide, some catalysts show superior selectivity when they are prepared in a highly crystalline form with a relatively low surface area. For example, it has been shown that highly crystalline Bi-Mo-O catalysts, prepared by calcining at high temperatures, are more selective for the partial oxidation of alcohols then their poorly-crystalline counterparts, synthesized at low temperatures, which tend to oxidize deeply [23].

2.3.2 Theories of Structure Sensitivity

Explanations of structure sensitivity are usually developed on a case-by-case basis by using the measured properties of the catalyst and some model of its anticipated surface structure. In most cases, the surface structure is taken to be the ideal, bulk terminated surface. Allowances are sometimes made for thermally generated defects associated with non-stoichiometry, such as oxygen vacancies [7] and crystallographic shear (CS) planes [5]. The properties of a catalyst can sometimes be rationalized in hindsight, but, the ability to accurately predict catalytic properties, based solely on surface structural models, has not been demonstrated. Furthermore, the structural arguments used to explain one catalyst's properties during a particular reaction can rarely be extended to other reactions or catalysts.

Adsorption and Catalytic Activity. Before the catalyst can promote an oxidation reaction, the hydrocarbon must adsorb on the catalyst's surface. Therefore, any surface feature that promotes or inhibits adsorption plays an important role in the redox process. The primary adsorption sites on oxide surfaces are believed to be *coordinatively unsaturated* surface sites [1,5,7]. These are metal atoms at the surface of the oxide which have a lower oxygen coordination than is realized in the bulk [1,5,7,22,24,25]. There are a number of ways in which these undercoordinated sites can be introduced at the surface of an oxide. The simplest example is the formation of an oxygen vacancy; any surface or sub-surface metal atoms which coordinate the V_O will have a reduced coordination number.

The bulk structure of the oxide may dictate that unsaturated metal atoms are exposed at certain crystallographic planes when they terminate the surface. The ReO_3 structure, shown in Fig. 2.2, is composed of a three dimensional corner sharing network of ReO_6 octahedra in axial alignment. The creation of a $ReO_3(100)$ surface requires breaking one of the Re-O bonds in each Re-O-Re unit where the octahedra share apical O along <100>. The O can only go with one of the Re in each unit and, as a result, the other Re will be left with a reduced coordination number (CN) of five. Similarly, the introduction of a step, island, or pit on the surface can lead to the exposure of undercoordinated metal ions. The number of sites exposed will depend on the crystallographic orientation of the surfaces which bound these features. The role of coordinatively unsaturated surface sites in the adsorption of reactant species has been demonstrated many times and it is generally believed that these sites are the key to the activity of catalysts [1,7]. A simple example can be found in comparisons of the adsorptive properties of the Zn terminated (0001) and O terminated $(000\bar{1})$ surfaces of ZnO [7].

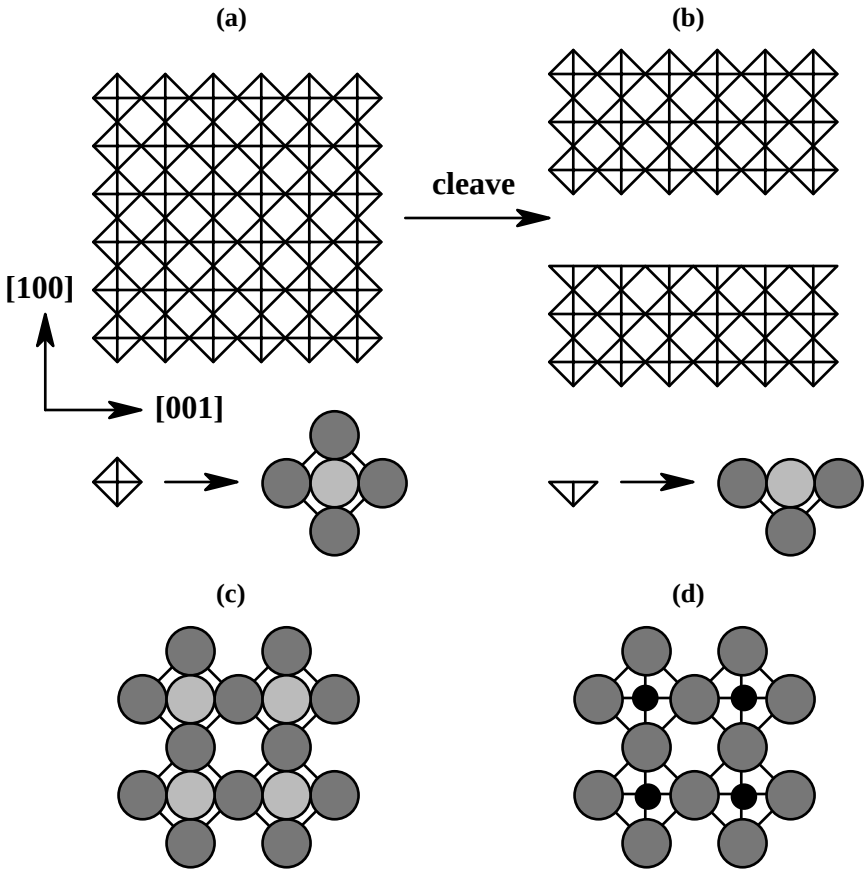

Figure 2.2 (a) Formation of coordinatively unsaturated surface sites during the creation of a ReO_3(100) surface. (b) The O in each Re-O-Re unit across the (100) interface can only go with one Re atom upon cleavage. The other Re is left in reduced (5-fold) coordination with respect to the bulk (6-fold) coordination. It has been assumed that all O go to the same half of the crystal, however, other configurations are possible. (c) ReO_3(100) surface terminated by complete (6-fold) octahedra and (d) incomplete (5-fold) octahedra. The small, black spheres are Re atoms. The large spheres are O and the lighter O are positioned above the darker ones.

Redox and Acid-Base Sites. The distinction is often made between acid-base and redox sites on oxide surfaces [1,5,7,9,13]. At redox sites the catalyst is able to easily exchange lattice oxygen with reactants or the atmosphere. On the other hand, proton transfer or exchange is favorable at acid-base type sites. If such ideally distinct sites exist, very different products should be formed at the two during reactions with any given hydrocarbon. The presence of both types of sites could be important, for example, during a multistep reaction which requires both proton exchange and oxygen insertion. For layered oxides, such as V_2O_5 and MoO_3, redox sites are thought to be localized on the basal planes while acid-base sites are thought to be located on the edge facets [5,7,9]. While it is often difficult to predict the acidity of surface sites, this type of site specificity is commonly invoked to explain catalytic anisotropies.

2.4 The Molybdenum Oxides

2.4.1 The Structural Chemistry of the Molybdenum Oxides

Molybdenum trioxide is the thermodynamically stable oxide of Mo under ambient conditions. Like most other transition metal oxides, when the partial pressure of oxygen is lowered, the average oxidation state of the Mo atoms decreases and the oxide is reduced. In MoO_3, reduction is accommodated by the formation of two oxygen stoichiometry compensating defects: oxygen vacancies and crystallographic shear (CS) planes [26,27]. Below oxygen to metal ratios of 2.90, seven stable and/or metastable sub-oxides have been identified between the compositions of MoO_3 and MoO_2: $Mo_{18}O_{52}$, Mo_9O_{26}, Mo_8O_{23}, Mo_5O_{14}, $Mo_{17}O_{47}$, η-Mo_4O_{11} and γ-Mo_4O_{11} [28]. The structural chemistry of these phases was described several decades ago in a series of papers by Kihlborg [28-33]. The space groups and lattice parameters of the oxides studied are presented in Table 3.2.

α-MoO_3. The layered structure of α-MoO_3 is illustrated in Fig. 2.3 [29]. Each layer is composed of two corner-sharing nets of MoO_6 octahedra that link by sharing edges along <001>. The adjacent double-octahedral layers are then linked along <010> only by weak van der Waals forces. In projection along [010] one sees a corner-sharing net that is characteristic of the ReO_3 structure. The α-MoO_3 structure was refined by Kihlborg and may be described by the Pbnm space group with the following established lattice parameters:

a = 3.9628 Å b = 13.855 Å c = 3.6964 Å

The MoO_6 octahedra which make up the MoO_3 structure are distorted and the Mo-O bond distances in each octahedron vary between 1.67 and 2.33 Å [34]. The shortest, strongest bonds which connect the Mo to the apical O that terminate the octahedra on (010) can viewed as double bonds (Mo=O). Within the {010} layers, there are two distinct sets of bridging (Mo-O-Mo) oxygen sites which link the polyhedra along <001> and <100>. Along <100>, the O sites bridge two octahedra within the same octahedral net and, therefore, these O are coordinated by only 2 Mo atoms. One of these Mo-O bonds is short and strong, 1.734 Å, while the other is longer and weaker, 2.251 Å. The second set of bridging oxygen atoms join two octahedra in the same layer along <001> and also join these to an octahedron in the layer below. Therefore, each of these O is coordinated by three Mo atoms. Of these three Mo-O bonds, two have identical bond lengths of 1.948 Å, while the third is longer, 2.332 Å. Due to the anisotropy in the Mo-O bond distances, the MoO_3 structure can also be viewed as consisting of infinite

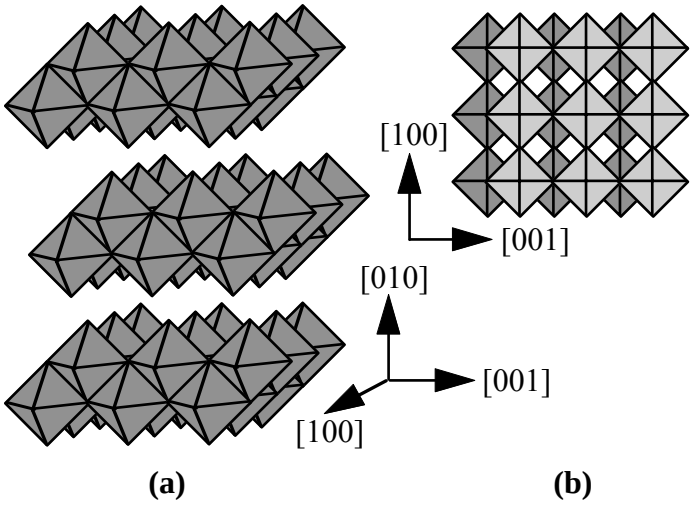

Figure 2.3. Idealized polyhedral representation of the α-MoO_3 structure. (a) The structure is composed of double octahedral layers stacked along [010]. The spacing between adjacent double layers is 6.9 Å. (b) A projection on the (010) plane shows two superimposed rectangular nets of corner-sharing octahedra. The shaded net is below the unshaded one.

chains of MoO_4 tetrahedra, parallel to <001>, joined by weaker Mo--O (d = 2.332 Å) bonds along <100> [29].

The anisotropic crystal structure of MoO_3 manifests itself in the distinct habit and mechanical instability of single crystals. Because the structure is composed of layers which are connected by only weak van der Waals bonds, crystals are micaceous and platy and cleave easily along the van der Waals gap. Creation of an (010) surface requires breaking no primary Mo-O bonds and this surface typically dominates the surface area of single crystals and powdered samples. After (010), creation of a (100) surface requires breaking the smallest number of bonds and, also, one of the weakest bonds in the structure. Not surprisingly, crystals are also commonly observed in needle-like morphologies with extended {010} and {100} facets.

$Mo_{18}O_{52}$ and Mo_8O_{23} - The Crystallographic Shear (CS) Phases. The $Mo_{18}O_{52}$ ($MoO_{2.889}$) [30] and Mo_8O_{23} ($MoO_{2.875}$) [31] structures can be derived from the fully oxidized structures of MoO_3 or ReO_3 by crystallographic shear (CS) operations, as illustrated in Fig. 2.4. In the context of the higher molybdenum oxides, one can think of CS as transforming a subset of octahedra, along specific planes, from a corner-sharing to an edge-sharing arrangement. Thus, the transformation reduces the average O coordination number. The shear operation in each crystal is characterized by a translation vector (the magnitude and direction of the shear) and a plane of propagation. For example, the $Mo_{18}O_{52}$ structure derives directly from α-MoO_3 by introducing shear

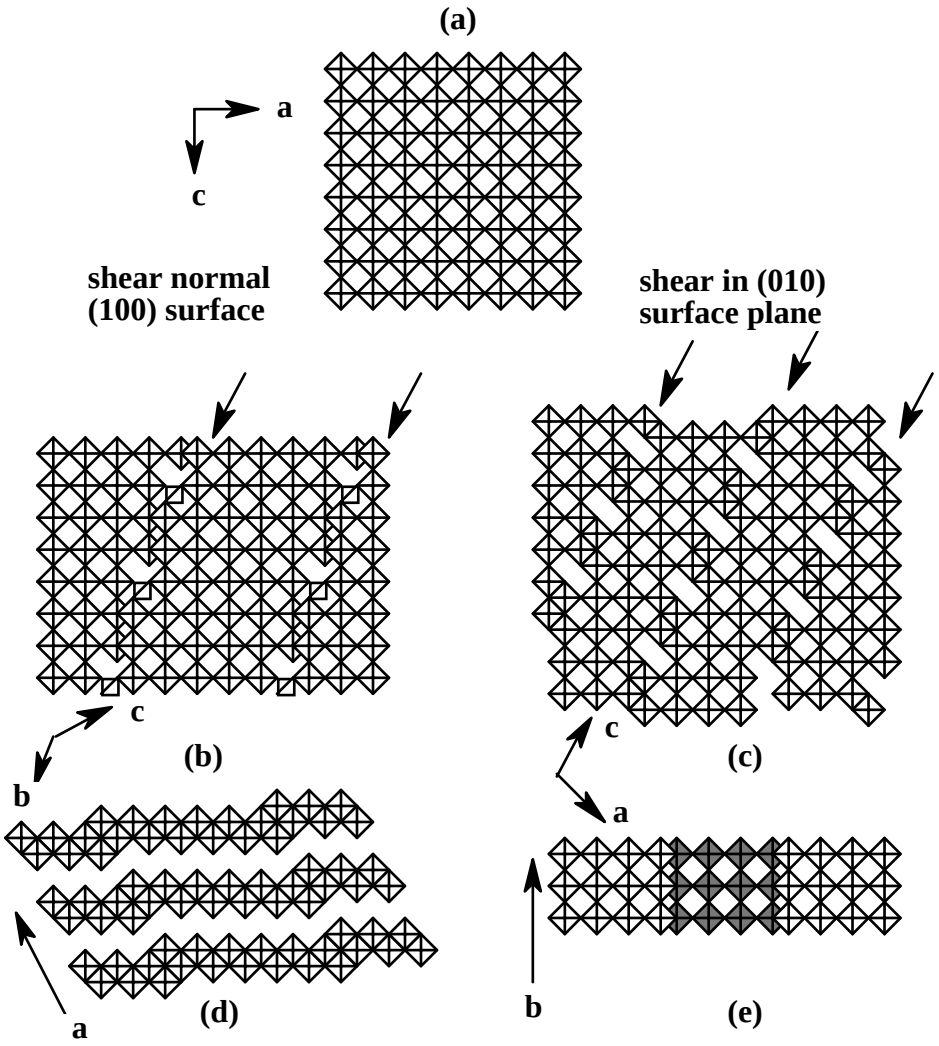

Figure 2.4 The relationship between a layer of the MoO_3 structure, viewed along [010] (a), a layer of the $Mo_{18}O_{52}$ structure, viewed along [100] (b), and a layer of the Mo_8O_{23} structure, viewed along [010] (c). CS operations (see text for details) are used to derive the reduced structures. Arrows have been used to guide the eye to the CS planes. Views parallel to $Mo_{18}O_{52}(100)$ (d) and $Mo_8O_{23}(010)$ (e).

of $\frac{1}{2}\langle 1\bar{1}0\rangle\{35\bar{1}\}$. The new cell is indexed such that $[010]_{MoO_3} \| [100]_{Mo_{18}O_{52}}$. The Mo_8O_{23} structure is derived from the ReO_3 structure by a CS operation of $\frac{1}{2}\langle 101\rangle\{\bar{1}02\}$ and the new cell is indexed such that $[010]_{MoO_3} \| [010]_{Mo_8O_{23}}$.

There are noteworthy differences between these two shear structures. While the $Mo_{18}O_{52}$ structure is derived from the α-MoO_3 structure, the Mo_8O_{23} structure is derived from the ReO_3 structure. This is an important distinction because the layers that make up Mo_8O_{23} (see Fig. 2.4c) are joined along <010> by corner-shared connections at the apical O position. Thus, Mo_8O_{23} is a three dimensionally bonded structure that does not contain a van der Waals gap as the $Mo_{18}O_{52}$ and α-MoO_3 structures do. Another difference, important for the interpretation of SPM observation described in Chapter 4, is

the direction of the shear vector with respect to the cleavage plane. The shear in $Mo_{18}O_{52}$ has a component normal to the (100) surface plane that produces a shear step (its height equal to the radius of an O ion) along the line of intersection. The direction of the shear in Mo_8O_{23}, on the other hand, lies in the (010) surface plane and, therefore, does not produce a shear step on this surface. In the $Mo_{18}O_{52}$ structure, the lines formed where the shear planes intersect the surface are oriented along <010> and are spaced at 21 Å intervals along <001>. In Mo_8O_{23}, these lines of intersection are oriented along <001> and are spaced at 13 Å intervals along the <100> direction. Although both types of CS planes would be classified as defects if distributed inhomogeneously in reduced MoO_{3-x}, they are periodic structural components of the shear phases and can, therefore, be unambiguously identified.

It has been suggested that similar shear structures, with slightly different metal/oxygen ratios, should also exist and two homologous series of shear structures related to $Mo_{18}O_{52}$ and Mo_8O_{23} have been proposed, Mo_nO_{3n-m+1} and Mo_nO_{3n-1} [28]. In these series, different metal to oxygen ratios are accommodated by varying the spacing of the CS planes and the amount of octahedral edge sharing within the parent MoO_3 and ReO_3 structures. For the case of the ReO_3 derivatives, Mo_8O_{23} and Mo_9O_{26} are easily prepared in gram quantities. However, higher members have only been sparsely detected during TEM studies. $Mo_{18}O_{52}$ is the only MoO_3 derivative which can be synthesized, phase pure, in large quantities. Again, however, higher members have been detected during EM and single crystal studies [27,28].

η-Mo₄O₁₁ and γ-Mo₄O₁₁. The Mo_4O_{11} structures provide an example of another mechanism by which the metal to oxygen ratio may be increased in molybdenum suboxides. Rather than having infinite slabs of the ReO_3 structure linked together at CS planes, the slabs are linked together by planes of MoO_4 tetrahedra [28,32]. In the η-Mo_4O_{11} structure, these planes are spaced at 12 Å intervals and inspection of Fig. 2.5a allows one to see that although it is a three dimensionally bonded structure, the lowest density of bonds is in the tetrahedral layers parallel to (100). We assume, therefore, that when crystals are cleaved to expose {100} surfaces, they will be terminated by tetrahedral MoO_4 groups. A view parallel to the (100) plane (see Fig. 2.5b) shows that the tetrahedral MoO_4 groups are elevated farthest from the surface plane and the view projected on (100), shown in Fig. 2.5c, shows that these groups form a rectangular net.

The structure of the high-temperature γ modification of Mo_4O_{11} is very similar, and can also be described as being composed of distorted slabs of the ReO_3 structure (extending infinitely in two dimensions) linked by MoO_4 tetrahedra. In both structures,

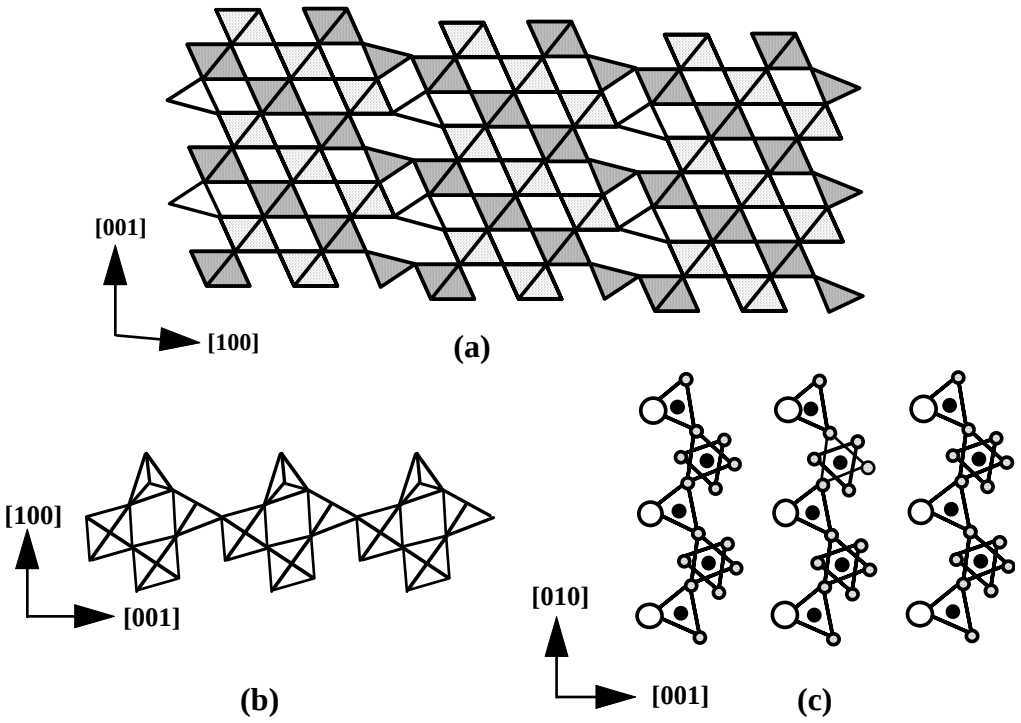

Figure 2.5 The η-Mo_4O_{11} structure. (a) An [010] projection showing the planes of tetrahedral groups that separate ReO_3-like blocks of the structure. The polyhedra with different shades are at different vertical levels. (b) A view parallel to the (100) surface that is expected to form during cleavage. (c) A plan-view of the (100) surface. Circles represent O at the vertices of surface polyhedra. The O atoms represented by the largest circles, at the vertices of the tetrahedra, are elevated further from the surface than the others. Mo atom positions are represented by the small black circles.

the slabs have the same thickness. They differ, however, in the orientation of the rows of octahedra in the adjacent slabs. In η-Mo_4O_{11} these rows of octahedra are always parallel, as can be seen in Fig. 2.5. In the γ modification, however, the polyhedra in every other row are parallel while those in the adjoining slabs are nearly anti-parallel. The relationship between these two structures is illustrated in Fig. 2.6.

Mo_5O_{14} and $Mo_{17}O_{47}$. The structures of Mo_5O_{14} and $Mo_{17}O_{47}$ are interesting because they feature Mo atoms in pentagonal bipyramidal coordination with oxygen, in addition to octahedral coordination [28,35]. The polyhedra link by corner and edge sharing in two dimensions to form intricate, planar networks. In the third dimension, the planar nets are stacked directly on top of one another (A A... stacking), such that equivalent polyhedra in adjacent layers share apical O atoms, to form elaborate tunnel structures that extend infinitely in one dimension. Although Kihlborg was able to identify the phases and solve their structures with single crystal X-ray diffraction, the stability of these phases is questionable because they can not be prepared as single phase products in quantity.

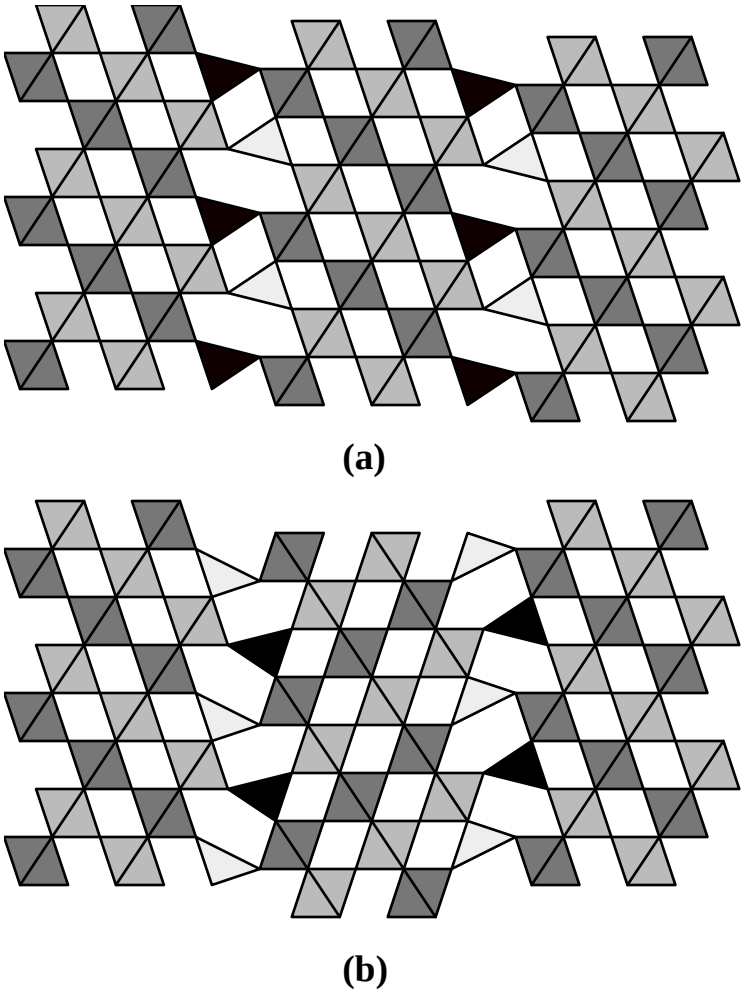

Figure 2.6 The crystal structures of the Mo_4O_{11} polymorphs. (a) η-Mo_4O_{11} (monoclinic) and (b) γ-Mo_4O_{11} (orthorhombic). In both structures, slabs of the ReO_3 structure are connected by MoO_4 tetrahedra, however, the orientation of the slabs differ in the two structures. See Text for a complete description.

2.4.2 Electronic Properties of the Molybdenum Oxides

The electronic structure and properties of the higher molybdenum oxides have not been systematically investigated. However, there is the general trend that with increasing metal to oxygen ratios, the electronic conductivity increases. Stoichiometric MoO_3 is an insulator with a band gap of 3.1 eV. When the oxide is reduced, by the introduction of impurity donor atoms or by oxygen deficiency, electronic donor levels are created near the bottom of the conduction band and, therefore, the reduced oxides behave as semiconductors [28,36]. The variation in conductivity of the Mo oxides ranges from the insulating MoO_3 to the semiconducting $Mo_{18}O_{52}$ (ρ = 78.1 Ω-cm) to the metallic η-Mo_4O_{11} (ρ = 1.66 x 10^{-4} Ω-cm). The experimentally determined, single crystal resistivities of these phases are presented in Table 3.2. The anisotropy in these structures leads to speculation that the electronic properties will also be anisotropic, however, definitive data on these variations are not available.

2.4.3 Previous Studies of Molybdate Surfaces

The interesting surface properties of MoO_3 have motivated earlier studies with conventional surface analysis methods [37-42]. Specifically, the results of low energy electron diffraction (LEED) [37,38], electron energy loss spectroscopy, X-ray photoelectron spectroscopy (XPS), ultra-violet photoelectron spectroscopy (UPS) [37], angle resolved UPS [39], and reflection high energy electron diffraction (RHEED) [38] experiments have been reported for MoO_3. RHEED data has also been reported for $Mo_{18}O_{52}$ [41]. The electron diffraction results indicate that the ideal $MoO_3(010)$ surface has a 1x1 structure. However, the stoichiometric surface is difficult to prepare and not entirely stable during analysis. Separate research groups have noted that in vacuum, the surface is easily damaged by even low energy electron probes [37,38]. For this reason, most of the reported results are actually characteristic of non-stoichiometric surfaces.

A number of SPM observations of molybdate surfaces have also been reported. Atomic scale resolution AFM images of a single layer of $MoO_3(010)$, formed by oxidation of the $MoS_2(0001)$ surface, had the expected (1x1) rectangular surface repeat unit [43]. There have also been ambient STM studies of some ternary molybdenum bronzes, $A_{0.3}MoO_3$ [44-47] and $A_{0.9}Mo_6O_{17}$ [46], where A is an alkali metal. While the focus of these studies has been on nanolithography [45,46] and charge density wave phenomena [47], atomic scale resolution images were also reported. In all of these reports, images were formed using conduction band states near the Fermi level and the authors noted a one-to-one correspondence between the configuration of bright spots in the images and the expected positions of polyhedra on the cleaved surfaces.

2.5 Molybdenum Trioxide (MoO_3) as a Catalyst

The most widely used partial oxidation catalysts are molybdates and vanadates [1]. Although pure MoO_3 is of limited commercial importance, it is the primary component in a number of important industrial catalysts. Examples include catalysts for methanol oxidation, $Fe_2(MoO_4)_3$ [1] and the oxidation and ammoxidation of propene and derivatives, Bi-Mo-O [1] and V-Mo-O [48]. Because MoO_3 is structurally "simple", relative to the multicomponent molybdates used industrially, and it has some inherent catalytic efficacy, it is frequently studied as a model partial oxidation catalyst [9-14]. The partial oxidation of methanol (MeOH) has been the focus of a number of previous investigations [9,25,79-90]. MoO_3 is the most selective (up to 100%) known catalyst for the partial oxidation of MeOH to formaldehyde [1]. On the other hand, it also has a very low activity for the reaction and, therefore, is not commercially viable. While it has been proposed that the reaction is surface structure sensitive, the mechanistic role that

structure plays in the reaction is debatable and, therefore, definitive structure-reactivity relationships have not been established [9].

In the following sections, previous work relevant to the partial oxidation of MeOH on MoO_3 is reviewed. In addition to a discussion of the reaction mechanism and the proposed role that surface structure might play, this section will also review previous work concerning the bulk structural evolution of MoO_3 during catalytic and redox processes. Because the partial oxidation of MeOH to formaldehyde on MoO_3 is thought to conform to a redox mechanism of the Mars - van Krevelen type, the structural evolution of MoO_3 during reduction is addressed first [1,2].

2.5.1 The Structural Evolution of MoO_3 during Reduction.

The reduction of MoO_3 in hydrogen and in vacuum has been investigated with conventional bulk and surface structure probes, including XRD [50-55], TEM [26,27,56-59], and LEED [37,38]. When reduced at temperatures greater than 350 ˚C, MoO_3 becomes oxygen deficient and nonstoichiometry is accommodated through the formation of two structural defects: oxygen vacancies (V_O) and crystallographic shear (CS) planes [26,58,59]. With slight deviations from stoichiometry, O/Mo > 2.998, oxygen deficiency is accommodated solely by the formation of oxygen vacancies. Between the compositions of $MoO_{2.998}$ and $MoO_{2.990}$, oxygen stoichiometry is compensated through a combination of CS planes and oxygen vacancies. Electron microscopy studies of samples that have been beam heated in vacuum [26,27,57], reduced in H_2 *ex situ*, and reduced with 100 mT H_2 *in situ* [58,59] support these defect models. The CS planes in the structure are randomly spaced but always have the same crystallographic orientation. The CS process introduces a shear displacement and the direction and plane of the shear may be described by $<\mathbf{a}/2\ \mathbf{b}/7\ 0>\{1\ \bar{2}\ 0\}$ [26]. As the degree of reduction is increased the CS plane density increases. At lower oxygen stoichiometries (O/Mo < 2.990), XRD [50-55] and TEM results indicate that a second phase, γ-Mo_4O_{11}, nucleates and then coexists with oxygen deficient MoO_{3-x}. Beyond this, γ-Mo_4O_{11} and MoO_2 are believed to coexist.

Structural changes have also been reported during TEM studies of the reduction of MoO_3 at temperatures less than 350 ˚C. When samples have been beam heated in the microscope's vacuum [26,57,60-64] or reduced *in situ* in an environmental cell [56,58], a distinct, cross-hatched pattern of "domains" has been observed to nucleate at approximately 120 ˚C and persist up to 350 ˚C. The domains were first reported more than 50 years ago and have been described in different ways by different authors. The observations may, however, be summarized and generalized as follows. The domains

form at low temperatures and grow in size (coarsen) as the temperature is increased. The domains are always acicular (needle-like) in habit and oriented with their long axis parallel to a direction very near the <101> axis of MoO_3. When the temperature exceeds approximately 350˚C, the domain contrast disappears and CS planes nucleate within the regions that were previously bounded by the domains. When samples are heated rapidly to temperatures greater than 350˚C, the domains are not observed prior to CS plane nucleation.

The indices used to describe the orientation of the domains vary from author to author. For example, while some [26,57,64] have described the domains as being oriented along the <203> axis of the crystal (which makes a 35.54˚ angle with <001>, in the most recent work, Gai and coworkers [56,58,59] have indexed the direction as <304> which makes a 38.8˚ angle with <001>. Regardless of this choice, a comparison of the micrographs in the references cited above makes it clear that all the groups observed the same biphasic microstructure. Selected area diffraction patterns indicate that the structure of the domains is similar to that of the MoO_3 matrix and this similarity has been interpreted in two different ways [26,57-59,64].

Because CS planes nucleated within the domains (when they were present), Bursill [26] first postulated that the domains were an oxygen deficient phase, $MoO_{2.9975}$, which was isostructural with MoO_3. This composition was deduced based on the size and the number of CS planes that nucleated within the domains when the domain contrast disappeared. Later, however, convergent beam electron diffraction studies led Bursill and coworkers [57] to the conclusion that the domains were actually a molybdenum oxide-hydroxide (later termed a 'hydrogen molybdenum bronze' [65]) of the general formula $MoO_{3-x}(OH)_x$ (alternatively, H_xMoO_3) similar to those prepared via acidic reduction by Glemser and Lutz [66]. This interpretation was supported by similarities in the symmetry and the a and c lattice parameters of the domains and the hydrogen bronze, $Mo_4O_{10}(OH)_2$. Bursill also advanced a probable formation mechanism; during sample preparation, H atoms adsorb on the surfaces of the oxide and, when the sample is beam heated, these species diffuse into the lattice of the thin particles and react at approximately 200 ˚C to form domains of H_xMoO_3 [57].

In later studies, Gai and coworkers [57,58,59] observed the same two phase microstructure as previous groups. In this case, however, the microstructure was observed during *in situ* reduction studies within a TEM environmental cell. Because the domains were observed in environments from which hydrogen was deliberately excluded, such as high purity CO, the authors concluded that the domains could not be a protonated phase. Instead, they proposed that they were an oxygen deficient form of MoO_3

(identical to that initially proposed by Bursill [26]) which had an ordered array of oxygen vacancies [58]. This oxygen deficient superlattice phase has never been detected in any XRD study of the Mo-O system [50-55]. Data from the current experiments provide a consistent resolution for the competing models advanced by Bursill [57] and Gai [58,59]. To complete the relevant background, the conditions under which H_xMoO_3 is known to form are outlined below.

2.5.2 The Formation of H_xMoO_3 when MoO_3 Reacts with Atomic H.

At temperatures below 250 ˚C in the absence of O_2, MoO_3 intercalates available atomic H and this leads to the formation of hydrogen molybdenum bronzes, H_xMoO_3 [65-73]. Similar behavior by WO_3 [67] and V_2O_5 [68] is also well documented. During intercalation, the H atoms enter the MoO_3 lattice topotactically and occupy interstitial sites between the layers of the structure [65]. A common method of supplying atomic H involves mixing the oxide with a hydrogen dissociation catalyst (Pt or Pd) and then exposing the mixture to H_2(g) [69,70]. During this process, known as hydrogen "spill over" [69], H_2 dissociates on the Pt particles and then H spills over to react with the oxide. Large quantities of H can intercalate and, ultimately, a hydrogen bronze with the composition $H_{1.6}MoO_3$ is formed [69-71]. MoO_3 will protonate in the presence of even small quantities of atomic H, for example, pH < 1x10^{-8} Torr in a UHV chamber with $P_T \approx pH_2$ = 1 x 10^{-7} Torr [71,72]. In this case, H_2 was dissociated with a red-hot tungsten filament placed in the vicinity of the MoO_3 sample. An interesting feature of the intercalation reaction is that it is self-catalyzing. Once a small fraction of the bronze has formed, it is capable of catalyzing the dissociation of H_2 alone and the presence of Pt or a tungsten filament is no longer necessary [72].

During intercalation, the H atom donates its electron to the oxide and, therefore, the oxide becomes electronically conductive. The oxide is also modified structurally during the process; the topotactic transformation to $H_{1.6}MoO_3$ results in a distortion of the lattice from orthorhombic to monoclinic symmetry and a decrease in the oxide's interlayer spacing. Hydrogen bronzes can also be prepared by acidic reduction in aqueous media [65,66]. Four distinct bronzes, H_xMoO_3 (where $0.23 \leq x \leq 0.4$, $0.85 \leq x \leq 1.04$, $1.55 \leq x \leq 1.72$, $x = 2.0$), have been prepared in this way and they have been characterized with XRD [65,66,68], and, in some cases, neutron diffraction [73] and infrared (IR) spectroscopy [74-77]. There is no rule of thumb concerning the structural distortions that accompany intercalation. For example, the least protonated bronze ($0.23 < x < 0.4$) maintains an orthorhombic lattice and the interlayer spacing is greater than the parent MoO_3, in contrast to $H_{1.6}MoO_3$. Finally, optical changes also accompany

transformation to H_xMoO_3 and the different phases adopt a brilliant range of colors from deep blue ($0.23 \leq x \leq 0.40$) to red ($1.55 \leq x \leq 1.72$) [65,66].

At high temperatures, the hydrogen molybdenum bronzes decompose as H leaves the structures in the form of H_2O [74,75]. $H_{1.68}MoO_3$ decomposes to suboxides of Mo above 300 ˚C in the presence of H_2. In the presence of O_2, it reverts to MoO_3 above ~200 ˚C. [67,78]. The decomposition of the blue orthorhombic bronze ($0.23 \leq x \leq 0.40$), during heating in air and *in vacuo* has been studied in some detail [74,75,77]. In vacuum, the bronze is stable up to about 287 ˚C. At this temperature, the structure releases some H and O (as H_2O) and an oxygen deficient bronze, $H_{0.21}MoO_{2.95}$, which is isostructural with the starting structure forms. This phase is then stable up to 390 ˚C where it transforms to $H_{0.06}MoO_{2.88}$, which is isostructural with α-MoO_3. This phase then decomposes to $MoO_{2.86}$ (446 ˚C) and, finally, a mixture of MoO_3 and Mo_4O_{11} (610˚C). $MoO_{2.86}$ has an orthorhombic structure similar to MoO_3, but, little else is known about the phase.

2.5.3 Reactions between Methanol (MeOH) and MoO_3

Bulk Structural Evolution during Reactions with MeOH. The structural evolution of MoO_3 during reactions with MeOH-He mixtures was studied by Gai and Labun [79] with TEM. The structural modifications they observed were identical to those seen during *in situ* studies of reduction in vacuum or H_2 [26,56-64] (described in 2.5.1). When samples were reacted with MeOH *in situ* or in a separate reactor outside the microscope, <304> oriented domains identical to those observed during previous reduction studies were observed at approximately 250 ˚C. Up to temperatures of 350 ˚C, the domains persisted and coarsened. At temperatures greater than 380 ˚C, the domain contrast disappeared and CS planes nucleated in the regions previously bounded by the domains. In the discussion of these results, Gai and Labun [79] maintain that the domains observed at low temperatures must be oxygen deficient (MoO_{3-x}) and, again, cite the formation of domains in CO as an unambiguous demonstration that they are not the hydrogen bronze, H_xMoO_3, postulated by Bursill and coworkers [57].

The structural evolution of MoO_3 during reactions with MeOH-He mixtures has also been studied with X-ray diffraction. After reactions of 6 hr at 215˚C, Vergnon and Tatibouët [80] reported the formation of a hydrogen bronze with the composition $H_{0.31}MoO_3$. Guidot and Germain [81] performed a similar study and continuously recorded the XRD patterns of MoO_3 samples at 200 ˚C as they were exposed to different MeOH-He-O_2 mixtures. When O_2 was supplied in the feed, no change was observed in

the XRD patterns after reactions in excess of 31 h at 200 ˚C. If oxygen was eliminated a hydrogen bronze identical to the one reported by Vergnon and Tatibouët [80] formed.

Structure Sensitivity of MeOH Oxidation. The influence of MoO_3's surface structure on its reactivity during the oxidation of MeOH is the subject of debate. While it is generally recognized that the active sites for methanol chemisorption and oxidation are undercoordinated surface Mo sites, there is disagreement concerning the crystallography and chemical nature of these sites. It was first proposed by Tatibouët and Germain [9] that the {010} (basal) facets of MoO_3 were responsible for formaldehyde formation while the {h0l} (lateral) facets were responsible for the formation of higher order products such as dimethyl ether and dimethoxy methane. However, the results of subsequent temperature programmed desorption (TPD) spectroscopy studies led Farneth and coworkers [82,83] to conclude that the {010} facets play a subordinate role in the reaction and that the lateral facets were responsible for the formation of all products. The anisotropic crystal structure of MoO_3 provides support for this conclusion. If free surfaces are created by breaking the smallest number of bonds, the Mo atoms on (010) surface remain fully coordinated while those on lateral facets will have reduced coordination and unsaturated bonds. Chung and coworkers [84] have also cited the importance of undercoordinated surface Mo and deduced that formaldehyde is formed at terminal oxygen (Mo=O) vacancy sites while higher order products are formed at bridging oxygen (Mo-O-Mo) vacancy sites.

Proposed Mechanism of MeOH Oxidation. MeOH chemisorbs dissociatively on MoO_3 at temperatures as low 25 ˚C. Adsorption is thought to occur at a coordinatively unsaturated surface Mo and results in the formation of a surface methoxy and a surface hydroxyl [82-86]. The existence of the surface methoxy has been demonstrated with IR spectroscopy [87-89]. The subsequent fates of the methoxy and hydroxyl are dependent on the experimental conditions. During temperature programmed desorption (TPD) spectroscopy experiments, the methoxy decompose to formaldehyde and the protons liberated from the alcohol react with lattice oxygen to form H_2O [82,83]. Available data indicate that the same process occurs over a wide range of temperatures and gas compositions in flow reactors [84-87,90] and methoxy decomposition is believed to be the rate limiting step of the reaction [85,86]. The incorporation of lattice oxygen into the product water vapor has been demonstrated with O^{18} isotopic labeling [85,86] and, therefore, the reaction conforms to a redox mechanism of the Mars - van Krevelen type [2,82]. The mechanism shown schematically in Fig. 2.7 has been proposed for MeOH

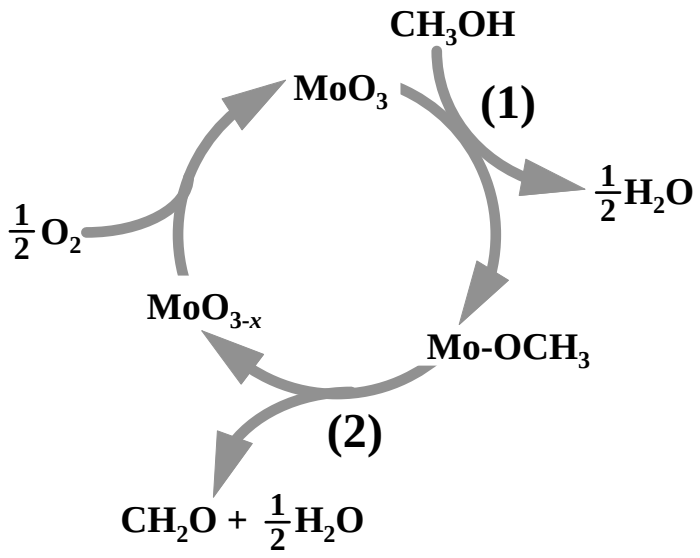

Figure 2.7 Proposed mechanism for the partial oxidation of methanol to formaldehyde on MoO_3 [82,83]. The first step "(1)" is the dissociative chemisorption of MeOH. This leads to the formation of a surface methoxide, OCH_3, and the liberation of a proton. In the second step, "(2)", the methoxy decomposes to formaldehyde via the liberation of a second proton. The protons then react with lattice O to form H_2O.

oxidation to formaldehyde on MoO_3. If the reaction is conducted in the absence of gas phase O_2, products include methane, higher order products (such as dimethyl ether), and H_2, but, not formaldehyde [80,81,86]. Therefore, MeOH chemisorption still occurs in the absence of O_2, but, the surface methoxy do not decompose to formaldehyde.

2.6 References

[1.] A.W. Sleight *in* " Solid State Chemistry Compounds", (A.K. Cheetham and P. Day, eds.), p. 171, Clarendon Press, Oxford, U.K. (1992).

[2.] R. Mars and D.W. van Krevelen, *Chem. Eng. Sci.* **3** (1954) 41.

[3.] L. YA. Margolis, *Catal. Rev.* **8** (1973) 241.

[4.] A. Bielanski and J. Haber, *Catal. Rev.-Sci. Eng.* **19** (1979) 1.

[5.] J. Haber *in* "Solid State Chemistry in Catalysis", (R.K. Grasselli and J.F. Brazdil, Eds.), p. 1, American Chemical Society, Washington D.C. (1985).

[6.] M.V. Twigg, Catalyst Handbook, 2nd. Ed., Wolfe Publishing (1989).

[7.] M. A. Barteau, *J. Vac. Sci. Tech. A* **11** (1993) 2162.

[8.] P. Kofstad, Non-stoichiometry, Diffusion, and Electrical Conductivity in Binary Metal Oxides, Robert E. Krieger Publishing Company, Malabar, FL, (1983).

[9.] J.M. Tatibouet and J.E. Germain, *J. of Catal.* **72** (1981) 375.

[10.] J.C. Volta and J.M. Tatibouet, *J. of Catal.* **93** (1985) 467.
[11.] J.M. Tatibouet, Ch. Phichitkul and J.E. Germain, *J. of Catal.* **99** (1986) 231.
[12.] K. Bruckman, J. Grabowski, J. Haber, A. Mazurkiewicz, J. Sloczynski and T. Wiltowski, *J. of Catal.* **104** (1987) 71.
[13.] M. Abon, J. Massardier, B. Mingot, J.C. Volta, N. Floquet and O. Bertrand, *J. of Catal.* **134** (1992) 542.
[14.] M.R. Smith and U.S. Ozkan, *J. of Catal.* **141** (1993) 124.
[15.] M. Gasior and T. Machej, *J. of Catal.* **83** (1983) 472.
[16.] K. Lui, S. Akhte and H.H. Kung *in* "Solid State Chemistry in Catalysis", (R.K. Grasselli and J.F. Brazdil, Eds.), p. 205, American Chemical Society, Washington D.C. (1985).
[17.] W.E. Farneth, E.M. McCarron, A.W. Sleight and R.H. Staley, , *Langmuir* **3** (1987) 217.
[18.] R.L. McCormick and G.L. Schrader, *J. of Catal.* **113** (1988) 529.
[19.] J.M. Tatibouet and J.E. Germain, *C. R. Acad. Sci. Paris Ser. C* **290** (1980) 321.
[20.] P. Courtine *in* "Solid State Chemistry in Catalysis", (R.K. Grasselli and J.F. Brazdil, Eds.), p.37. American Chemical Society, Washington D.C. (1985).
[21.] M. Inomata, A. Miyamato and J. Murakami, *J. Phys. Chem.* **85** (1981) 2372.
[22.] D.B. Dadyburjor, S.S. Jewur and E. Ruckenstein, *Catal. Rev.-Sci. Eng.* **19** (1979) 293.
[23.] H. Arora, G. Deo, I.E. Wachs and A.M. Hirt, *J. of Catal.* **159** (1996) 1.
[24.] J. Happel, M. Hnatow and L. Bajars, Base Metal Oxide Catalysts Marcell Dekker, NY (1977).
[25.] U. Chowdhry, A. Ferretti, L.E. Firment, C.J. Machiels, F. Ohuchi, A.W. Sleight, and R.H. Staley, *App. Surface Science* **19** (1984) 360.
[26.] L.A. Bursill, *Proc. R. Soc. London* **A311** (1969) 267.
[27.] L.A. Bursill, *Acta. Crystallogr. Sect. A* **28** (1972) 187.
[28.] L. Kihlborg, *Ark. Kemi* **21**, 471 (1963).
[29.] L. Kihlborg, *Ark. Kemi* **21**, 357 (1963).
[30.] L. Kihlborg, *Ark. Kemi* **21**, 443 (1963).
[31.] L. Kihlborg, *Ark. Kemi* **21**, 461 (1963).
[32.] L. Kihlborg, *Ark. Kemi* **21**, 365 (1963).
[33.] L. Kihlborg, *Acta Chem. Scand.* **13** (1959) 954.
[34.] A. Andersson and S. Hansen, *J. Catal.* **114** (1988) 332.
[35.] L. Kihlborg, *Ark. Kemi* **21** (1963) 427.

[36.] J.B. Goodenough *in* "Progress in Solid State Chemistry, Vol. 5", (H. Reiss, ed.), p. 145, Pergamon Press, NY (1971).

[37.] L. E. Firment and A. Ferretti, *Surf. Sci.* **129** (1983) 155.

[38.] L. C. Dufour, O. Bertrand, N. Floquet, *Surf. Sci.* **147** (1984) 396.

[39.] L.E. Firment, A. Ferretti, M.R. Cohen, and R.P. Merrill, *Langmuir* **1** (1985) 166.

[40.] O. Bertrand, N. Floquet, D. Jacquot, *Surf. Sci.* **164** (1985) 305.

[41.] N. Floquet and O. Bertrand, *Surf. Sci.* **198** (1988) 449.

[42.] N. Floquet and O. Bertrand, *Solid State Ionics* **32/33** (1989) 234.

[43.] Y. Kim and C.M. Lieber, *Science* **257** (1992) 375.

[44.] J. Heil, J. Wesner, B. Lommel, W. Assmus, and W. Grill, *J. Appl. Phys.* **65** (1989) 5220.

[45.] E. Garfunkel, G. Rudd, D. Novak, S. Wang, G. Ebert, M. Greenblatt, T. Gustafsson, and S.H. Garofalini, *Science* **246** (1989) 99.

[46.] G. Rudd, D. Novak, D. Saulys, R.A. Bartynski, S. Garofalini, K.V. Ramanujachary, M. Greenblatt, and E. Garfunkel, *J. Vac. Sci. Technol. B* **9** (1991) 909.

[47.] U. Walter, R. E. Thomson, B. Burk, M.F. Crommie, A. Zettl, and J. Clarke, *Phys. Rev B* **45** (1992) 11474.

[48.] T.V. Andruchkevich, *Catal. Rev.-Sci. Eng.* **35** (1993) 213.

[49.] G.W. Coulston, S.R. Bare, H. Kung, K. Birkeland, G.K. Bethke, R. Harlow, N. Herron, P.L. Lee, *Science* **275** (1997) 191.

[50.] L. L. Y. Chang and B. Phillips, *J. Am. Ceram. Soc.* **52** (1969) 527.

[51.] D.T. Hawkins and W. L. Worrell, *Met. Trans.* **1** (1970) 271.

[52.] M.J. Kennedy and S.C. Bevan, *J. Less-Common Met.* **36** (1974) 23.

[53.] O. Bertrand and L.C. DuFour, *Phys. Stat. Sol.* **60** (1980) 507.

[54.] A. Ueno, Y. Kotera, S. Okuda and C.O. Bennett, *in* "The Chemistry and Uses of Molybdenum" Proceedings of the 5nd Int. Conference, p250, Climax Mo. Co., Ann Arbor, MI (1982).

[55.] J. Sloczynski, *J. Solid State Chem.* **118** (1995) 84.

[56.] W. Thoni, P. Gai, and P.B. Hirsch, *in* "The Chemistry and Uses of Molybdenum" Proceedings of the 2nd Int. Conference, p129, Climax Mo. Co., Ann Arbor, MI (1976).

[57.] L.A. Bursill, W.C.T Dowell, P. Goodman and N. Tate, *Acta. Crystallogr. Sect. A* **34** (1978) 296.

[58.] P.L. Gai, *Phil. Mag. A* **43** (1981) 841.

[59.] P.L. Gai-Boyes, *Catal. Rev. Sci. Eng.* **34** (1992) 1.

[60.] R.D. Heidenreich and L. Sturkey, *J. Appl. Phys.* **16** (1945) 97.
[61.] O. Glemser and G. Lutz, *Kolloid-Z.* **119** (1950) 99.
[62.] H. König, *Z. Physik.* **130** (1951) 483.
[63.] H. Hashimoto, *J. Phys. Soc. Japan* **9** (1954) 150.
[64.] E. Pernoux and R. Borrelly, *J. Microscopie* **2** (1963) 407.
[65.] J.J. Birtill and P.G. Dickens, *Mat. Res. Bul.* **13** (1978) 311.
[66.] O. Glemser and G. Lutz, *Z. Anorg. Allg. Chem.* **264** (1951) 17.
[67.] D. Tinet, S. Partyka, J. Rouquerol and J.J. Fripiat, *Mat. Res. Bul.* **17** (1982) 561.
[68.] A.M. Chippindale and P.G. Dickens, *Solid State Ionics* **23** (1987) 183.
[69.] P.A. Sermon and G.C. Bond, *Catal. Rev.* **8** (1973) 211.
[70.] P.A. Sermon and G.C. Bond, *J. Chem. Soc. Faraday I* **72** (1976) 730.
[71.] R. Erre, H. van Damme, and J.J. Fripiat, *Surf. Sci.* **127** (1983) 48.
[72.] R. Erre, H. van Damme, and J.J. Fripiat, *Surf. Sci.* **127** (1983) 69.
[73.] P.G. Dickens, J.J. Birtill, and C.J. Wright, *J. Solid State Chem.* **28** (1979) 185.
[74.] N. Sotani, Y. Kawamoto, and M. Inui, *Mat. Res. Bull.* **18** (1983) 797.
[75.] N. Sotani, N. Yoshida, Y. Yoshioka, and S. Kishimoto, *Bull. Chem. Soc. Jpn.* **58** (1985) 1626.
[76.] P.G. Dickens, S.J. Hibble, and G.S. James, *Solid State Ionics* **20** (1986) 213.
[77.] T. Ohno, H. Miyata, F. Hatayama, and N. Sotani, *Bull. Chem. Soc. Jpn.* **60** (1987) 3435.
[78.] G.C. Bond and J.B.D. Tripathi, *J. of Less-Common Met.* **36** (1974) 31.
[79.] P.L. Gai and P.A. Labun, *J. Catal.* **94** (1985) 79.
[80.] P. Vergnon and J.M. Tatibouet, *Bull. Soc. Chem. Fr.* **11-12** (1980) I-455.
[81.] J. Guidot and J.E. Germain, *React. Kinet. Catal. Lett.* **15** (1980) 389.
[82.] W.E. Farneth, F. Ohuchi, R.H. Staley, U. Chowdhry, and A.W. Sleight, *J. Phys. Chem.* **89** (1985) 2493.
[83.] W.E. Farneth, R.H. Staley, and A.W. Sleight, *J. Am. Chem. Soc.* **108** (1986) 2327.
[84.] J.S. Chung, R. Miranda, and C.O. Bennett, *J. Catal.* **114** (1988) 398.
[85.] C.J. Machiels and A.W. Sleight, *J. Catal.* **76** (1982) 238.
[86.] C.J. Machiels and A.W. Sleight, *in* "The Chemistry and Uses of Molybdenum" Proceedings of the 5nd Int. Conference, p. 250, Climax Mo. Co., Ann Arbor, MI (1982).
[87.] R.P. Groff, *J. Catal.* **86** (1984) 215.
[88.] J.S. Chung, R. Miranda, and C.O. Bennett, *Chem. Soc. Faraday Trans. I* **81** (1985) 19.
[89.] J.S. Chung and C.O. Bennett, *J. Catal.* **92** (1985) 173.

[90.] W.-H. Cheng, *J. Catal.* **158** (1996) 477.

3

Experimental Method

3.1 Introduction

In this chapter, an overview of the experimental techniques and instruments used during the course of this thesis is presented. First, scanning probe microscopies are described. The procedures used to grow single crystals of the molybdenum oxides are then presented. These procedures are summarized in Table 3.1. The structural parameters and electronic properties of the molybdates have been determined and are summarized in Table 3.2. Finally, a general description of the reaction system and the procedures used to study the evolution of the MoO_3(010) surface is presented. Specific experimental treatment procedures and conditions are described in later chapters, where they are relevant.

3.2 Scanning Probe Microscopy (SPM)

Scanning Probe Microscopy (SPM) encompasses a class of real space, surface structure probes which rely on rastering a probe (tip) over a sample to produce a topographic map of the sample's surface structure. In many ways, the techniques are similar to stylus-type profilometers which have been used to characterize surfaces in the past. However, this newer class of profilometers offers exceptional surface resolution, down to the atomic scale. This unprecedented resolution is achieved by using precise piezoelectric scanners and highly sensitive mechanisms of surface detection. The mechanism by which the surface is "sensed" is the primary feature that distinguishes the different SPM techniques. In this section, the SPMs used during the course of this study, scanning tunneling microscopy (STM), contact atomic force microscopy (AFM), and noncontact atomic force microscopy (NC AFM), are described. More detailed discussions of the theory and operational principles behind these instruments can be found in the many reviews that have been published in recent years [1-6].

3.2.1 Scanning Tunneling Microscopy (STM)

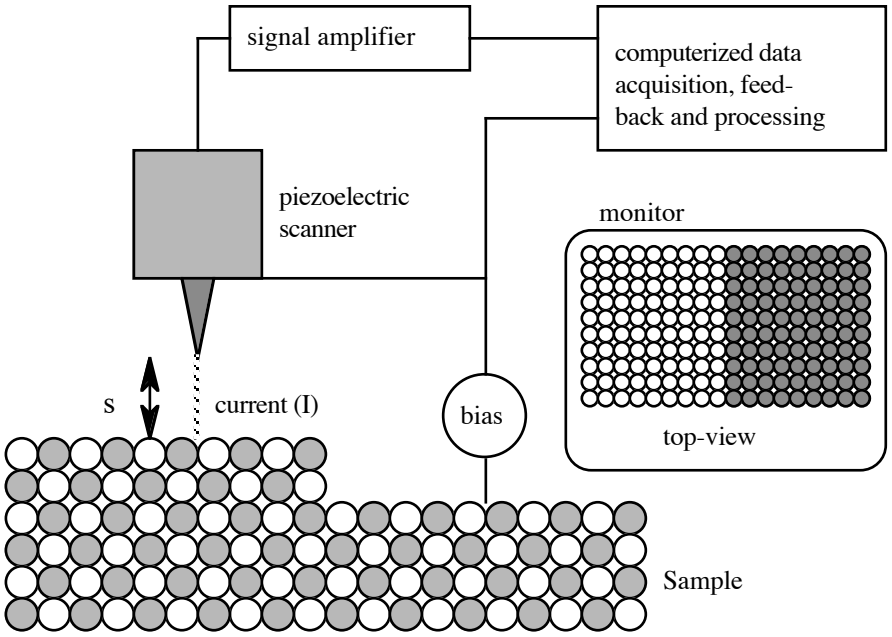

Figure 3.1 Schematic representation of the scanning tunneling microscope (STM). During operation, the sample is biased relative to the tip and a tunneling current is established between the two. While scanning, the feedback system maintains a constant current by adjusting the tip-to-sample separation, **s**. Plotting the z scanner response, as a function of x and y, provides a topographic map of the sample surface.

The scanning tunneling microscope was invented in 1982 by Binnig and Röhrer at IBM [7] and a schematic representation of the instrument is shown in Fig. 3.1. The sensing mechanism that the STM uses is a tunneling current between the tip and the sample. When the tip (a sharp Pt or W wire) is positioned a few angstroms above an electrically conducting sample that is biased (with respect to the tip), electrons tunnel between the two electrodes and a continuous tunneling current may be established. This tunneling current has an inverse exponential dependence on the separation, **s**, between the tip and the sample and, therefore, provides a very sensitive measure of the tip-to-sample separation.

During operation in *constant current* mode, the tip's vertical position above the sample is controlled by a feedback circuit which constantly compares the measured tunneling current to an experimentally fixed (set point) value. If the measured and set point currents are not equal, the tip-to-sample separation is adjusted such that the desired current level is maintained. If the measured current is too low, the tip is moved closer to the sample by the piezoelectric scanner and, conversely, if the current is too high, the tip is moved away from the sample. As the tip is scanned across the sample, the piezoelectric scanner's vertical response is recorded as a function of the tip's **x** and **y** positions on the sample surface. This data can be displayed as a topographic map of the sample's surface structure. If a relatively constant current is maintained while scanning,

the tip will follow the surface topography with an accuracy of approximately ±0.1 Å. In this thesis, constant current data are presented in the form of gray scale images in which the black-to-white contrast corresponds to the topographic height of the features on the surface. White features are the highest and black features are the lowest. An alternate approach is to collect *constant height* data. In this case, the tip is scanned over the sample at a constant height while the tunneling current is measured as a function of position on the surface. Here, the image contrast corresponds to the measured tunneling current as a function of position.

The description of STM presented above is a simplified one and, in fact, the tunneling current between the tip and sample is dependent on more than just the tip-to-sample separation. In particular, the tunneling current also depends on the local electronic structure of the sample's surface. When scanning over large areas, the atomic scale variations in the electronic structure of the surface are not resolvable because the distance between experimental sampling points is greater than the interatomic distances on the surface. As a result, the STM image can be taken as a direct representation of surface topography. When scanning over very small areas, less than $(100\ \text{nm})^2$, local variations in the electronic structure from atom to atom (i.e. the spatial distribution of the electron wave functions) can alter the tunneling probability. Therefore, contrast at the atomic scale cannot be interpreted as a simple topograph. In order to understand the atomic scale contrast, we must explicitly consider the electronic structure of the surface.

Interpretation of Atomic Resolution STM Images. Ignoring tip-sample force interactions and assuming that the tip is atomically sharp, the constant current STM image represents the partial density of states of the surface at a given energy level [6]. This energy is experimentally fixed by the bias applied between the tip and the sample. For small applied biases ($|V| < 1.0$ V), states around the sample's Fermi level (e_f) are sampled and the image can be taken to represent the partial density of states at the Fermi level, $\rho(r_0,e_f)$. With larger biases, energy levels above or below e_f are also sampled, but the probability of tunneling to or from states near e_f remains the highest.

In most metals, the density of states $\rho(r_0,e)$ or atomic wave functions do not vary significantly with energy near the Fermi level. Therefore, the STM contrast is, essentially, independent of the experimental imaging bias and the STM image may be approximated as an atomic scale topograph of the surface [8]. In covalently bonded semiconductors (i.e. GaAs, Si, Ge), on the other hand, the partial density of states $\rho(r_0,e)$ may vary drastically as a function of energy (bias) and the contrast in STM images will reflect this bias dependence. When the sample is biased negative (with respect to the tip),

electrons tunnel from the valence band of the semiconductor to the conduction band of the tip. With positive samples biases, electrons tunnel from the tip to the semiconductor's conduction band. The corresponding STM images will reflect the spatial distribution of the valence and conduction band wave functions, respectively. Therefore, when the sample is biased negative, the atoms to which the valence band states are localized are selectively imaged and with positive biases, those atoms to which the conduction band states are localized are imaged. For example, on the GaAs(110) surface, conduction band states are localized at the Ga atoms while valence states are localized at the As atoms and, as a result, images acquired with negative sample biases reveal the As atoms while those acquired with positive biases reveal the Ga atoms [9].

Atomic resolution STM images of transition metal oxide surfaces are frequently interpreted in the same way as covalently bonded semiconductors; it is assumed that filled states images (negative samples bias) show the more electronegative atoms (oxygen) while empty states images reveal the more electropositive ones (metal). While this is a reasonable approximation, there are conditions under which this interpretation will fail. For example, although the cation d-orbitals dominate the density of states near the bottom of an oxide's conduction band, the O 2p states make a significant contribution near the top of this band. Thus, depending on the experimental imaging bias, the tip could be more sensitive to the anions even when probing empty states. A second important consideration is the geometric configuration of the atoms at the surface. Because the tunneling current has an inverse exponential dependence on the tip-to-sample separation, the tip is more sensitive to atoms which protrude from the surface. The possible coordination environments in transition metal oxides leads to speculation that this 'geometric factor' can play a significant role in STM image contrast. For example, on a surface terminated by MO_6 octahedra in axial alignments, the oxygen atoms which terminate the surface are more than 1.5 Å closer to the STM tip than the underlying metal atoms. As a result, the possibility of resolving the O atoms in empty states images can not be ruled out. There is a relatively simple and safe approximation of STM image contrast for transition metal oxides. One may assume that the metal-oxygen polyhedra are imaged collectively. This model is used to interpret the SPM images of the molybdate surfaces described in Chapter 4.

Experimental Equipment and Procedure. All of the STM images presented in this thesis were acquired with one of three microscopes; a RHK STM100, a Park Scientific Instruments (PSI) AutoProbe CP, or a Digital Instruments (DI) Nanoscope III. The PSI and DI instruments are multimode SPMs (they can be used for other scanned probe

techniques, such as AFM). The PSI SPM was operated exclusively in the ambient atmosphere while the DI instrument could be operated in the ambient or in an Ar atmosphere which was free of water and oxygen impurities (H_2O and O_2 < 5 ppm). In the later case, the microscope was enclosed in a commercial glove box (Vacuum Atmospheres) with a continuously purified Ar atmosphere. The RHK microscope is a dedicated STM that may be operated in UHV (base pressure less than $1x10^{-9}$ Torr) or the ambient.

All STM measurements were made with mechanically clipped Pt-10%Ir tips (Sigmund Cohn Inc., d = 0.254 mm). Constant current data were recorded with tunneling currents between 0.5 and 2 nA and biases between -3.0 and 3.0 V. During ambient imaging, smaller biases were generally used, between -1.0 and 1.0 V. Unless otherwise indicated, the images presented here were acquired on cleavage surfaces. For UHV measurements, the single crystals were cleaved in one of two ways: in a N_2 filled glove bag that was attached to a load-lock on the UHV chamber or on a cleavage stage within the UHV chamber (*in situ*).

3.2.2 Atomic Force Microscopy (AFM)

The atomic force microscope (AFM) [5], shown schematically in Fig. 3.2a, uses the same piezo driven scanning mechanism as the STM. In contact AFM, the repulsive force between the atoms of the sample and the atoms of the tip is used to 'sense' the surface. The tip is a sharp (radius of curvature less than 250 Å) Si cone or Si_3N_4 pyramid mounted on a small, flexible cantilever (of the same material) with a very low spring constant. The cantilever and tip are shown schematically in Fig. 3.2b. As the tip is scanned over the sample's surface, the cantilever deflects in response to the surface's topography. The deflection of the cantilever is measured by reflecting a laser beam off of the back of the cantilever onto a split, position sensitive photo detector (PSPD). As the cantilever deflects, the position of the laser spot on the detector changes and this change in laser position provides a sensitive measure of the cantilever's deflection.

The AFM may be operated in either the *constant force* or the *constant height* mode. During constant force imaging, the system's feedback loop maintains a nearly constant cantilever deflection (constant force) by adjusting the height of the sample with the z piezoelectric scanner. The changes in piezo height are collected as a function of position and, then, rendered as a topographic map of the sample's surface. During constant height imaging, the vertical (z) positions of the sample and tip are fixed and the deflection of the cantilever is measured as a function of position. Constant force imaging is the most common mode of contact operation and was used exclusively in this study.

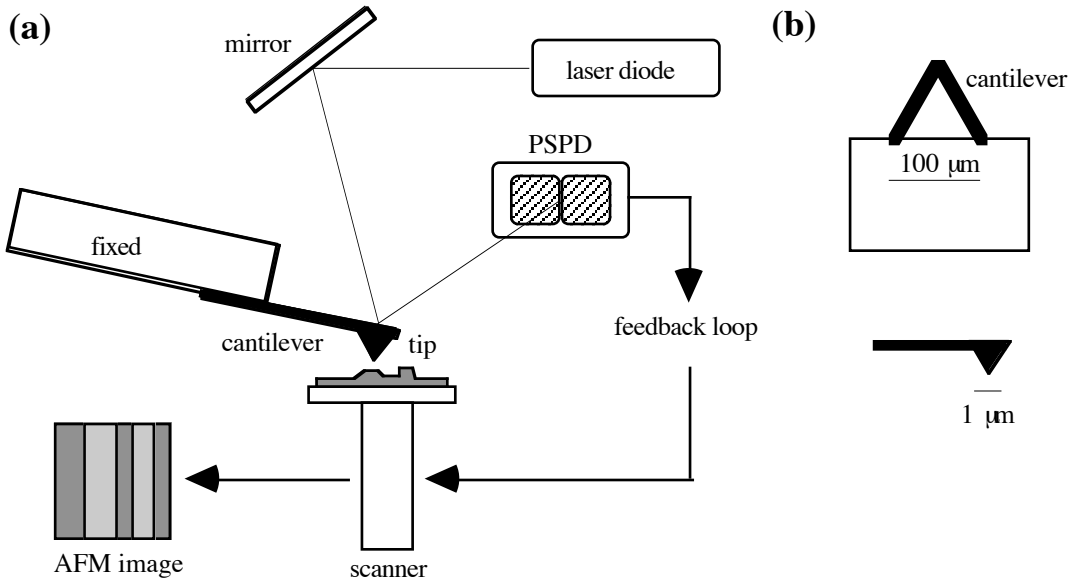

Figure 3.2 (a) Schematic representation of the AFM. During operation in contact mode, the feedback loop maintains a constant cantilever deflection (constant force) by adjusting the height of the sample relative to the cantilever. The up and down motion of the scanner, as a function of position on the sample, provides a topographic map of the sample's surface structure. (b) The AFM cantilever and tip.

There are two ways to represent constant force data. Most commonly, data are presented topographically and the image provides a map of surface topography. In these gray scale images, white features have the greatest topographic height on the surface while dark features have the lowest. Because the human eye has a fixed and rather small dynamic range, it is not possible to distinguish more than 256 shades of gray. In some cases, very high or low features dominate this contrast range and smaller features, although resolved by the probe, can not be represented in a conventional topograph. By plotting the deflection of the cantilever during constant force operation (deflection image), one can emphasize changes in topography rather than absolute heights so that the fine scale features of the surface can be seen more clearly. While the system strives to maintain a constant cantilever deflection, it always takes a finite, though short, period for the system to attain this consistency. The cantilever deflection is always pronounced when there is an abrupt change in surface topography (height). Plotting cantilever deflection as a function of position brings these boundaries out. In the deflection image, most of the surface exhibits the same (constant) deflection and appears as a gray contrast, however, the boundaries between adjacent regions of different height are a pronounced black or white contrast (black if the cantilever deflects down, white if it deflects up).

Noncontact (NC) AFM. In noncontact (NC) AFM, the surface sensing mechanism is based on the attractive, primarily van der Waals, forces between the AFM tip and the sample. These forces are longer range and, as a result, the tip does not usually touch the sample while it is scanned over the surface. During noncontact imaging, the cantilever-tip is maintained between 25 and 100 Å above the surface and vibrated at a constant frequency (near its mechanical resonance frequency, 100 kHz) with an amplitude of 10 to 30 Å. As the resonating tip is scanned over the surface, it's vibration amplitude changes in response to gradients in the attractive force between the tip and the sample. These gradients are a function of the tip-to-sample separation. The system's feedback mechanism maintains a nearly constant cantilever vibration amplitude by adjusting and restoring the tip-to-sample separation. The amount of scanner movement, needed to maintain the constant separation (constant vibration amplitude), is used to generate a topographic map of the surface.

Interpretation of AFM Data. The interpretation of large scale AFM data is straight-forward and the image can generally be taken as a topographic map of the surface structure. However, image artifacts, that lead to an inaccurate depiction of the surface structure, are possible. Artifacts are particularly probable when imaging surface features with dimensions smaller than the radius of the probe tip. For example, very small, sharp features which protrude from the surface (such as whiskers or pyramids) may actually function as the 'tip' during imaging. When such features are encountered on the surface, the AFM tip shape will be formed in the image rather than the feature shape. A tell tale sign of this artifact is an image in which the same rounded or squared shape is replicated over and over with the same aspect ratio. If small pits are present on the surface, the finite size of the probe dictates that these features will appear smaller and, perhaps, shallower than they really are. Similar artifacts are also possible in STM images and, in general, care must be taken when interpreting SPM images that contain features with dimensions comparable to the size of the tip.

AFM images of some surfaces may exhibit atomic scale contrast. However, the mechanism by which this contrast arises is not understood. The possibility of probing with an atomically sharp tip is unlikely and, if this tip geometry was realized, the pressure exerted by the tip on the sample (for applied forces as low as 0.1 nN) would be many times larger than the yield stress of diamond [10]. One viable explanation for atomic scale contrast relies on sliding planes of the sample over itself. For example, a flake of the sample sticks to the AFM probe and then slides over the layers below it during imaging. Similarly, one can imagine an AFM tip terminated by an atomically flat

surface. The high and low spots in the image could then correspond to the times when the atoms of the tip and sample slide in and out of registry [11]. Because both of these explanations rely on a cooperative imaging mechanism, true atomic resolution is unlikely and it has not yet been demonstrated that point defects can be resolved with ambient AFM. While the active imaging mechanism remains obscure, 'atomic' resolution AFM images of a number of materials (for example, Au [12], graphite, MoS_2, BN [13], NaCl [14]) have been reported and it is generally possible to interpret these images based on the expected surface termination of the material.

Experimental Equipment and Procedure. Contact AFM observations were made with a Park Scientific Instruments (PSI) AutoProbe CP and a Digital Instruments (DI) NanoScope E. All noncontact (NC) measurements were made on the PSI SPM. Both instruments operate in the ambient and the DI instrument can also be operated in a glove box with an inert Ar environment. Data recorded on the DI AFM were obtained using Si_3N_4 cantilevers which had pyramidal tips of nominal radius less than 200 Å and a force constant of approximately 0.05 N/m. In addition to the above Si_3N_4 tips, Au coated Si cantilevers were utilized on the PSI instrument. These Si cantilevers have conical Si tips with a radius of curvature of only 100 Å and a force constant of 0.16 N/m. Typical force set points were between 1 and 8 nN for contact AFM and -0.1 to -0.8 nN for NC AFM.

3.3 Single Crystal Growth of the Molybdenum Oxides

Single crystals of molybdenum oxide phases, with compositions between MoO_3 and MoO_2, can be grown by chemical vapor transport (CVT) or "mineralization" reactions. A thorough review of these techniques may be found in Schafer's "Chemical Transport Reactions" [15]. In all cases, the growth reactions were carried out in sealed, evacuated, quartz ampoules. A small amount of a halogen gas (Cl_2 or I_2) was used as a transport or mineralization agent. $TeCl_4$ and iodine provided convenient solid sources for the agents; $TeCl_4$ decomposes at the reaction temperatures ($T > 250$ ˚C) to liberate Cl_2 while iodine boils ($T > 200$ ˚C). CVT and mineralization reactions are differentiated by the manner in which the reaction vessel is heat treated. During CVT, the ampoule is heated in a temperature gradient (5 ˚C $\leq \Delta T \leq 100$ ˚C) and crystals are grown by transport of the oxide along the length of the tube from the source zone to the crystallization zone. Mineralization reactions, on the other hand, are conducted under isothermal conditions and growth is a coarsening reaction. All of the Mo-O phases grown by CVT were transported down a temperature gradient from the hot (source) zone to the cold (crystallization) zone. The crystal growth parameters for the Mo-O phases are summarized in Table 3.1.

3.3.1 α-MoO_3

Large single crystals of α-MoO_3 were grown by chemical vapor transport (CVT) using $TeCl_4$ as a transport agent. In a standard growth, a quartz tube (I.D. = 13 mm) was charged with 0.05 g/cm^3 of α-MoO_3 powder (99%, Johnson Matthey) and 0.004 g/cm^3 of $TeCl_4$ (99.9%, Akros, Fisher Scientific) in a glove box with an inert Ar atmosphere ([H_2O] < 5 ppm, [O_2] < 2 ppm). Prior to loading, the MoO_3 powder was ignited in air at 500˚C for 2 h to ensure dryness. The loaded tube was then placed in a desiccator (containing P_2O_5) and transferred to a N_2 filled glove bag. The tube was then secured to a stop cock, transferred to a vacuum manifold, and evacuated to P < 4 x 10^{-5} atm. Finally, the tube was sealed to form an ampoule approximately 10 cm in length.

Crystal growth was accomplished by heating the ampoule in a horizontal tube furnace with the temperature graded from 520 ˚C to 500 ˚C along its length. Prior to growth, the tube was backreacted (by heating it in a reversed temperature gradient) for several hours to cleanse the crystallization zone of powder particles and eliminate the possibility of pre-existing MoO_3 nuclei. This step limits the total number of crystals which form and helps ensure large single crystals with minimal intergrowth between them. Within 5 days, transparent, green-yellow crystals with dimensions as large as 7 x 4 x 2 mm^3 could be harvested from the cool end of the tube. Crystals were always platy, with large {010} facets that were elongated along <001>. The {hk0} and {001} faces were also well developed and had areas of up to 7 x 2 and 4 x 2 mm^2, respectively.

MoO_3 single crystals were also grown by sublimation of the oxide in the ambient atmosphere. This technique is commonly employed to produce coarse MoO_3 catalyst samples and, therefore, the structure of these growth surfaces is of a practical interest. First, approximately 5 g of MoO_3 powder was charged into the bottom of an open ended quartz tube (d = 3 cm, l = 20 cm). The tube was then positioned in a horizontal tube furnace such that the closed (charge) end was at the center of the furnace and the open end extended just outside the furnace. To initiate growth the charge was heated to 720 ˚C and maintained at this temperature for 2-3 days. The tube was then removed from the furnace and cooled to room temperature so that the single crystals could be harvested. Crystals grown by sublimation are generally needle or plank-like and less than 50 μm thick along <010>. The long axis of the crystal is always <001> and may exceed 15 mm. Along <100>, the crystals' dimensions are typically on the order of 0.25 to 1 mm.

3.3.2 $Mo_{18}O_{52}$

Single crystals of $Mo_{18}O_{52}$ were grown by mineralization following a procedure similar to that described by Bertrand et al. [16]. First, a finely ground mixture of MoO_3 (99%, Johnson Matthey) and Mo (99.9%, Johnson Matthey) powder (0.075 g/cm^3) was loaded into a quartz tube with an inner diameter of 11 mm. The tube was then flamed *in vacuo* to drive off residual water vapor. The tube was then vented in the ambient and 0.005 g/cm^3 of I_2 (99%, Johnson Matthey) was quickly added to the vessel. It was then evacuated ($P < 4 \times 10^{-5}$ atm) and, finally, sealed to form an ampoule approximately 10 cm in length. Typically, stoichiometric mixtures of MoO_3 and Mo (O/Mo = 2.89) were employed. However, the phase's formation is not particularly sensitive to charge composition and powders with compositions between $MoO_{2.890}$ and $MoO_{2.93}$ yielded $Mo_{18}O_{52}$ crystals. Prior to growth, the powder charge was distributed evenly along the length of the ampoule and it was then centered in a horizontal tube furnace. The center of the reaction vessel was annealed at 677 ˚C, while the ends were at a slightly lower temperature (approximately 667 ˚C).

Within a week, platy black crystals of $Mo_{18}O_{52}$ could be harvested along the length of the tube. Crystals grown in this manner have well developed {100} facets and dimensions as large as 7 x 5 x 0.5 mm^3. The crystals were almost always found with crystals of other molybdenum suboxides (such as γ-Mo_4O_{11} and Mo_8O_{23}). However, the distinct morphology and color of the different phases make segregation trivial. While a net transport of reactants along the length of the tube was rarely evident, isothermal experiments, conducted in a box furnace, showed that a small temperature gradient was needed to grow large crystals. On the other hand, isothermal heat treatments did tend to yield a single phase product of small $Mo_{18}O_{52}$ crystals. Finally, it is important to point out that $Mo_{18}O_{52}$ is a member of a closely related family of crystallographic shear compounds of the general formula Mo_nO_{3n-2} [17]. Therefore, identification of this phase by powder XRD does not rule out the possibility that the crystals may contain up to 5 vol% of related compounds such as $Mo_{19}O_{55}$ or $Mo_{20}O_{58}$ [18,19].

3.3.3 $Li_xMo_{18}O_{52}$

Single crystal of Li doped $Mo_{18}O_{52}$ were grown from the melt by a procedure similar to the gradient flux technique which Greenblatt et al. [20,21] have applied to the growth of alkali molybdenum oxide bronzes. First, 10 g of a 6.25 to 1 molar ratio of MoO_3 and $Li_{0.25}MoO_3$ powders were mixed, dried under vacuum, and sealed in an evacuated quartz tube to form an ampoule with an 11 mm inner diameter and 80 mm length. The ampoule was then heated to 850 ˚C, held there for 4 h, and cooled to 400 ˚C at 4.5 ˚C/h while a 10 ˚C to 20 ˚C temperature gradient was maintained across the vessel.

The solid product obtained consisted of many, mm sized, platy, black crystals of $Li_xMo_{18}O_{52}$ within a finer grained matrix of MoO_3. X-ray analysis revealed that these $Li_xMo_{18}O_{52}$ crystals were isostructural with $Mo_{18}O_{52}$. The melt grown crystals are distinguished from those grown from the vapor because the electronic conductivity of melt grown $Mo_{18}O_{52}$ is four times greater. The likely explanation for this greater conductivity is that these crystals are intercalated with a small amount of Li which donates electrons to the conduction band.

$Li_{0.25}MoO_3$ was obtained by ion exchanging $Na_{0.25}MoO_3$ in a 1 M LiCl (99.9%, Aldrich) solution for one week. $Na_{0.25}MoO_3$ was prepared by reacting 5 g of α-MoO_3 powder for 4 h at room temperature with a 500 ml solution of 5 g $Na_2S_2O_4$ (reagent grade, Fisher Scientific) and 40 g Na_2MoO_4 (99%, Aldrich) in distilled water [22].

3.3.4 Mo_8O_{23}

Single crystals of Mo_8O_{23} were grown by a mineralization reaction similar to that used to obtain $Mo_{18}O_{52}$ single crystals. First, a finely ground mixture of MoO_3 (99%, Johnson Matthey) and Mo (99.9%, Johnson Matthey) with a composition between $MoO_{2.89}$ and $MoO_{2.87}$ was prepared. 0.05 g/cm^3 of this mixture was then loaded into a quartz tube (I.D. = 13 mm) and flamed *in vacuo* to drive off residual water vapor. 0.0005 g/cm^3 of I_2 was then added to the tube before it was evacuated ($P < 4 \times 10^{-5}$ atm) and sealed to form an ampoule approximately 10 cm in length. The powder charge was distributed evenly along the length of the ampoule and the vessel was annealed isothermally at 690 ˚C for four to seven days. Isothermal conditions were ensured by packing the tubes in Al_2O_3 powder beds and heating in the center of a large muffle furnace.

At the conclusion of the anneal, between 10 and 20 large, barrel shaped crystals of Mo_8O_{23} could be harvested from the length of the silica ampoule. If isothermal conditions were ensured, only large crystals of the desired phase were found in the vessel. These crystals have a very distinct barrel shaped habit, with flat, well developed, metallic pink, {010} faces capping the barrel and silvery black {100}, {001}, and {h0l} faces forming the circumference of the barrel.

3.3.5 γ-Mo_4O_{11}

Single crystals of γ-Mo_4O_{11} were grown by CVT using iodine as a transport agent. First, 0.075 g/cm^3 of powder of the composition $MoO_{2.76}$ (consisting of a finely ground mixture of Mo and MoO_3) was charged into a silica tube (I.D. = 13 mm) and flamed *in vacuo*. 0.0005 g/cm^3 of I_2 was added and the tube was evacuated. The tube was then sealed ($P < 4 \times 10^{-5}$ atm) to form an ampoule approximately 10 cm in length.

The powder charge was distributed evenly along the source zone of the tube and the ampoule was back reacted for several hours in a reversed temperature gradient to cleanse the crystallization zone. Crystal growth was accomplished by annealing the ampoule in a temperature gradient, 690 ˚C (source) to approximately 650 ˚C (crystallization zone), in a horizontal tube furnace. Within a week of reaction, platy, metallic purple crystals could be harvested from the cool end of the ampoule and the cooler portion of the charge powder bed. Typically, Mo_4O_{11} was the only phase present, although, occasionally one or two crystals of MoO_3, $Mo_{18}O_{52}$ or Mo_8O_{23} could also be found. The single crystals had dimensions as large as 6 x 3 x 0.3 mm^3.

Table 3.1 Crystal Growth Parameters of the Molybdenum Oxides.

Phase	Powder Charge	Transport Agent	Annealing Conditions	Crystal Habit
MoO_3	0.05 g/cm^3 of α-MoO_3	0.004 g/cm^3 of $TeCl_4$	T_{source} = 520°C $T_{cryst.}$ = 500°C t ~ 5 days	green-yellow plates 7 x 3 x 2 mm^3
	5 g of α-MoO_3	Ambient (sublimation)	720 - 600 °C t ~ 3 days	yellow planks 15 x 1 x 0.1 mm^3
$Mo_{18}O_{52}$	0.05 g/cm^3 of $MoO_{2.91}$ (MoO_3 + Mo)	0.005 g/cm^3 of I_2	T_{source} = 677°C $T_{cryst.}$ = 667°C t ~ 7 days	black plates 7 x 5 x 0.5 mm^3
$Li_xMo_{18}O_{52}$	6.25 : 1 (molar) mix of MoO_3 and $Li_{0.25}MoO_3$	melt grown N.A.	850°C for 4 h cooled to 400°C at 4.5°C/h	black-purple plates 4 x 2 x 0.5 mm^3
Mo_8O_{23}	0.05 g/cm^3 of $MoO_{2.88}$ (MoO_3 + Mo)	0.0005 g/cm^3 of I_2	isothermal anneal at 690°C for one week	black-purple barrels 3 x 3 x 5 mm^3
γ - Mo_4O_{11}	0.075 g/cm^3 of $MoO_{2.76}$ (MoO_3 + Mo)	0.0005 g/cm^3 of I_2	T_{source} = 690°C $T_{cryst.}$ = 650°C t ~ 7 days	metallic purple plates 6 x 3 x 0.3 mm^3
η - Mo_4O_{11}	0.075 g/cm^3 of $MoO_{2.76}$ (MoO_3 + Mo)	0.004 g/cm^3 of $TeCl_4$	T_{source} = 525°C $T_{cryst.}$ = 490°C t ~ 7 days	wine red plates 7 x 4 x 0.3 mm^3

3.3.6 η-Mo_4O_{11}

η-Mo_4O_{11} crystals were grown by CVT using chlorine as a transport agent. First, 0.075 g/cm^3 of powder of the composition $MoO_{2.76}$ (consisting of a finely ground mixture of Mo and MoO_3) was charged into a silica tube (I.D. = 13 mm) and flamed *in vacuo*. The tube was vented in a N_2 filled glove bag and approximately 0.004 g/cm^3 of $TeCl_4$ was added. The tube was then evacuated and sealed ($P < 4 \times 10^{-5}$ atm) to form an ampoule approximately 10 cm in length. The vessel was then annealed (after segregating the charge to one end of the vessel and backreacting) in a temperature gradient, 525 °C (source) to ~ 490 °C (crystallization), in a horizontal tube furnace. Within a week of reaction, platy, metallic, wine red crystals could be harvested from the cool end of the ampoule. The crystals obtained at this temperature and composition are always η-Mo_4O_{11} and exhibit dimensions as large as 7 x 4 x 0.3 mm^3, with the {100} faces the most well developed.

3.4 Bulk Characterization of Mo-O Single Crystals

Pulverized single crystals of each phase were analyzed using standard powder X-ray diffraction methods to confirm their identity and establish lattice parameters. All samples were analyzed on a Rigaku Θ-2Θ X-ray diffractometer using Cu K_α radiation which was generated with a source operating at 35 kV and 25 mA. The diffraction data was refined, using a least squares method (UNIX based program Finax), to obtain lattice parameters. For all samples, at least 15 diffraction peaks were included in the refinement. A summary of the experimental and published lattice parameters for each phase can be found in Table 3.2. The room temperature sheet resistivity of single crystal samples was determined using a standard four point resistivity procedure. Measurements were facilitated by a commercial (Signatone, S-301-4), linear, 4-point setup with spring loaded metal contacts spaced 1 mm apart. Currents between 1 nA and 100 mA were applied with a constant current source (Keithley, 224) while the voltage was measured with a digital multimeter (Keithley, 197) to within ± 0.001 mV. In general, the measured bias displayed a linear dependence on the applied current. The geometric correction factors derived by Smits [23] were applied to establish the specific resistivity. Plots of the measured voltage (V) as a function of the applied current (I) may be found in Figures 3.3 through 3.6 and the experimentally determined specific resistivities of each phase are summarized in Table 3.2.

Table 3.2 Room Temperature Crystalline and Electronic Parameters of the Molybdenum Oxides.

Phase	Space Group	Experimental Lattice Parameters	Published Lattice Parameters	ρ (Ω-cm)
MoO_3	Pbnm	a = 3.9664(9) Å b = 13.8685(30) Å c = 3.7012(9) Å	a = 3.9628 Å b = 13.855 Å [24] c = 3.6964 Å	insulator
$Mo_{18}O_{52}$	$P\bar{1}$	a = 8.097(23) Å b = 11.812(28) Å c = 21.415(43) Å α = 102.22(22) ° β = 68.43(22) ° γ = 109.46(28) °	a = 8.145 Å b = 11.89 Å c = 21.23 Å [17] α = 102.67 ° β = 67.82 ° γ = 109.97 °	78.1
$Li_xMo_{18}O_{52}$	$P\bar{1}$	-	-	17.2
Mo_8O_{23}	P 2/a	a = 16.9077(67) Å b = 4.0549(15) Å c = 13.3982(47) Å β = 106.364 (44) °	a = 16.88 Å b = 4.052 Å [25] c = 13.39 Å β = 106.19 °	7.01
γ - Mo_4O_{11}	Pnma	a = 24.49 Å b = 5.457 Å c = 6.752 Å	a = 24.49 Å b = 5.457 Å [26] c = 6.752 Å	-
η - Mo_4O_{11}	$P2_1/a$	a = 24.649(13)Å b = 5.4424(27) Å c = 6.7065(29) Å β = 94.369(48) °	a = 24.54 Å b = 5.439 Å [26] c = 6.701 Å β = 94.28 °	1.66×10^{-4}

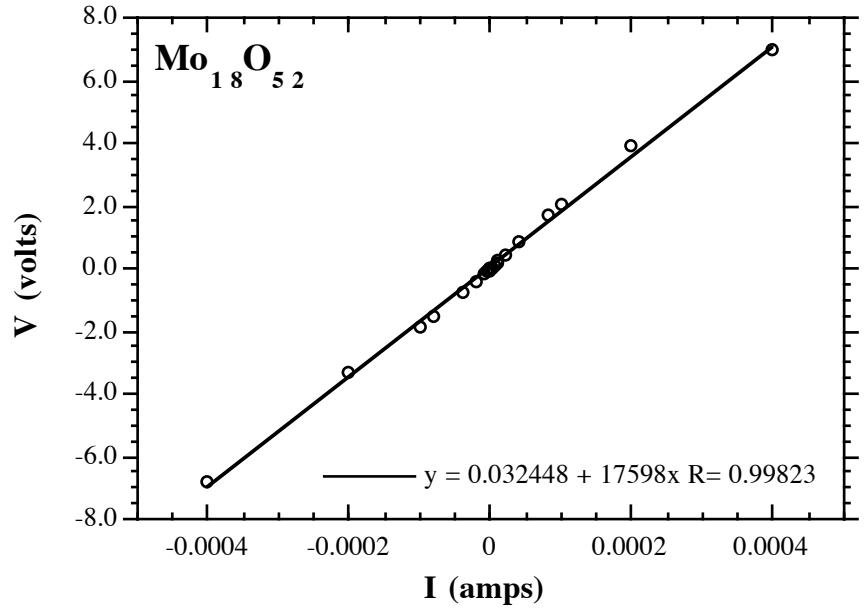

Figure 3.3 Four point resistivity data for $Mo_{18}O_{52}$.

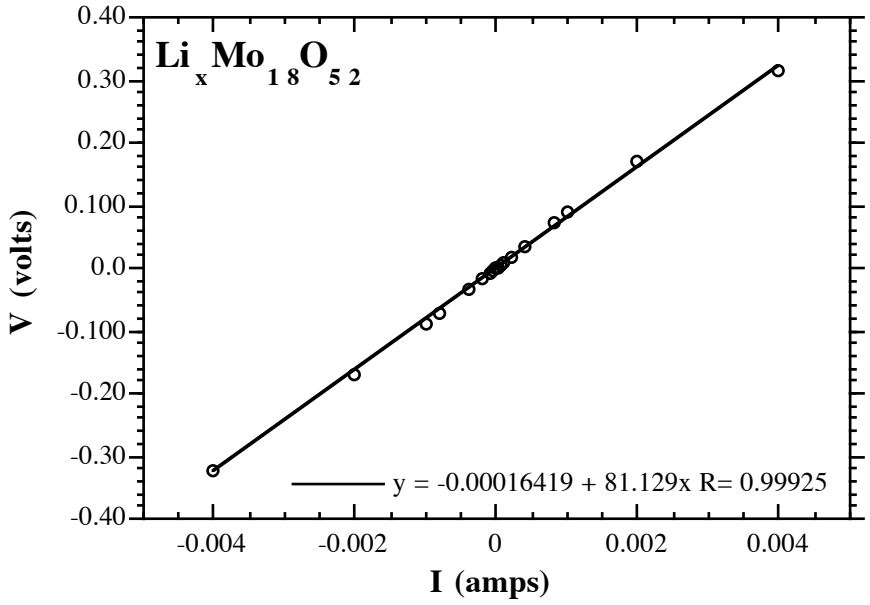

Figure 3.4 Four point resistivity data for Li doped $Mo_{18}O_{52}$.

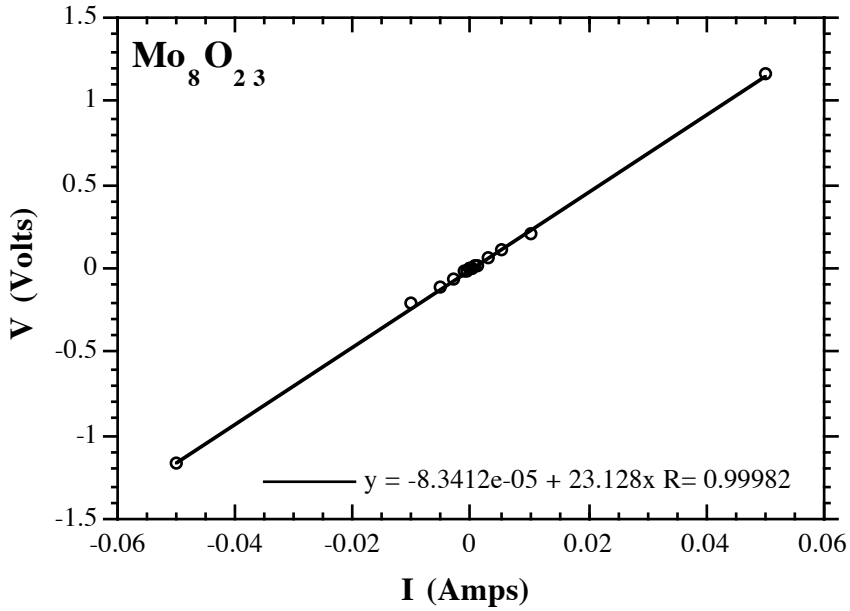

Figure 3.5 Four point resistivity data for Mo_8O_{23}.

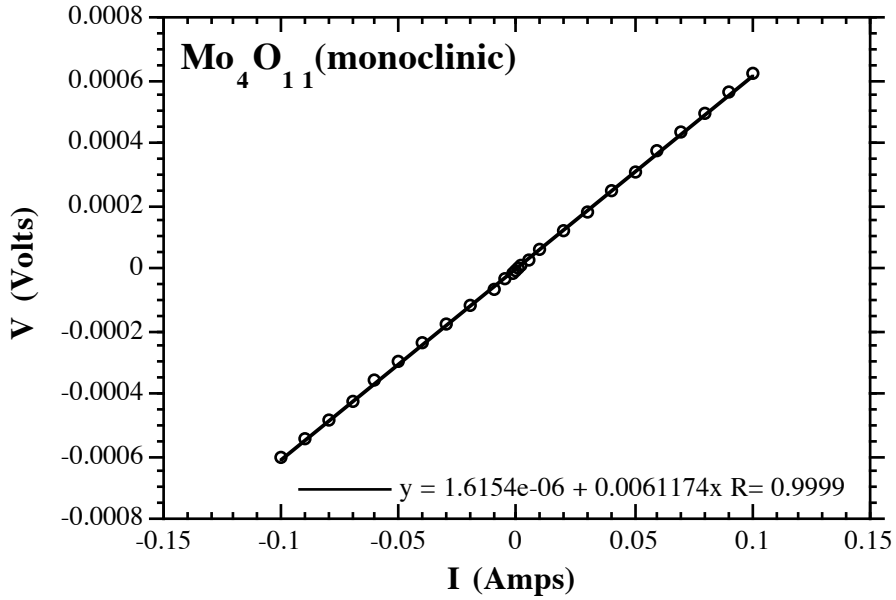

Figure 3.6 Four point resistivity data for η-Mo_4O_{11}.

3.5 Catalytic Reactions

3.5.1 Single Crystal Reactor

The single crystal reactor used for the surface evolution studies is shown schematically in Fig. 3.7. The reaction vessel consisted of a quartz furnace tube (I.D. = 30 mm, O.D. = 33 mm, length = 1 m) centered in a nichrome resistance furnace. The length of the hot zone was 0.3 m. Ground glass fittings at both ends of the reaction tube ensured a vacuum tight environment and provided access for sample loading and periodic reactor cleaning. The temperature of the reactor was maintained with a commercial temperature controller (Omega) and measured with a type K (chromel-alumel) thermocouple. The thermocouple was completely enclosed in a glass sheath and fed into the hot zone of the furnace via a compression fitting.

The carrier and reactant gases were processed in various ways to remove impurities and/or fix the composition of the gas phase. If gases were "dried" they were either passed through a column of $CaSO_4$ or through a liquid nitrogen trap. The initial oxygen content of inert carrier gases, such as N_2, could be fixed by passing the gas through a bed of hot Cu coils maintained at 400 ˚C. If the carrier gas was also to be dried it was dried after the Cu scrub. In many experiments, gases were simply used as-received with nominal impurity levels. The liquid reactants were typically of high purity (99+%), however, in some cases experiments were performed, intentionally, with stocks of lower purity. Liquids were introduced into the reactor by bubbling the carrier gas through a Pyrex bubbler maintained at constant temperature (0 ˚C or 25±1 ˚C). All reactions were performed at atmospheric pressure using flow rates between 25 and 400 cc/min. Valves located along the length of the system allowed for reactor purging, switching from one gas phase to another, and gas mixing. Finally, a quartz, magnetic, transfer rod was used to move samples into (or out of) the hot zone of the reactor without exposing the system to the ambient. The transfer rod consisted of a quartz tube (l = 20 cm) with a permanent magnet sealed within. Clips, fashioned from chromel wire, were used to attach the samples or a silica boat to the transfer rod.

For low temperature reactions ($T \leq 150$ ˚C), a round bottom three-neck flask was used in place of the quartz reaction tube. The flask was contained in an insulated, resistively heated mantel. The temperature of the vessel was maintained by a temperature controller and measured with a thermocouple (type K) that was fed into the reactor by way of a compression fitting. The thermocouple was positioned directly adjacent to the single crystal sample. This apparatus was vacuum tight and could be purged in the same manner as the quartz reaction tube.

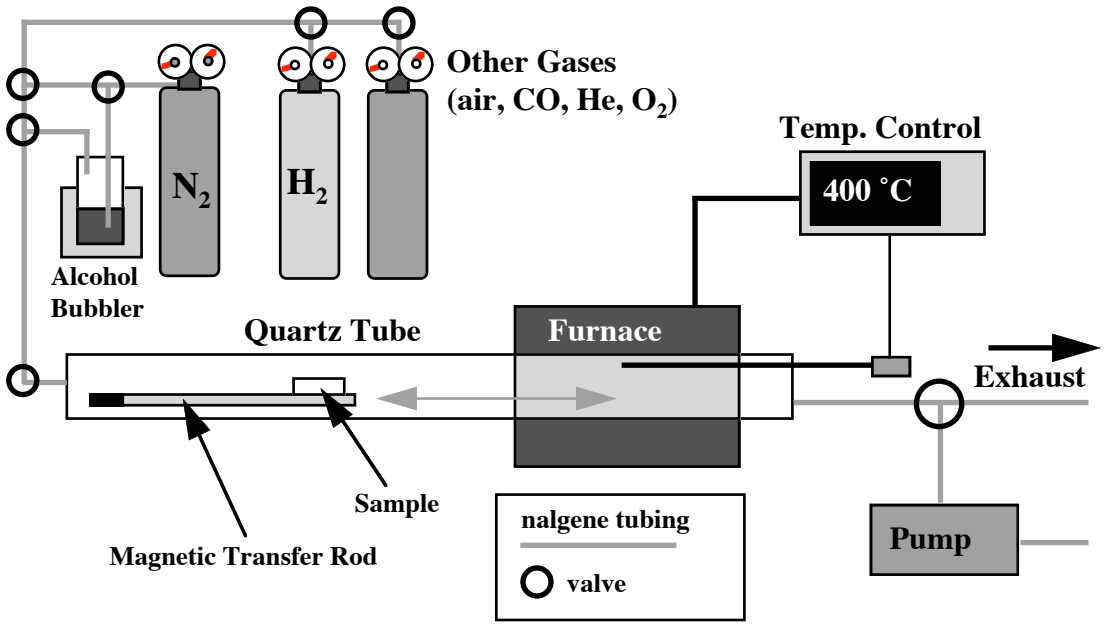

Figure 3.7 Schematic representation of the single crystal reactor. Gas drying ($CaSO_4$) and scrubbing (Cu coils) units are not depicted. The gas flow rates were measured with rotameters at the gas cylinders. See text for a complete description.

3.5.2 Catalytic Treatment Procedure

Single crystals of MoO_3 were mounted on a small, steel disc (r = 0.4 cm, t = 0.075 cm) by spot welding a thin strip of Ta foil across one of their {010} facets. Just before a sample was introduced into the reactor, it was cleaved with adhesive tape to produce a fresh (010) surface. The sample was then placed on the magnetic transfer rod and the assembly was immediately loaded into the unheated portion of the reactor (under a flow of the gas of interest at 1 atm). Experiments were also conducted on cleaved, unmounted single crystals. In this case, the crystal was cleaved with a razor blade and held in a silica boat during the reaction.

Before reacting the crystal, the reaction tube was purged. With the furnace at temperature (and the sample still in the cool zone) the reactor was evacuated for 5 min using an oil less pump. The vessel was then backfilled with the reactant gas mixture of interest to a pressure of just over 1 atm. This backfilling step was performed three times, before every heat treatment. After the purge, a continuous flow of the reactant gas was established and the sample was transferred to the hot zone with the magnetic transfer rod. Mounted samples were positioned such that the steel mount was in direct contact with the glass thermocouple sheath. If the sample was not mounted, the silica boat was positioned in contact with the sheath.

After sample introduction, the temperature of the hot zone initially drops and then rises to approximately 110% of the setpoint temperature before dropping and leveling off. It takes 5 to 10 min for the temperature to stabilize completely. The sample was reacted for a predetermined period of time at the desired temperature and gas flow rate. Following completion of the reaction period, the sample was removed from the hot zone with the magnetic transfer rod and allowed to cool to room temperature under flowing gas. The sample was then removed from the reactor for SPM analysis. The reaction time is taken to be the time between introducing the sample to the hot zone and subsequently transferring it back to the cold zone.

Sample transfer and analysis was accomplished in one of three ways. In the initial experiments, the samples were taken out of the reaction tube and immediately imaged in the ambient atmosphere. Over the AFM analysis period (several hours), changes in surface structure were never observed. During the course of this study, a glove box was acquired and this made it possible to image surfaces in a controlled atmosphere free from O_2 and water vapor. This is certainly the preferred mode of operation when dealing with reduced surfaces, which could be susceptible to reoxidation. After this system was acquired, control experiments were conducted to ensure that ambient exposure did not influence any prior results. In these experiments, the samples were reacted in a smaller reaction tube and then transferred to the glove box (in the reaction tube) without ever exposing them to the ambient. Differences between surfaces which had or had not been exposed to the ambient were never observed. This does not, however, mean that the exposed surfaces were not different. Very likely, exposed surfaces are partially hydroxylated and may, in fact, reoxidize slightly. However, at the detection level afforded by AFM, the surfaces appeared identical. Once the glove box system was in place, all subsequent imaging was done in a controlled Ar environment. In some cases, samples were transferred directly without air exposure, while, in other cases, they were exposed to the ambient momentarily before being transferred to the box.

3.6 Acknowledgments

The author thanks Dr. Weier Lu (Carnegie Mellon University) for technical assistance during the STM study of the $Mo_{18}O_{52}(100)$ surface.

3.7 References

[1.] G. Binnig and H. Röhrer, *IBM J. Res. Dev.* **30** (1986) 355.

[2.] L.E.C van de Leemput and H. van Kempen, *Rep. Prog. Phys.* **55** (1992) 1165.

[3.] D.A. Bonnell (Ed.) Scanning Tunneling Microscopy and Spectroscopy: Theory, Techniques, and Applications, VCH Publishers Inc., New York, NY (1993).

[4.] M. Tsukada, K. Kobayashi, N. Isshiki and H. Kageshima, *Surf. Sci. Rep.* **13** (1991) 265.

[5.] G. Binnig, C.F. Quate and C.H. Gerber, *Phys. Rev. Lett.* **12** (1986) 930.

[6.] S. N. Magonov and M.-H. Whanbo, Surface Analysis with STM and AFM, VCH, Weinheim, FRG (1996).

[7.] G. Binnig and H. Rohrer, *Phys. Rev. Lett.*, **49**, 57 (1982).

[8.] J. Tersoff *in* [3] pp 31-50.

[9.] R.M. Feenstra, J.A. Stoscio, J. Tersoff, and A.P. Fein, *Phys. Rev. Lett.* **58** (1987) 1192.

[10.] N. Burnham and R. Colton *in* [3] pp 191-250.

[11.] J.B. Pethica, *Phys. Rev. Lett.* **57** (1986) 3235.

[12.] S. Manne, H.J. Butt, S.A.C. Gould and P.K. Hansma, *Appl. Phys. Lett.* **56** (1990) 1758.

[13.] T.R. Albrecht and C.F. Quate, *J. Vac. Sci. Technol.* **A6** (1988) 271.

[14.] G. Meyer and N.M. Amer, *Appl. Phys. Lett.* **56** (1990) 2100.

[15.] H. Schafer, (Translated by Hans Frankfort), Chemical Transport Reactions, Academic Press, New York, NY (1964).

[16.] O. Bertrand, N. Floquet and D. Jacquot, *J. of Cryst. Growth*, **96** (1989) 708.

[17.] L. Kihlborg, *Arkiv Kemi* **21** (1963) 443.

[18.] L. Kihlborg, *Arkiv Kemi* **21** (1963) 471.

[19.] L.A. Bursill, *Acta Cryst.* **A28** (1972) 187.

[20.] M. Greenblatt, *Chem. Rev.* **88** (1988) 31.

[21.] W.H. McCarroll and M. Greenblatt, *J. Solid State Chem.* **54** (1984) 282.

[22.] D. Thomas and E. McCarron, *Mater. Res. Bull.* **21** (1986) 945.

[23.] F.M. Smits, *Bell Systems Technical Journal* **37** (1958) 711.

[24.] L. Kihlborg, *Arkiv Kemi* **21** (1963) 357.

[25.] L. Kihlborg, *Arkiv Kemi* **21** (1963) 461.

[26.] L. Kihlborg, *Arkiv Kemi* **21** (1963) 365.

4

SPM of Molybdenum Oxide Cleavage Surfaces

4.1 Introduction

In the following chapters, atomic force microscopy (AFM) will be used to identify the defects and morphological changes which develop on the MoO_3(010) surface during redox reactions. Before these experiments, precedents necessary for the interpretation of SPM images of evolving surfaces were established [1-4]. In this chapter, the contrast that is observed in STM and AFM images of four stoichiometric binary molybdenum oxide surfaces - α-MoO_3(010), $Mo_{18}O_{52}$(100), Mo_8O_{23}(010), and η-Mo_4O_{11}(100) - is described [1,3]. The MoO_3(010) surface is taken as the ideal surface structure, a corner sharing arrangement of MoO_6 octahedra similar to a (100) layer of the ReO_3 structure. When MoO_3 is reduced, oxygen deficiency is accommodated by the formation of oxygen vacancies and crystallographic shear (CS) planes. $Mo_{18}O_{52}$(100) and Mo_8O_{23}(010) contain CS planes which intersect the surface in two distinct ways. In $Mo_{18}O_{52}$, a component of the shear is normal to the (100) surface plane so that in addition to changing the coordination environment of the atoms on the CS plane, the shear introduces some surface relief. In Mo_8O_{23}, the shear lies entirely in the (010) surface plane and, therefore, the CS plane should introduce no surface relief. The final molybdate, η-Mo_4O_{11}, is distinguished from the other three molybdates because the (100) surface is terminated entirely by MoO_4 tetrahedra instead of MoO_6 octahedra. The structural chemistry of all of these molybdates was described in section 2.4.1.

4.2 SPM Observations

4.2.1 MoO_3(010)

α-MoO_3 is a layered solid and, as a result, fresh {010} surfaces are easily produced by cleavage with adhesive tape or a razor blade. The cleaved MoO_3(010) surface is characterized by large atomically flat terraces which are separated by steps. When steps are encountered, their edges are almost invariably oriented parallel to <001>

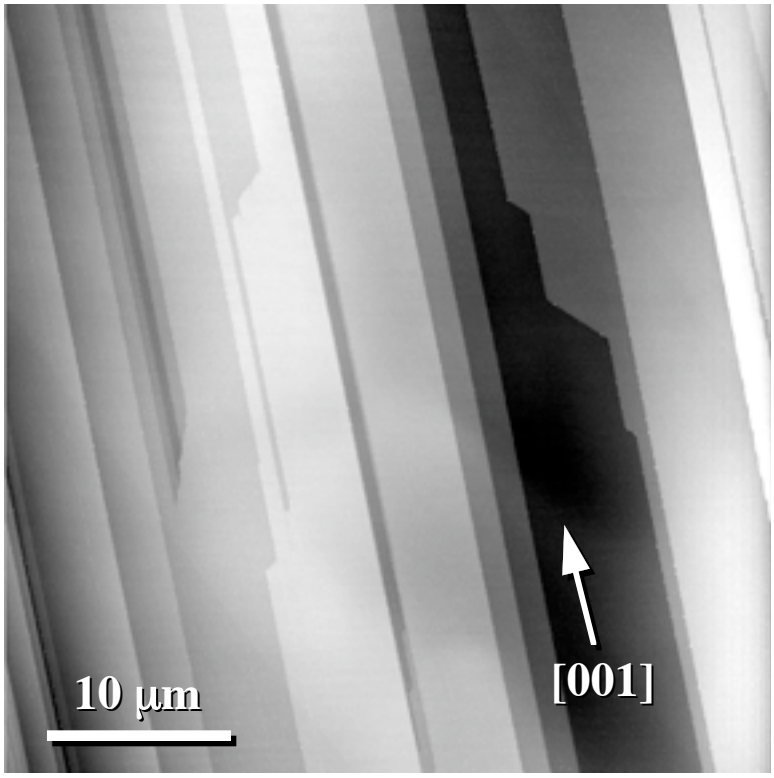

Figure 4.1 Topographic AFM image of a cleaved MoO_3(010) surface. Note the predominance of step edges oriented parallel to <001>. Surface steps are always an integer multiple of 7 Å (b/2) high and most of the steps in this region are only b/2 high. The black-to-white contrast in the image is 50 Å.

(see Fig. 4.1) and, in many cases, the flat terraces can extend more than 1 mm along this direction. The density of steps varies from region to region on the cleavage surface. In some areas, the terraces may be more than 100 μm wide along <100> while in other areas, they may be as narrow as a few microns. Steps oriented parallel to <001> can be formed by breaking bonds between Mo and doubly coordinate O at the shared corners of the octahedra along <001>. Step edges of other orientations are also encountered, but with a much lower frequency. Because the creation of steps of other orientations requires breaking more Mo-O bonds, the relatively higher population of <001> step edges is not surprising. Within experimental error (± 1 Å), the heights of the steps on this surface are always an integer multiple of the van der Waals gap that separates the adjacent double octahedral layers of the MoO_3 structure. The van der Waals gaps occur every 6.9 Å and this is the smallest step ever observed on the (010) surface. Therefore, MoO_3 cleaves at the weak van der Waals gap and two identical oxygen terminated surfaces are created.

Because only weak van der Waals bonds are broken during the formation of the (010) surface, it has a very low energy and significant atomic relaxation is not expected. Based on the bulk structure, one expects the (010) surface to be terminated by the layer of O atoms at the apices of the MoO_6 octahedral groups. The O atoms are more than 1.6 Å above the next layer of atoms and should be arranged to form a rectangular repeat unit, 3.96 Å x 3.70 Å. Atomic scale resolution AFM images can routinely be obtained on the

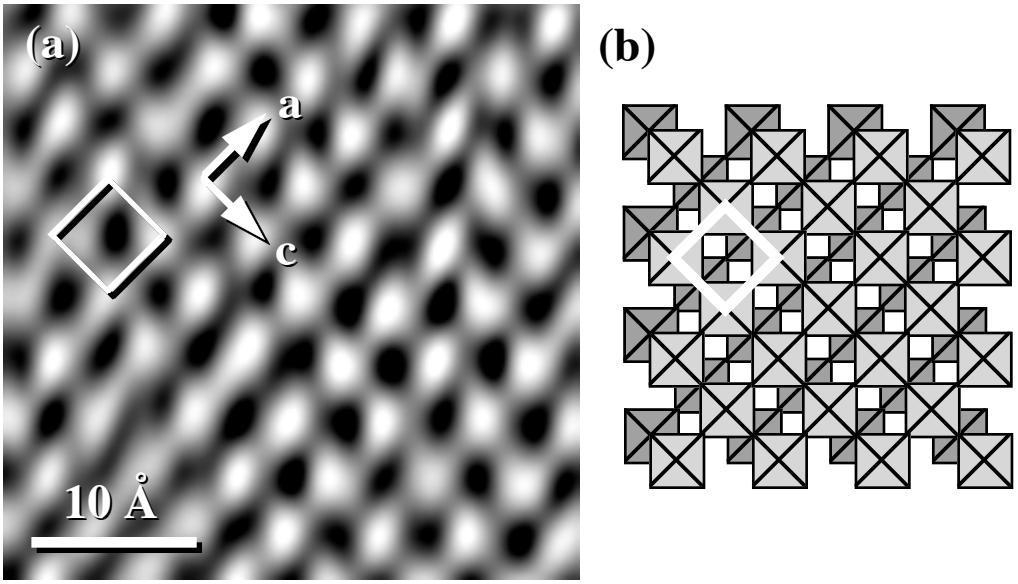

Figure 4.2 (a) Atomic scale resolution contact AFM image of the MoO_3(010) surface. (b) Polyhedral representation of the MoO_3(010) surface in approximately the same orientation as the AFM image. The surface repeat unit is indicated with a white box in each figure.

flat terraces of the (010) surface and their contrast (see Fig. 4.2) shows the expected, nearly square, repeat unit with dimensions of approximately 4 Å x 4 Å. This observation of a 1x1 repeat unit is consistent with previous LEED results [5,6] and earlier AFM observations of oxidized MoS_2 surfaces [7]. While the mechanism by which atomic scale contrast is formed in ambient AFM images is the subject of debate, there are numerous examples in which the features in atomic scale resolution AFM images can be correlated to the expected surface termination [8]. For the MoO_3(010) surface, there is a one-to-one correlation between the white contrast features in the image and the expected positions of the surface octahedra.

In addition to well developed basal facets, MoO_3 crystals grown by CVT often have optically smooth, lateral {hk0} facets. Contact AFM images of the as-grown facets revealed that these macroscopically 'smooth' surfaces were actually made up of many parallel steps with edges oriented parallel to <001>. Although the spacing and height of the steps are irregular, their orientation is fixed, as illustrated in the example shown in Fig. 4.3. The presence of these steps is interesting in light of the proposed mechanisms for the partial oxidation of hydrocarbons, such as propene, on MoO_3 catalysts; it has been proposed that propene activation takes place on the side {100} and {101} facets while oxygen insertion takes place on the {010} (basal) planes [9]. The microfaceted planes observed here place both types of sites in close proximity.

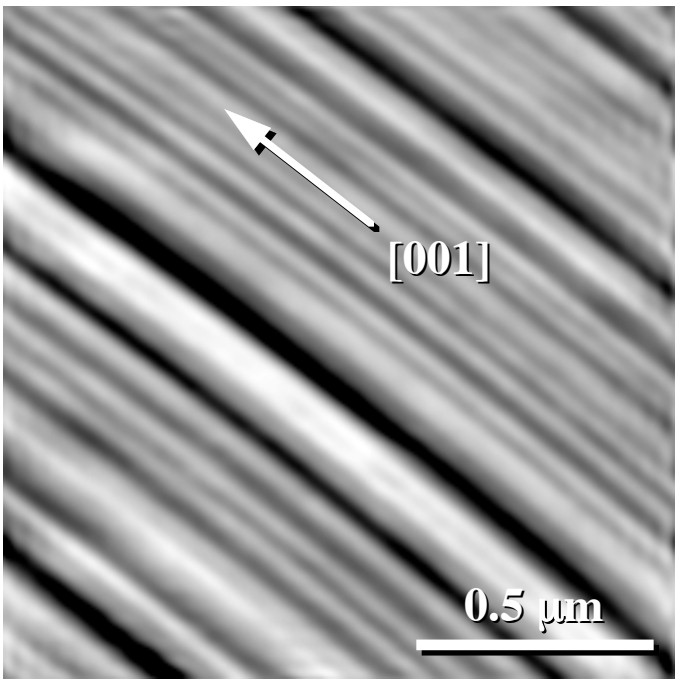

Figure 4.3 Contact AFM image of a MoO_3(hk0) growth facet. This facet can be indexed approximately to (570). The black-to-white contrast in this image is 200 Å.

4.2.2 $Mo_{18}O_{52}$(100)

Like MoO_3, $Mo_{18}O_{52}$ is a layered solid and the platy black crystals are easily cleaved with adhesive tape to produce {100} surfaces that are flat over many microns. When steps are encountered on this surface (cleaved or as grown) they are invariably oriented along the <010> axis of the crystal. This is the direction along which the crystallographic shear (CS) planes of the structure intersect the surface. As discussed in Section 2.4, the $Mo_{18}O_{52}$ structure is closely related to that of MoO_3. Both structures are composed of double octahedral layers that are linked by weak van der Waals bonds. Therefore, the cleaved (100) surface should be fully terminated by oxygen and consist of infinite slabs of an MoO_3(010)-type structure separated by ordered CS planes which run parallel to <010> [10]. Because cleavage occurs along weak van der Waals bonds, little surface relaxation is anticipated.

When the flat terraces are examined on a finer scale, the contrast in both STM (ambient and UHV) and AFM images of this surface is dominated by 1.5 Å high steps with edges oriented parallel to <010>. These small steps are spaced at regular intervals of approximately 20 Å and can be seen clearly in SPM images when scanning over areas as large as $(1000\ Å)^2$ (see Fig. 4.4). The spacing and orientation of the features allows us to assign this contrast to the positions where the CS planes intersect the (100) surface.

The CS plane contrast is similar in UHV STM, ambient STM and ambient AFM images recorded over hundreds of angstroms. However, distinct differences between the techniques become apparent when the surface is imaged near the atomic scale. High

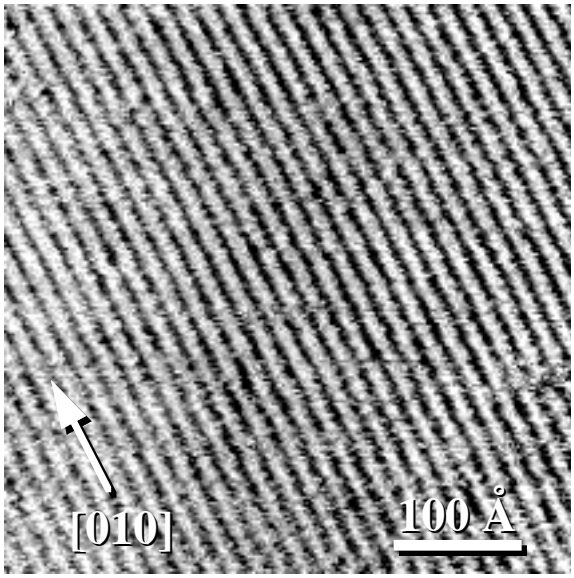

Figure 4.4 Ambient STM image of a cleaved $Mo_{18}O_{52}(100)$ surface showing CS plane resolution over a large scale. The CS planes are parallel to <010> and have a periodicity of 20 Å along <001>. Image is 460 Å x 460 Å.

resolution UHV STM images (see Fig. 4.5), recorded by tunneling from occupied states at biases near -1.65 V, clearly show contrast features in addition to the CS planes. The expected step at the CS plane is easily resolved and is indicated by the arrows in Fig. 4.5. Contrast within the areas separated by the CS planes can also be resolved. The rows of white contrast between the CS planes have a 3.8 Å period, just as the rows of MoO_6 octahedra in the MoO_3 slabs are expected to have. At the end of every third row, a brighter spot occurs along the CS planes and these bright spots have an 11.8 Å period along <010>. This is equivalent to the spacing between the MoO_4 tetrahedral units which define the vertices of the repeat unit on the (100) surface. Within experimental error, the observed surface repeat unit has the same dimensions as an (100) plane in the bulk structure, indicating that little or no surface reconstruction occurs.

The $Mo_{18}O_{52}(100)$ surface can routinely be imaged in the ambient with STM (see Fig. 4.6) by tunneling from occupied states at biases between -0.65 and -0.35 V. The contrast in these images shows the same terrace/shear step structure as those recorded in UHV (Fig. 4.5). Individual round, white contrast features are resolved within each terrace and there is a one-to-one correspondence between these features and the corner-sharing MoO_6 octahedra that make up the surface. However, the brighter contrast of the MoO_4 tetrahedral units, which is present in UHV images, is not repeated. This observation is characteristic of all images recorded on this surface in air. The discrepancy is not yet understood, but, could be the result of adsorbates or differences between the ambient and UHV imaging mechanism. Atomic scale resolution images of this surface were not attained with AFM. Although the CS planes were resolved over

areas as small as 200 Å x 200 Å (see Fig. 4.7), other contrast features were never observed.

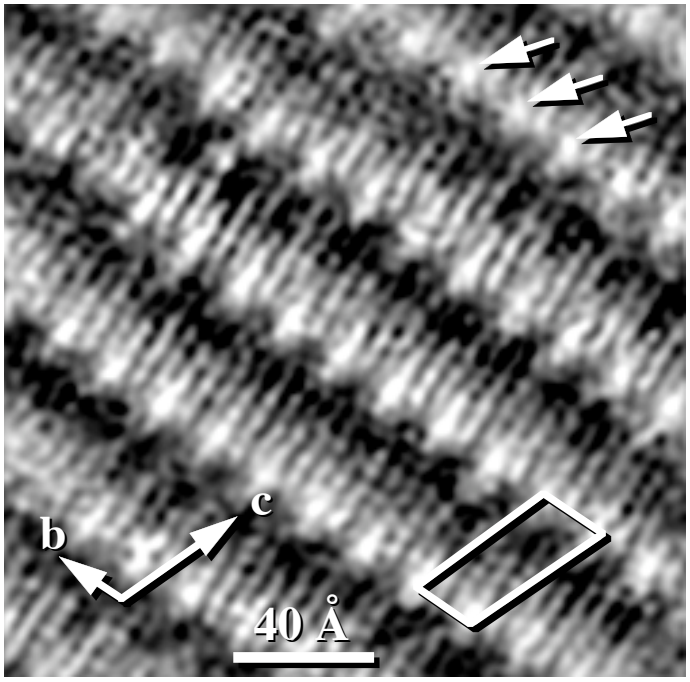

Figure 4.5 Atomic resolution UHV STM image of a cleaved $Mo_{18}O_{52}$(100) surface. The 1.5 Å step introduced where the CS planes intersect the surface is indicated by the arrows at the top of the figure. Each of these arrows also points to one of the bright contrast features which have been attributed to the MoO_4 tetrahedral units.

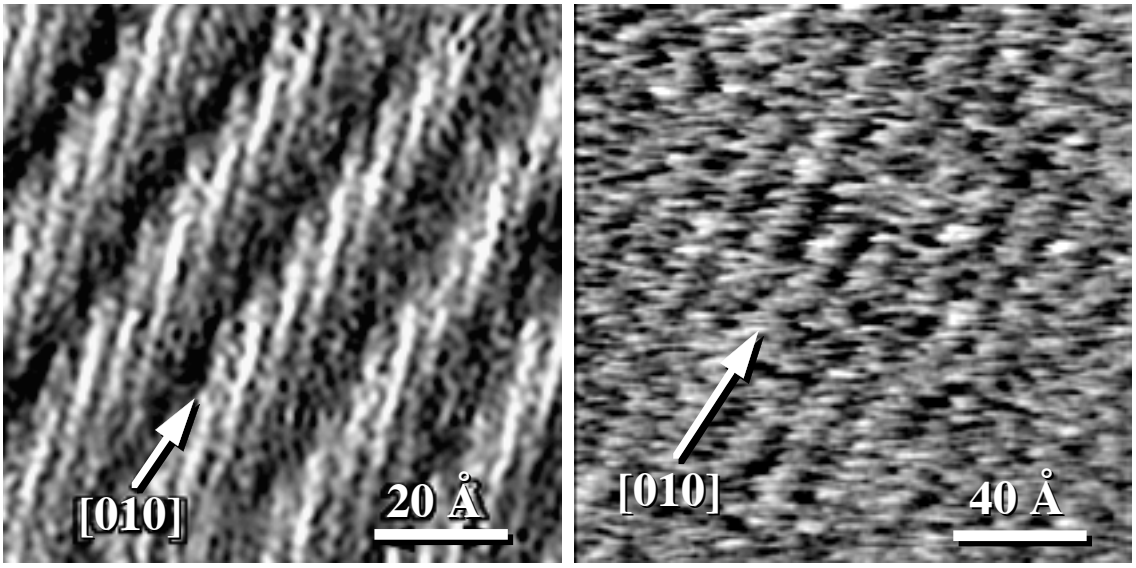

Figure 4.6 and 4.7 High resolution ambient STM (left) and AFM (right) images of $Mo_{18}O_{52}$(100) cleavage surfaces. The step at the CS plane/surface intersection is resolvable with both techniques. Additional contrast features, between the CS planes, have only been resolved with STM. While the rows of MoO_6 octahedra are easily resolved with STM in the ambient, the MoO_4 tetrahedra along the CS planes have never been resolved.

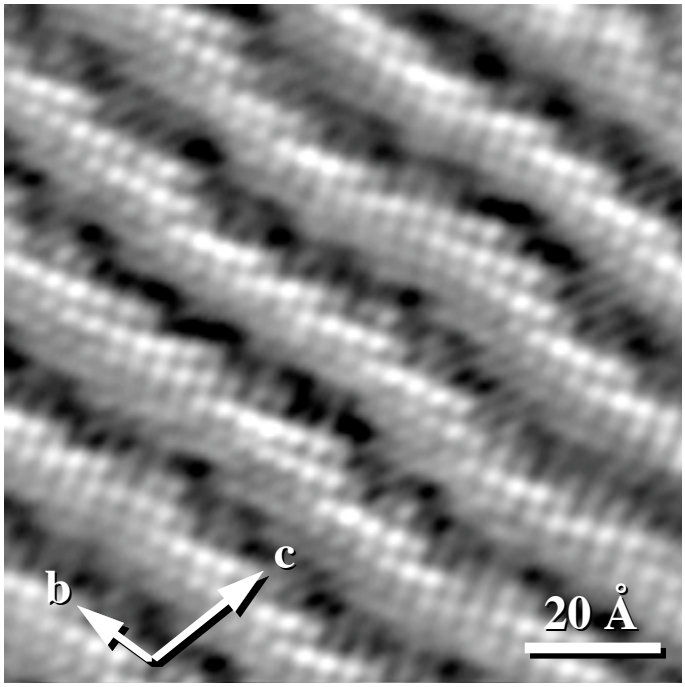

Figure 4.8 Ambient STM image of a cleaved $Li_xMo_{18}O_{52}(100)$ surface. The individual white spots in the image correspond to the MoO_6 octahedral units which terminate the surface.

4.2.3 $Li_xMo_{18}O_{52}(100)$

$Li_xMo_{18}O_{52}$ is essentially $Mo_{18}O_{52}$ with lithium intercalated into the van der Waals gaps which separate the adjacent layers of the structure. As a result, these crystals cleave easily with adhesive tape just like the parent $Mo_{18}O_{52}$ structure. Ambient STM images show contrast nearly identical to that of ambient STM images of the $Mo_{18}O_{52}(100)$ surface. The CS planes and octahedral units which terminate the surface are easily resolved, while the tetrahedral units along the CS planes are not. Images of the (100) surface of the Li intercalated structure, however, typically had a higher resolution than images of undoped $Mo_{18}O_{52}$. Comparison of ambient STM images of $Mo_{18}O_{52}(100)$ (see Fig. 4.6) and $Li_xMo_{18}O_{52}(100)$ (see Fig. 4.8) show that the individual MoO_6 octahedral units that terminate the surface are resolved more clearly on the surface of the doped crystals. This suggests that the electronic conductivity of nominally pure $Mo_{18}O_{52}$ is near the lower practical limit for atomic resolution imaging in air.

4.2.4 $Mo_8O_{23}(010)$

Mo_8O_{23} is a three dimensionally bonded oxide, however, {010} surfaces can be formed easily by cleavage parallel to {010} with a razor blade. Although the morphology of the surface depended on the direction of the cleave, {010} surfaces were characterized by large, micron-sized, flat areas. Most cleaves produced irregular, curved

steps that were rarely found on the more oxidized Mo-O surfaces studied. Cleavage parallel to <001>, however, resulted in the formation of many straight steps with edges oriented along <100>. For UHV measurements, single crystals were either cleaved in a N_2 filled glove bag, which was attached to a load-lock on the UHV chamber, or they were cleaved *in situ*. Atomic scale resolution STM images could be recorded in UHV or the ambient, however, the surface was etched during AFM experiments in air and all images showed the effect of this degradation. This etching phenomenon appears to be similar to that which Parkinson [11] observed in SPM studies of layered chalcogenides.

STM images of the Mo_8O_{23}(010) surface revealed two characteristic types of contrast which could be observed in different places on the same crystal and characteristic examples are shown in Fig. 4.9a and Fig. 4.9c. Both contrast types were observed while imaging in air, typically, while tunneling from filled states at -0.7 V. In UHV, tunneling into empty states at 1.3 V, however, only the contrast exhibited in Fig. 4.9a was observed. In both cases, the dimensions of the surface repeat unit are equivalent, within experimental error, to the dimensions of the (010) projection of the Mo_8O_{23} unit cell. However, the atomic scale features in the images are clearly different.

By considering the details of the bulk crystal structure of Mo_8O_{23}, it is possible to identify the most likely surface termination produced when a crystal is cleaved to expose {010} planes. Although the bonding in Mo_8O_{23} is nominally three dimensional, there is significant anisotropy in the axial Mo-O-Mo bonds that link the layers of MoO_6 octahedra along <010>. There are 16 such axial linkages per unit cell and in each one there is one very strong and short (1.69 Å) Mo-O bond and one longer, weaker (2.35 Å) contact. For comparison, the shorter of these two Mo-O bonds is similar in length to the bonds between Mo and the singly coordinate apical O atoms (1.67 Å) that terminate the basal plane layers in MoO_3. Assuming that the network of longer, weaker bonds is broken, cleavage produces two identical surfaces on which half of the surface polyhedra are MoO_6 octahedra capped by apical O atoms and the other half are inverted MoO_5 square pyramids that are not capped by apical O. This ideal termination pattern is illustrated in Fig. 4.9b where the polyhedra capped by O are white and those without the apical O are shaded.

Considering this termination model, the contrast in the image shown in 4.9a can then be understood by making a one-to-one correlation between half of the surface polyhedra in the model and the white contrast features on the STM image. In Fig. 4.9b, we see that both sets of surface polyhedra (for example, consider the white ones) form rows of six octahedra aligned along [201]. Each repeat unit (the oblique surface unit cell is indicated by the dark lines) contains three of the polyhedra from each of two adjacent

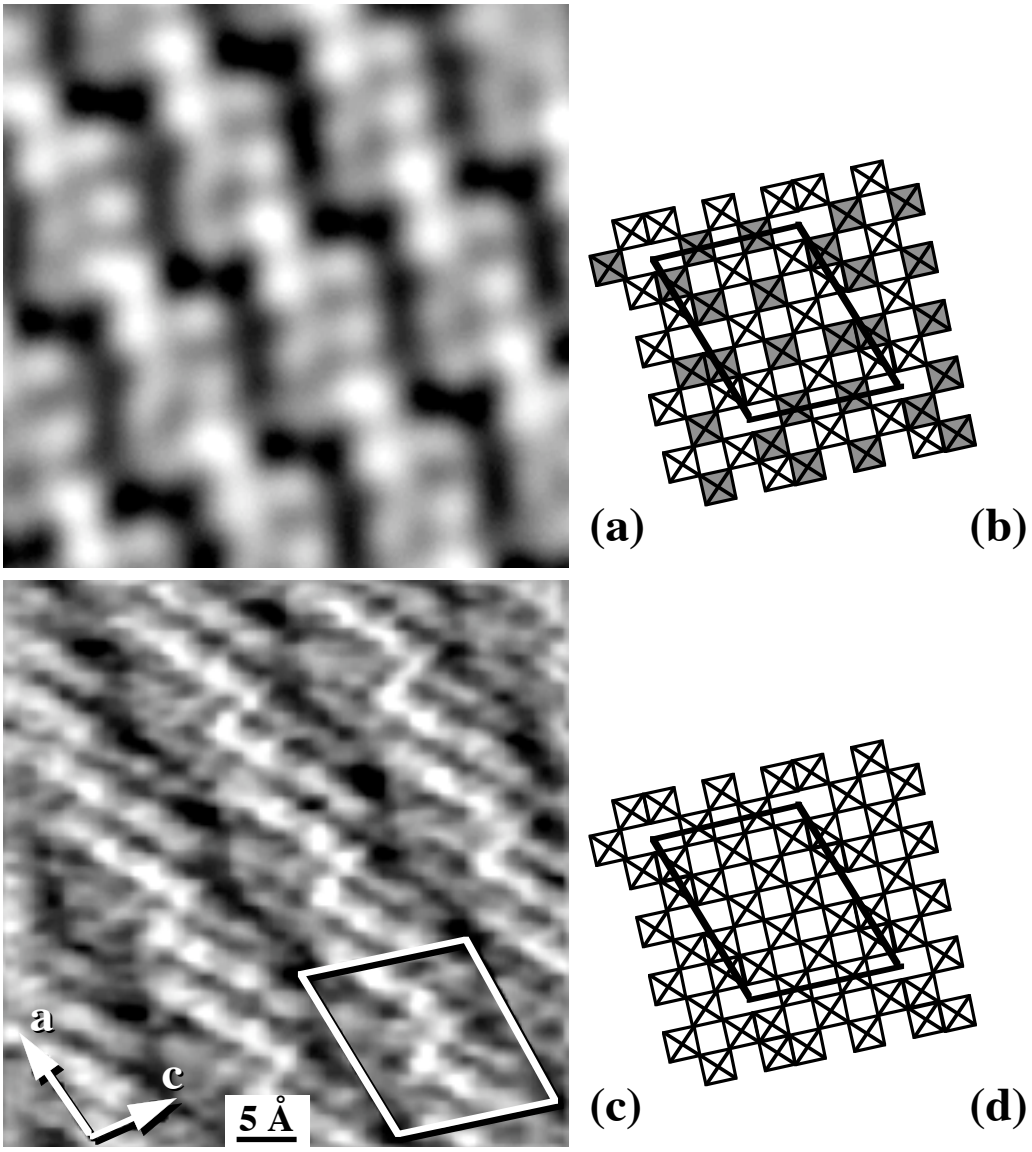

Figure 4.9 Constant current STM images showing the two characteristic contrast types observed on the $Mo_8O_{23}(010)$ surface, (a) and (b) and the corresponding termination models for each contrast type. Please see text for a complete description. The STM images are in the same orientation and on the same scale.

rows. One of the rows continues to the cell below and the other to the cell above. An identical pattern of features can be identified in the STM image in Fig. 4.9a. Using this correlation, the surface/CS plane intersections are the dark lines of contrast in the image. It is important to note that the assignment of the dark lines as the surface/CS plane intersections is not dependent on which subset of the polyhedra are imaged as white spots because the two subsets form the same pattern; it is important only that the two types of polyhedra are imaged differently.

The second type of contrast (see Fig. 4.9c) can be interpreted by assuming that all of the surface polyhedra are imaged, without distinguishing between those that are terminated by O and those that are not. Within each repeat unit there are rows of white contrast oriented along the $[10\bar{1}]$ direction. These contrast features have an orientation and spacing identical to the rows of corner-sharing octahedra that make up the structure. For comparison, Fig. 4.9d shows a model where all of the polyhedra are identical. Using these features as a guide, the surface/CS plane intersections can again be assigned to the dark lines of contrast oriented along the <100> axis of the crystal. Because this type of contrast can be observed under the same conditions as the other, we assume that there is a difference in the surface structure. Based on the uniformity with which the polyhedra are imaged, it is tempting to speculate that this surface has a uniform termination.

4.2.5 η-Mo_4O_{11}(100)

The η-Mo_4O_{11}(100) surface was imaged in air with STM. Like the other molybdate phases, cleavage, with a razor blade, revealed flat surfaces and high resolution STM images could be formed by tunneling from filled states in the bias range of -0.29 to -0.6 V. Two typical images are shown in Fig. 4.10. All of the images of this surface, recorded on multiple crystals with a variety of tips, have small regions that exhibit a regular, rectangular array of white contrast features which are separated by regions of diffuse contrast with no recognizable order. Like Mo_8O_{23}(010), Contact AFM imaging degraded this surface.

Although this is a three dimensionally bonded structure, we might anticipate that,

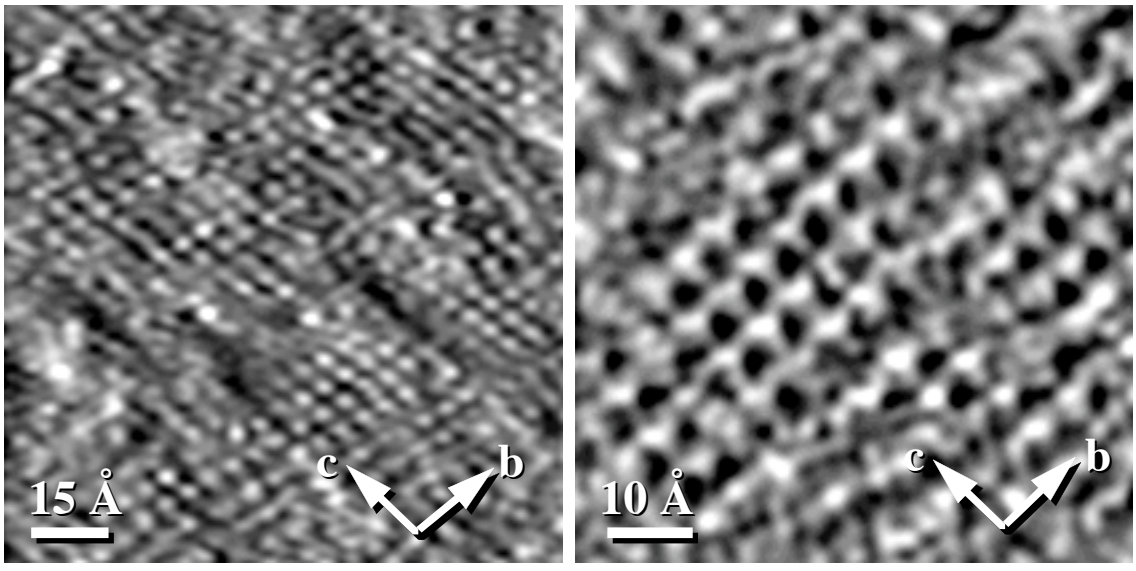

Figure 4.10 Ambient STM images of the η-Mo_4O_{11}(100) surface. Characteristically, small regions that exhibit an ordered rectangular array of white spots are separated by regions of diffuse contrast.

in the ideal case, a uniform termination layer can be exposed. We expect the cleaved (100) surface to be terminated at the planes which contain the MoO_4 tetrahedra. The bonds that must be broken to form this surface are axial linkages between a Mo atom at the center of an octahedron, an O at its apex, and a Mo atom at the center of a tetrahedron. The octahedral Mo-O bond is 2.11 Å and the tetrahedral Mo-O bond is 1.76 Å. Assuming that the longer and weaker of the two bonds is broken, the surface would be composed of a rectangular, 5.4 x 6.7 Å, pattern of tetrahedral groups that are terminated by an apical O. The pattern of contrast observed in the ordered regions of the images has the same periodicity and there is a one-to-one correlation between the white spots and the expected positions of tetrahedral groups. Thus, the contrast in these images can be interpreted in the same way as the contrast in the images of all the other molybdates. We assume that the diffuse contrast arises from defects in the termination layer, which might react with the surrounding environment.

4.3 Discussion

These observations of molybdenum oxide cleavage surfaces demonstrate that it is possible to use SPM to distinguish different types of surface/CS plane intersections in reduced Mo oxides. The MoO_3(010) surface is characterized by atomically flat terraces separated by steps that are integer multiples of 6.9 Å. When CS planes intersect the surface in such a way that a component of shear is normal to the surface plane, as is the case for $Mo_{18}O_{52}$(100), 1.5 Å shear steps are clearly observed in SPM images. These features are easily distinguished from the much larger steps between the adjacent layers of the structure. When CS planes intersect the surface in such a way that the shear lies entirely in the surface plane, as it does in Mo_8O_{23}(010), the line of intersection is a dark contrast feature in STM images. Because we used compounds in which the orientation and distribution of the shear planes is known from bulk crystallography, we can take these assignments to be unambiguous. Furthermore, based on these assignments, it should also be possible to identify surface/CS plane intersections on inhomogeneously reduced materials where the features might have a much larger and irregular spacing.

It is interesting to note that while the surface/CS plane intersections appear as dark lines of contrast in all STM images of Mo_8O_{23}(010), there is no obvious topographic signature in the ideal structure. There are, however, structural elements that do not appear elsewhere. Within each cell, two groups of four edge-sharing octahedra are separated from one another by rectangular channels bounded by six octahedra. While most of the details of the contrast in Fig. 4.9a can be correlated with the expected positions of the different types of surface polyhedra, both types of polyhedra are expected

at the surface/CS plane intersection and, therefore, the uniform dark appearance cannot be rationalized in the same way. If we instead assume that the contrast associated with these positions is due to an electronic rather than a topographic effect, we would conclude that the local conductance is lower at the positions where the shear planes intersect the surface. This is consistent with the observation that the highest bulk electronic resistivity in this material is measured when the current travels parallel to the CS planes [12].

While the surface/CS plane intersections in all SPM images of $Mo_{18}O_{52}(100)$ are distinguished by the 1.5 Å vertical rise and this alone is sufficient for identification, it is interesting to note that spatially resolved tunneling spectra of this surface indicate that there is also an electronic effect [3]. Specifically, the local conductance to the empty states at the surface/CS plane intersection is higher, in contrast to what was observed on the $Mo_8O_{23}(010)$ surface. Because bulk data for the anisotropy of the electronic conductivity are not available for $Mo_{18}O_{52}$, we are not able to compare our local observation to the properties of the bulk. It is noteworthy, however, that resistivity data for some shear compounds do show enhanced conductivity when the current travels parallel to the CS planes [13].

The anisotropy of the bonding in the four molybdates described here leads to the creation of stable cleavage surfaces that can be imaged in air and vacuum. The success of interpreting the observations simply by correlating the expected positions of surface polyhedra with the image contrast is somewhat surprising and raises some interesting questions. First, what are the differences between STM images recorded in UHV and those recorded in air? Ideally, we would like to be able to specify the surface structure as a function of the surrounding environment. However, the differences that we see in air and vacuum might be a reflection of the experimental conditions and active imaging mechanism rather than the surface structure. For example, when tunneling in air, we assume that the adsorbed layer of water that must be on the surface acts as a dielectric in the tunnel gap and modifies (increases) the tunneling probability.

There are two clear differences between our vacuum and air observations. First, on the $Mo_{18}O_{52}(100)$ surface, contrast features corresponding to the tetrahedral groups were reproducibly observed only in vacuum. Second, the type of contrast exhibited in Fig. 4.9c (STM images of the $Mo_8O_{23}(010)$ surface) was observed only in air. Unfortunately, it is not possible to attribute these differences solely to structural changes caused by the environment. In all of the cases described here, the absolute value of the bias used to record high resolution images in air is less than what is used in vacuum and all of the ambient images were formed by tunneling from filled states. These are

potentially important considerations since images recorded at different biases sample different energy levels and this can potentially cause contrast differences. We can, however, make the statement that all images presented here were recorded while probing conduction band states formed by the overlap of Mo and O orbitals. Because the Fermi level is pinned near the bottom of the conduction band, and this band is separated from the filled valence band by a gap of several volts, we do not probe the filled states even when the sample is negatively biased. We either tunnel to empty states above the Fermi level or remove electrons from filled states in the same band. However, differences might still arise because the relative contribution of the O orbitals to the density of states in the conduction band changes as a function of bias.

The systematic SPM imaging of similar phases with well characterized structural differences is an effective way to develop contrast assignments. This has made it possible to identify contrast signatures of two different types of surface/CS plane intersection: those with and without a component of shear normal to the surface of intersection. Additionally, the details of atomic-scale contrast in these anisotropically bonded oxides could be interpreted by assuming a surface structure formed by cleavage of the longest, weakest bonds normal to the surface.

A similar systematic SPM study has been performed on two vanadate surfaces, $V_2O_5(001)$ and $V_6O_{13}(001)$ and the results are described and discussed in the archival literature [2,4]. This work has not been presented here because it is not relevant to the specific objectives of this thesis. However, the results of this study showed that simple broken bond models could also be used to interpret the contrast in AFM images of anisotropically bonded vanadates. Furthermore, with image simulations, two limiting STM contrast types were identified for the case of probing the conduction band states of surfaces that are terminated by metal-oxygen octahedra (MO_6) in axial alignment. When the surface octahedra are terminated by apical O and these O are more than 1 Å closer to the tip than the closest metal (M) atom, the O appear as white contrast in STM images. When the surface is terminated by M and O, at approximately the same level, it is the M atoms that appear as white contrast in STM images [4].

4.4 Summary and Conclusions

Study of these molybdate surfaces has demonstrated that the atomic scale contrast in SPM images of anisotropically bonded oxides can often be interpreted based on a simple model that assumes cleavage occurs at the longest, weakest bonds normal to the surface. The SPM contrast signatures of two types of surface/CS plane intersections in molybdenum suboxides have been identified. When the CS planes have a component of

shear normal to the surface, as in $Mo_{18}O_{52}$(100), the CS planes are marked by a step at the interface. When the CS planes intersect the surface such that the shear lies entirely in the surface plane, as in Mo_8O_{23}(010), the line of intersection is marked by dark contrast in STM images.

4.5 References

[1.] G.S. Rohrer, W. Lu, R.L. Smith, and A. Hutchinson, *Surf. Sci.* **292** (1993) 261.

[2.] R.L. Smith, W. Lu, and G.S. Rohrer, *Surf. Sci.* **322** (1995) 293.

[3.] R.L. Smith and G.S. Rohrer, *J. Solid State Chem.* **124** (1996) 104.

[4.] R.L. Smith, G.S. Rohrer, K.S. Lee, D.-K. Seo and M.-H. Whangbo, *Surf. Sci.* **367** (1996) 87.

[5.] L.E. Firment and A. Ferretti, *Surf. Sci.* **129** (1983) 155.

[6.] L.C. Dufour, O. Bertrand, N. Floquet, *Surf. Sci.* **147** (1984) 396.

[7.] Y. Kim and C.M. Lieber, *Science* **257** (1992) 375.

[8.] S.N. Magonov and M.H. Whangbo, *Adv. Mater.* **6** (1994) 335.

[9.] K. Bruckman, R. Grabowski, J. Haber, A. Mazurkiewicz, J. Sloczynski, and T. Wiltkowski, *J. Catal.* **104** (1987) 71.

[10.] L. Kihlborg, *Arkiv Kemi* **21** (1963) 471.

[11.] B. Parkinson, *J. Am. Chem. Soc.* **112** (1990) 7498.

[12.] M. Greenblatt, *Chem. Rev.* **88** (1988) 31.

5

Evolution of the MoO_3(010) Surface during the Reduction and Oxidation (Redox) Cycle

5.1 Introduction

Partial oxidation reactions on MoO_3 are generally thought to conform to the Mars - van Krevelen redox mechanism. If this is the case, oxygen stoichiometry compensating defects are continuously created and annihilated during the redox process. The objective of the experiments described in this chapter was to use AFM to determine how the MoO_3(010) surface evolves during the redox cycle. In the first section, the evolution of the surface during reduction between 200 and 400 ˚C is described [1]. Reduction was accomplished by reacting cleavage surfaces with 10%H_2-N_2, CO, and N_2 containing known quantities of water vapor. The structural evolution during reoxidation was examined by treating virgin and H_2-reduced surfaces at 400 ˚C in static air at ambient humidity [2].

5.2 Structural Evolution of MoO_3(010) during Reduction

Cleaved, mounted single crystals of MoO_3 were treated at 1 atm in continuous flows of forming gas (10%H_2-N_2), N_2, and CO. Flow rates between 350 and 50 cc/min were used and, in general, the choice of flow rate did not appear to affect the surface structural evolution. In most cases, the single crystal samples were reacted in as-received forming gas which had a nominal water impurity concentration of 20 ppm. Additional experiments were conducted to explore the effect of water vapor in the reactor. First, a subset of samples were treated in forming gas that was dried by passing it through a column of $CaSO_4$. To separate the effect of water present as an impurity phase and water formed as a reaction product, crystals were also treated in N_2 and CO streams of known water content. It is important, however, to recognize that changing pH_2O will necessarily lead to a change in the equilibrium pO_2. Most of the AFM images presented here were acquired in the ambient and, therefore, the surface had been exposed to air after reduction. Control experiments demonstrated that this exposure did not alter the

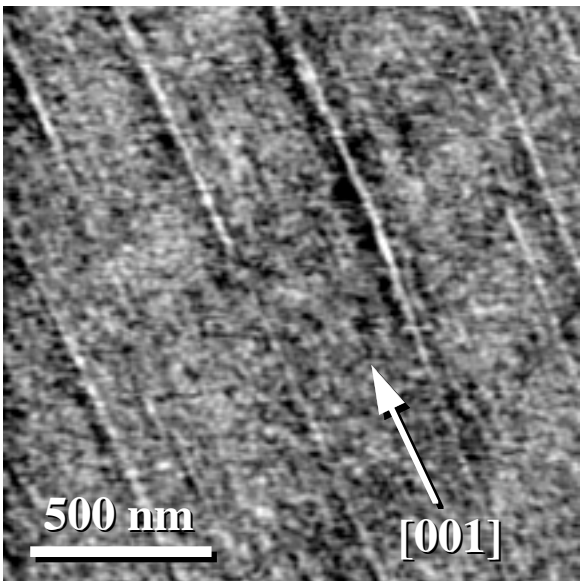

Figure 5.1 Contact AFM image of a cleaved MoO_3(010) surface which was reacted with forming gas for 1 min at 400 ˚C. The small surface steps, streaky, white contrast parallel to <001>, have heights of approximately 2 Å and lengths of up to 5 μm. The black-to-white contrast in this image is 5 Å.

microstructure that one observes with AFM. In these control experiments, the samples were reacted and then transferred directly, with out exposure to air, to a glove box for AFM analysis.

5.2.1 Results

Reduction at Low Temperatures (T < 350 ˚C). MoO_3(010) surfaces reacted at temperatures less than 350 ˚C for as long as six hours in 10%H_2-N_2, CO, and N_2 (with humidities ranging from nominally dry to saturated with H_2O) could not be distinguished from the fresh cleaved surface with AFM. The only noticeable change in crystals reacted for extended periods of time was a slight color change. For example, after reactions in excess of 6 h at 300 ˚C, the crystals' color changed from transparent green-yellow to transparent blue-green indicating that the samples were oxygen deficient MoO_{3-x}. X-ray diffraction (XRD) experiments demonstrated that powdered samples were phase pure MoO_3 after reactions in excess of 6 h at 250 ˚C in 10%H_2-N_2 (regardless of humidity).

Reduction at High Temperatures (T ≥ 350 ˚C) In contrast to the low temperature reactions, the MoO_3(010) surface was modified during reduction reactions at temperatures greater than 350 ˚C and reduction in as-received forming gas led to two distinct changes in the (010) surface. First, small steps oriented parallel to <001> form on the surface within the first minute of reduction. The steps have an irregular spacing and, as shown in Fig. 5.1, appear as a straight, streaky contrast along <001>. The height of these steps, approximately 2 Å, is far smaller than any step ever observed on the

untreated surface. The second change is the formation of pits on the, previously, flat {010} terraces of the surface. Pits with widths on the order of 1000 Å and depths of 50 Å were observed within the first minute of reduction at 400 ˚C and some examples of these pits are shown in Fig. 5.2.

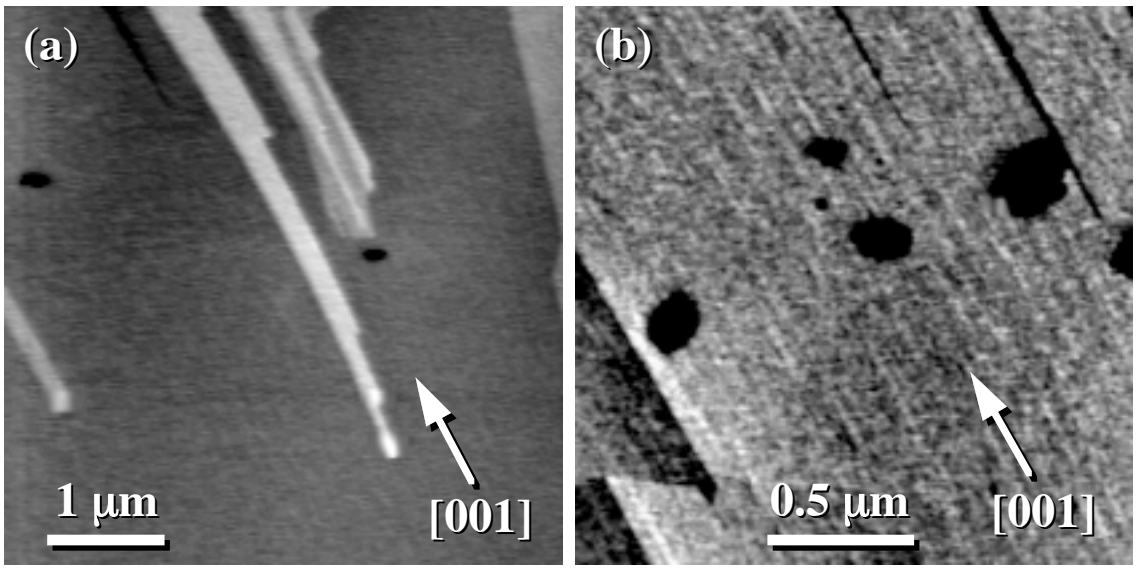

Figure 5.2 Contact AFM images of the pits which form on the MoO_3(010) surface during reactions with 10%H_2-N_2 (with 20 ppm H_2O). The surface in (a) was reacted for 30s at 400 ˚C and that in (b) for 2 min at 400 ˚C. The black-to-white contrast in the images is 40 Å (a) and 20 Å (b).

Figure 5.3 Contact AFM image of an MoO_3(010) surface which was reacted with 10%H_2-N_2 (20 ppm H_20) at 400 ˚C for 5 min. Both the average size and total number of pits increase with increasing reaction time. The black-to-white contrast in the image is 50 Å.

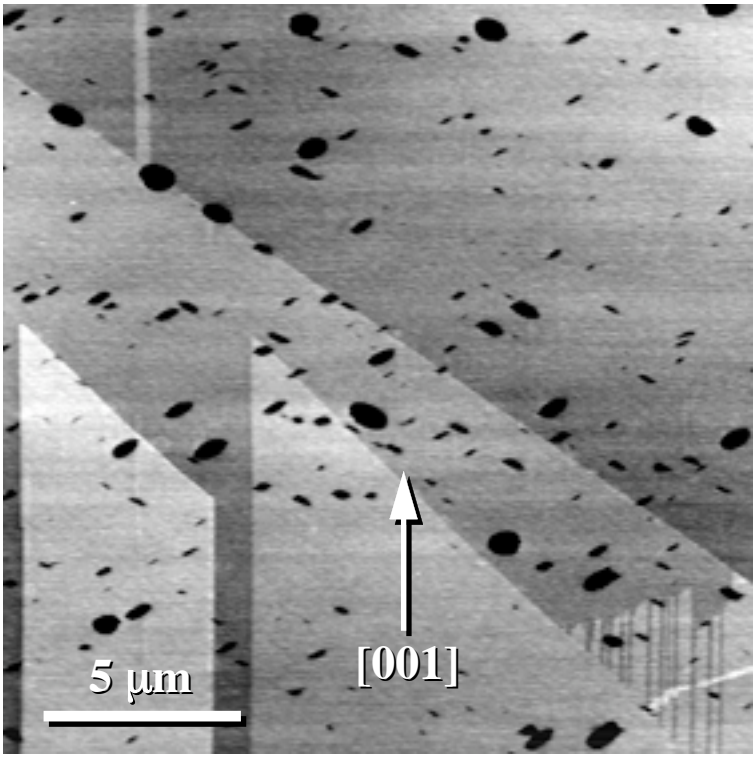

Surfaces reacted for longer periods of time showed similar features. However, as the reaction time was increased the density of the small surface steps and the number and average size of the pits increased (see Fig. 5.3). Within the first five minutes of reaction, pits as large as 1 μm in diameter and 200 Å in depth were observed. With longer reaction times, the density and size of the pits continue to increase and eventually the edges of adjacent pits begin to intersect. By surveying multiple areas on multiple crystals, it was determined that the pits nucleate with equal probability on both the {010} terraces and the step edge sites. The pits do, however, appear to be associated with the small surface steps. The edges of each pit almost always intersect a number of the small surface steps and, in many cases, the pits interrupt what would otherwise be a continuous 2 Å step. The coincidence of the pits and surface steps can be seen in the AFM images in Fig 5.4.

While the pits are not completely faceted, many of their bounding edges are preferentially oriented approximately along the <101> axis of the crystal. This can be seen in the AFM topograph in Fig. 5.5. The edges, however, are not exactly aligned with this low index direction; their orientation axis typically intersects <001> at angles of 51° and 35° rather than the 43° that one would expect for <101>. For all but the longest reaction times, the crystals were visually unaffected by the reducing treatments. Only after reactions in excess of 10 min did crystals begin to take on the blue-gray color that is characteristic of substoichiometric MoO_{3-x}. Finally, crystals that were treated at higher

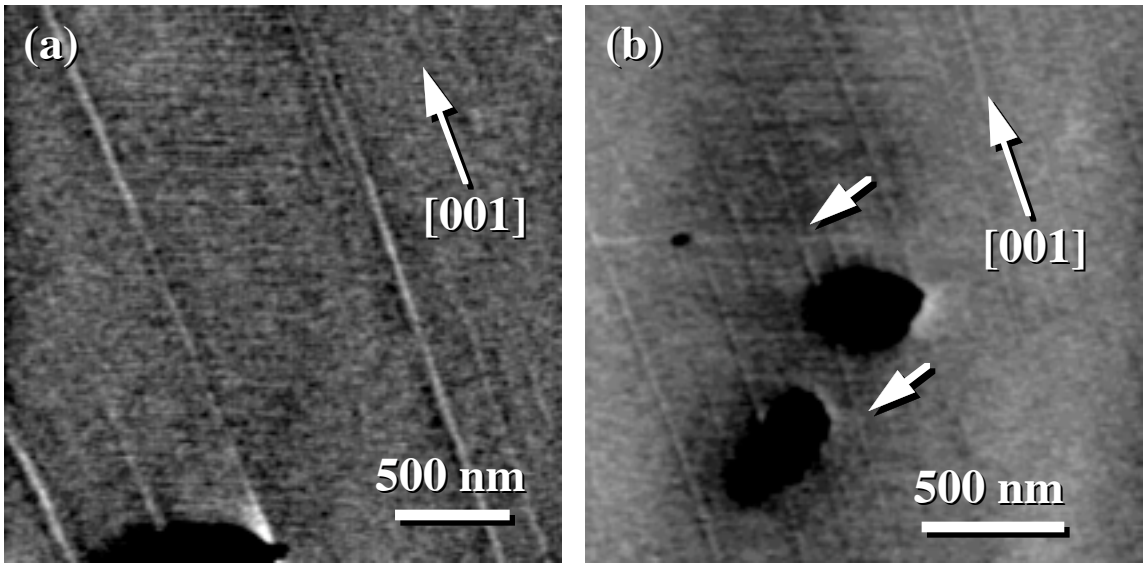

Figure 5.4 Contact AFM images showing the intersection of pit boundaries with the small surface steps during the reduction of MoO_3(010) in forming gas at 400° C. In (b), the pits appear to interrupt continuous 2 Å surface steps. One interrupted step is indicated with arrows in the figure.

temperatures, for example 500 ˚C, showed similar morphological changes. At higher temperatures, however, the defects grew at an accelerated pace.

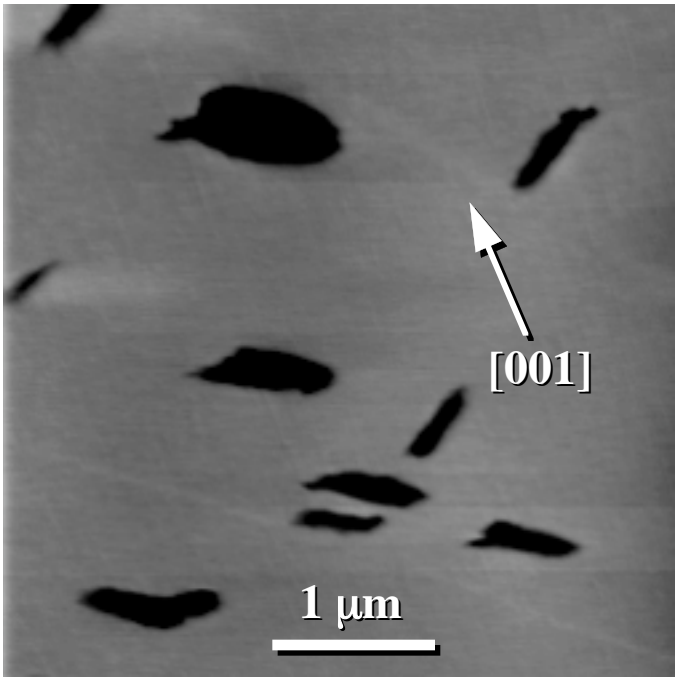

Figure 5.5 Contact AFM image of a MoO_3(010) surface after reaction with 10%H_2-N_2 (20 ppm H_2O) at 400 ˚C for 5 min. Note the high aspect ratio of the pits and their bounding edges. The black-to-white contrast in the image is 50 Å.

The Effect of Water Vapor on Pit Formation. While the surface evolution described in the previous section was characteristic of all samples reacted in as-received forming gas above 350 ˚C, crystals treated in dried mixtures had fewer and smaller pits than those heated in undried mixtures for equivalent periods of time. To separate the effect of water vapor produced by the reaction of H_2 with the crystal and water present as an impurity in the gas phase, a subset of crystals was treated in streams of flowing N_2 which had known amounts of H_2O. Surfaces treated in dry N_2 showed no signs of pitting after treatments in excess of 5 min at 400 ˚C. The presence of just 20 ppm H_2O in the N_2 stream, however, resulted in the formation of pits similar to those found on the samples treated in forming gas (see Fig. 5.6a). Crystals which were treated in N_2 that had been saturated with H_2O apparently pitted at an accelerated pace. Within 5 min at 400 ˚C, a severely stepped, cellular structure developed on the surface as can be seen in the AFM topograph in Fig. 5.6b. Again, the step edges are preferentially oriented (like the pits) nearly parallel to <101> directions. Step edges with this orientation (and with such a high density) have never been observed on the fresh cleaved (010) surface. Finally, a similar dependence of pitting on water content was observed when reduction was carried out in CO streams with different humidities.

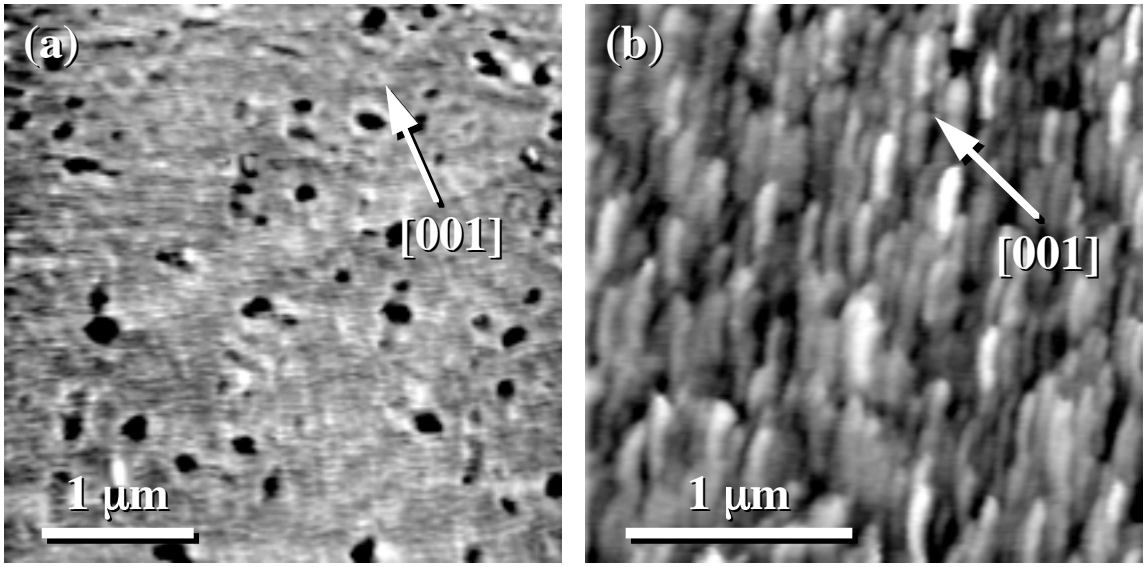

Figure 5.6 Contact AFM images illustrating the effect of water vapor on pit formation at 400 ˚C. The MoO_3(010) surface in (a) was treated for 5 min in flowing N_2 with ~ 20 ppm H_2O while that in (b) was treated for 5 min in N_2 that was saturated with H_2O at 25 ˚C. The black-to-white contrast in (a) is 60 Å while that in (b) is 200 Å.

5.2.2 Discussion

MoO_3 is one of a number of transition metal oxides that accommodate oxygen deficiency by forming both oxygen vacancies and crystallographic shear (CS) planes [3-7]. When the shear vector of a CS plane has a component that is normal to the surface plane, a small step must be created along the CS plane/surface intersection. TEM studies have shown that when MoO_3 is reduced above 350 ˚C, CS planes form along <001> and the shear can be described by <**a**/2 **b**/7 0> $\{1\bar{2}0\}$ [3,6]. Therefore, the 2 Å (~b/7) steps observed on the reduced MoO_3(010) surface are easily explained as the intersection of CS planes with the surface. This shear vector is parallel to the edge of an MoO_6 octahedron in the structure and is common to a number of the so-called "CS phases" in the binary Mo-O system [4,7]. $Mo_{18}O_{52}$ is one such phase and STM and AFM studies of the (100) surface of this compound have verified the existence of a small step at the CS plane/surface intersection (section 4.1.2) [8].

The series of N_2 treatments clearly showed that water vapor is necessary for pit formation at 400 ˚C. If the gas is dried prior to reaction and no water vapor is formed during the treatment, then pits do not form on the (010) surface, even after treatments in excess of 5 min. The simplest explanation for pit formation and growth is that the MoO_3(010) surface is volatilizing during the reduction reaction. The observation that water vapor accelerates this sublimation process is not so surprising. It is well known that H_2O can be used as a mineralization agent in the chemical vapor transport synthesis

of oxide single crystals [9]. Furthermore, H_2O is known to enhance the volatility of Mo, W, and their respective trioxides [10,11]. During these reactions, sublimation is enhanced by the formation of gaseous hydroxides or oxide-hydroxides. The pitting mechanism observed here most likely involves the formation and evaporation of volatile molybdenum oxide-hydroxide species (such as $MoO_2(OH)_2$) at the interface [11]. The volatilization and depletion of MoO_3 from Fe-Mo-O and Bi-Mo-O catalysts above 430 ˚C is well documented and it is likely that water vapor is also responsible for this process [12,13].

It is not clear that preferential sites for pit nucleation exist at the interface. While no heterogeneity has been identified on the fresh cleavage surface and the pits appear to be distributed randomly, nucleation sites could form at lower temperatures, as the crystal is being heated to the reaction temperature. AFM analysis of {010} surfaces reacted with molecular hydrogen at temperatures less than 350 ˚C, however, reveal no modifications. Therefore, the only possible pre-existing nucleation sites would be oxygen vacancies or some other surface feature which cannot be detected with AFM. The pits always intersect CS planes at the surface and, in many cases, they interrupt what would, otherwise, be continuous CS planes, as in Fig. 5.4. This indicates that the CS planes form prior to the pits and that pit nucleation might be linked to the CS process. One plausible explanation is that pit nucleation is enhance by the elastic strain in the vicinity of the shear planes.

The observation that the (010) surface is not modified during reduction at low temperatures (T < 300 ˚C) conflicts with previous TEM observations [3-6]. In these previous studies, "domains" were reported to form at low temperatures (~ 200 ˚C) and grow with increasing time or temperature (up to 350 ˚C). There are two possible explanations for our failure to observe the domains with AFM. The first is that the features give rise to no surface perturbation and, therefore, go undetected. The second possibility is that they do not form under the experimental conditions described here. This possibility is strongly supported by our powder XRD studies; secondary phases were not detected in samples reacted in 10%H_2-N_2 for as long as 6 h at 250 ˚C. The discrepancies between these experiments and previous TEM studies will be resolved in the next chapter.

5.2.3 The Effect of pO_2 on CS Plane and Surface Pit Formation.

While the microstructural changes described in the previous sections are characteristic of MoO_3(010) surfaces reduced in the presence of H_2O, the homogeneity and speed of defect formation is dependent on the partial pressure of oxygen in the

reactor. When samples were mounted with Ta, pits and CS planes appeared to form homogeneously across the (010) surface. If however, the samples were reacted in the absence of Ta, reduction proceeded inhomogeneously. For example, after 5 min of reduction at 400 ˚C, very few CS planes or pits could be found in the center of single crystals. Very near (within 200 μm) the edges of the crystals, however, the population of CS planes and surface pits was substantially higher and comparable to that found on crystals mounted with Ta. From the edge inward, there is a negative gradient in the size and density of the defects. If a small piece of Ta foil was placed in the boat with the crystals, the surface structural evolution was identical to that observed on the mounted single crystal samples. Thus, when Ta is present in the reactor, CS planes and pits form more rapidly and appear to be distributed more homogeneously across the (010) surface. Tantalum's influence could also be observed with the naked eye; surfaces reacted in the presence of Ta were more deeply colored than their counterparts which were reacted in the absence of Ta.

CS planes form as a direct result of reduction and oxygen loss. In the presence of Ta, CS plane formation is accelerated and, therefore, reduction must be occurring faster. In light of tantalum's well-known ability to scavenge oxygen, this is certainly not a surprising result. Consider the free energies of formation of Ta_2O_5 (s) and H_2O (g) from their constituent elements at 400˚ C [14]:

$$2Ta + 5/2\ O_2 = Ta_2O_5 \quad \Delta G_f = -\ 1750\ kJ/mol$$
$$H_2 + 1/2\ O_2 = H_2O \quad \Delta G_f = -\ 209.2\ kJ/mol$$

Recalling that $\Delta G_f = -\ RT \ln K$ ($R = 8.314$ J/mol) and, therefore, $K = \exp(-\Delta G_f/RT)$, we arrive at the following equilibrium expressions for the partial pressure of oxygen at 400˚C (assuming that the activities of Ta and Ta_2O_5 are unity):

$$Ta\text{-}Ta_2O_5 \quad (pO_2)^{(5/2)} = \exp(-1750/RT)$$
$$(pO_2) = 2.545 \times 10^{-52}\ atm$$

$$H\text{-}H_2O \quad (pO_2)^{(1/2)} = (pH_2O/pH_2)\exp(-209/RT)$$
$$(pO_2) = (pH_2O/pH_2)^2 * 5.7 \times 10^{-17}\ atm$$

In the as-received forming gas mixture, the ratio of pH_2O to pH_2 is approximately 2×10^{-4}. If we assume that equilibrium is established, $pO_2 = 2.28 \times 10^{-24}$ atm. Therefore, there

is a significant difference (28 orders of magnitude) between the equilibrium partial pressure of oxygen established by Ta/Ta_2O_5 and that established by H_2/H_2O.

The real situation in the reactor is more complex. First of all, both equilibrium equations must be considered simultaneously to arrive at the equilibrium partial pressures. However, we are in no way certain that equilibrium has been established and, in all likelihood, it has not. For example, if equilibrium were to be established, essentially all of the available water vapor would also be scavenged by the Ta (as would the O in MoO_3). The strong variation in pitting with the initial water content indicates that this is not the case and, therefore, O_2 may be scavenged more efficiently than water. Because it is impossible to independently vary the partial pressures of oxygen and water at a given temperature, it is also impossible to systematically characterize the dependence of pitting on these two parameters. However, the available data indicate that both reduction and water vapor are necessary for pitting. If water vapor is completely excluded (i.e. dry N_2), reduction (CS plane formation) still occurs, but pits do not form. If any water is present and reduction occurs, then pits also form. Furthermore, the pit density appears to scale with the CS plane density.

One remaining question is why the surface reduces faster near the edges? In the initial low pO_2 (with Ta) experiments this effect may have been overlooked because reduction occurred so quickly everywhere. With a higher pO_2, however, the effect was much more noticeable. One must ask, therefore, whether reduction kinetics are controlled by the adsorption of and reaction with H_2 or purely by the partial pressure of oxygen or do both operate to different extents depending on the gas phase? If H_2 adsorption requires coordinatively unsaturated surface sites, we might expect the process to proceed more swiftly at the edges because these types of sites are thought to be localized here [12]. If it is the $pO2$, then these results indicate that oxygen leaves the crystal most efficiently near the edges. This may be because O_2 diffusion is faster between the layers of the crystal or simply because at the edges we have two exposed surfaces which can simultaneously give up oxygen to the atmosphere.

5.2.4 Implications of CS Planes and Pits on the Catalytic Process

The formation of CS planes at the MoO_3(010) surface alters the oxide in a number of ways and these changes can potentially influence the oxide's catalytic properties. For example, new atomic coordination environments occur where the MoO_6 octahedra share edges at the CS plane/surface intersection [4,7,15]. CS planes form only after the surface is saturated with oxygen vacancies and, therefore, they effectively fix the oxygen vacancy concentration at the surface. CS planes grow into the bulk by the climb

of their bounding partial dislocations and, therefore, they consume oxygen vacancies and sites as they extend into the interior of the crystal. The presence of CS planes in our samples indicates that at 400 °C in the presence of H_2 the equilibrium concentration of surface vacancies has already reached its upper limit. In previous TEM studies, vacancy saturation and CS plane formation were also observed at ~400°C [3-6]. If we assume that oxygen vacancies are preferred reaction sites, then CS plane formation will limit the catalyst's activity by establishing an upper limit on the oxygen vacancy concentration. If, on the other hand, CS planes enhance partial oxidation processes, as suggested by Broclawik and Haber [15], then the reverse might be true for reactions which occur above ~350 °C. Finally, it is important to realize that CS planes alter both the mass and charge transport properties of the oxide. For example, O'Keeffe [16] has pointed out that CS planes might provide high diffusivity pathways for oxygen ions in the solid. Furthermore, it is known that as the oxygen deficiency and CS plane density increases, the electronic conductivity of the oxide also increases [17].

Because some water is always present in a catalytic reactor, at least as a deep oxidation product, and these reactors are often operated under reducing conditions, the surface pitting process may occur over a wide variety of reaction conditions. The morphological changes associated with this process probably influence the properties of MoO_3 catalysts. Studies on the reactivity of highly-oriented, powdered MoO_3 catalysts indicate that the {010} (basal) facets favor the deep oxidation of feedstocks such as methane [18] and 1-butene [19] while the lateral facets, the {100} and {h0l} surfaces, show a high selectivity to partial oxidation products. Furthermore, studies of the conversion of propene to acrolein indicate that this oxidation reaction proceeds via a two step process that requires sites on both the lateral and basal planes to be in close proximity [20]. If we accept these mechanisms, our results indicate that the pits which form on the basal facets, after exposure to water vapor, will enhance the ability of MoO_3 to catalyze these partial oxidation reactions. Pitting increases the number of {h0l} sites and brings more basal plane sites and lateral sites into close proximity. It is interesting to note that while the initial powder morphology of the catalyst may favor deep oxidation products (i.e. highly oriented to {010}), one of these products (H_2O) will cause the catalyst to evolve toward a morphology with greater selectivity to partial oxidation products.

5.3 Oxidation of Cleaved and Reduced MoO_3(010) Surfaces

An important consideration for catalyst performance is the reversibility of the reduction of the oxide's surface after hydrocarbon oxidation. To investigate this reversibility, the reoxidation of MoO_{3-x}(010) surfaces, prepared by reduction in forming gas at 400 ˚C, was examined. Of particular interest was the evolution of the CS planes and pits introduced during reduction. Cleaved, mounted single crystals of MoO_3 were reduced in a flow of 10%H_2-N_2 (with 20 ppm H_2O) for a predetermined period of time at 400 ˚C. Following this reducing treatment, at least five characteristic areas on the reduced crystals were imaged with AFM and the location of these areas was noted so that they could be revisited after the oxidation treatments. Reoxidation was accomplished by heating the reduced crystals in static, ambient air at 400 ˚C. In this section, we simply describe the evolution of one of a number of crystals that was studied. This sample was first reduced for 8 min and then oxidized for times of 10, 20, 60 and 120 min in a muffle furnace. After each of these intervals, the characteristic areas on the sample were re-examined with AFM.

5.3.1 Results

Reoxidation of H_2-reduced MoO_{3-x} causes changes in the CS planes and pits that populate the (010) surface. The initial oxidation treatments of 10 and 20 min had little effect on the surface structure of a crystal reduced for 8 min at 400 ˚C. In Fig. 5.7, the CS planes which remained after a total of 30 min in air at 400 ˚C are shown. Changes in

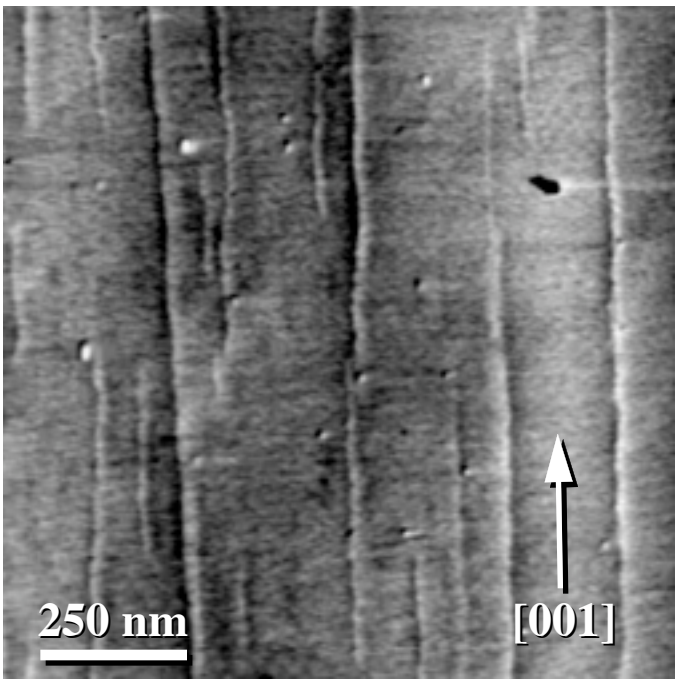

Figure 5.7 CS planes which persisted on a MoO_{3-x}(010) surface through reoxidation. This contact AFM image shows an area on a crystal which was reduced for 8 min in 10%H_2-N_2 at 400 ˚C and then oxidized in air for 30 min at the same temperature. After an additional 60 min at 400 ˚C in air, the CS planes, finally, disappeared from the surface.

the length or height of the defects were not evident after the first 30 min. After the surface was heated for an additional 60 min at 400 ˚C, however, the CS planes had vanished from this area and, in fact, all of the areas studied. A flat featureless surface was left behind after the CS planes disappeared.

Little change was evident in the surface pits after the initial 30 min of oxidation. After an additional 60 min at 400 ˚C, distinct, morphological changes became apparent. The depths of the pits increased by up to 300 Å and their edges began to show faceting parallel to <001> and <100>. After an additional 2 h, the pits were noticeably larger (up to 6 microns in length) and deeper (up to 2000 Å) and they assumed rectangular shapes bounded by {001} and {100} planes. This is shown in the before and after images in Fig. 5.8. Step edges also showed signs of erosion and faceting to {001} and {100}. Although the pit edges are oriented parallel to both <100> and <001>, they exhibit a high aspect ratio and <001> edges are clearly preferred (see Fig. 5.9).

When fresh {010} cleavage surfaces were heated under the same conditions (400 ˚C in air), but without a prior reducing treatment, only a small fraction of the surface volatilized; the process was confined exclusively to step edges and dislocations that intersected the (010) surface. Volatilization at screw dislocations led to the formation of dissolution spirals or etch pits (see Fig. 5.10). Both partial (Fig. 5.10b) and perfect (Fig. 5.10c) dislocations intersect the surface and, in most cases, the spirals were observed in groups of two or more (Fig. 5.10a). We distinguish the partials from the perfect

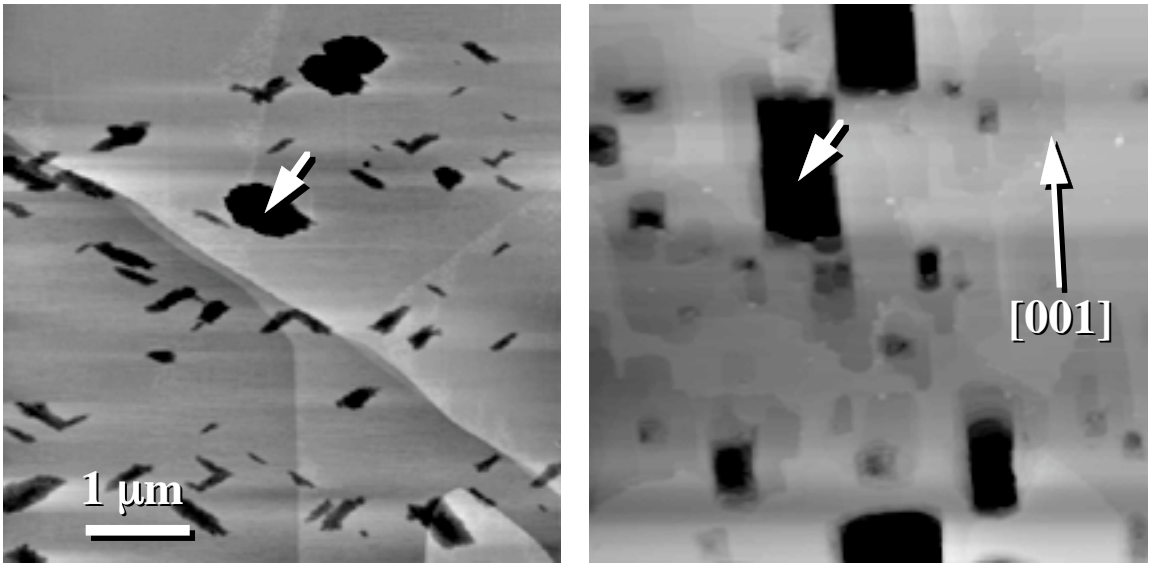

Figure 5.8 Growth and faceting of pits on MoO_{3-x}(010) during reoxidation. AFM topographs show (a) an area after reduction in forming gas for 8 min at 400 ˚C and (b) the same area after oxidation in air at 400 ˚C for 3.5 hours. The images are in the same orientation and the white arrows mark the same point on the surface. The black-to-white contrast in the images is 100 Å (a) and 400 Å (b).

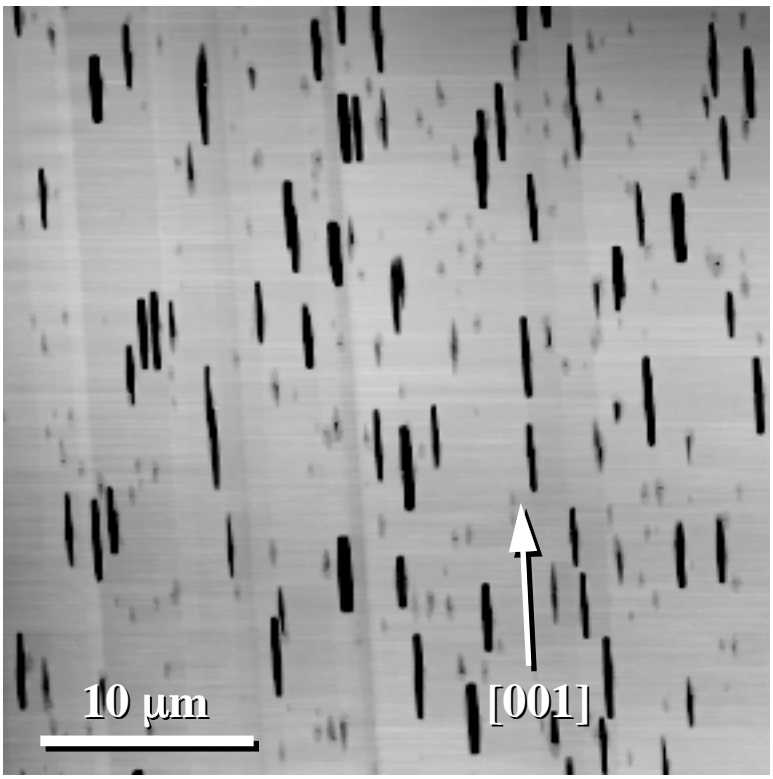

Figure 5.9 AFM topographs of <001> oriented pits on the MoO_3(010) surface after a reduction and oxidation cycle. This surface was reduced for 8 min at 400 ˚C in 10%H_2-N_2 and then reoxidized for 3.5 hours at the same temperature. The black-to-white contrast in the image is 400 Å.

dislocations because a Burgers circuit around the partials leads to a vertical displacement of 7 Å, which is only 1/2 of the b lattice parameter of MoO_3.

5.3.2 Discussion

The results presented above demonstrate that, at the same temperature, reduction in forming gas proceeds more quickly than oxidation in air. It took between 0.5 and 1.5 hours at 400˚C to remove the CS planes which were created in only 8 min during reduction at the same temperature. The surface steps associated with the CS planes persist because they can only be eliminated when the CS plane climbs completely out of the crystal. This nonconservative process requires O vacancies to diffuse from the end of the CS plane (where it terminates in the bulk of the crystal) to the surface where they are consumed by oxygen adatoms. This is the reverse of the CS plane formation process; oxygen vacancies are created at the surface and then diffuse to the end of the defect plane. Although there may be structural differences which influence the rate of diffusion, if we assume that vacancy diffusivity is the same for both processes, the slower oxidation kinetics can most easily be explained by the difference in the driving force during the two processes. During the reoxidation experiments, the chemical potential gradient was defined by lattice O in the crystal and O_2 in the surrounding gas phase. During reduction, on the other hand, the chemical potential gradient was defined by O in the crystal and

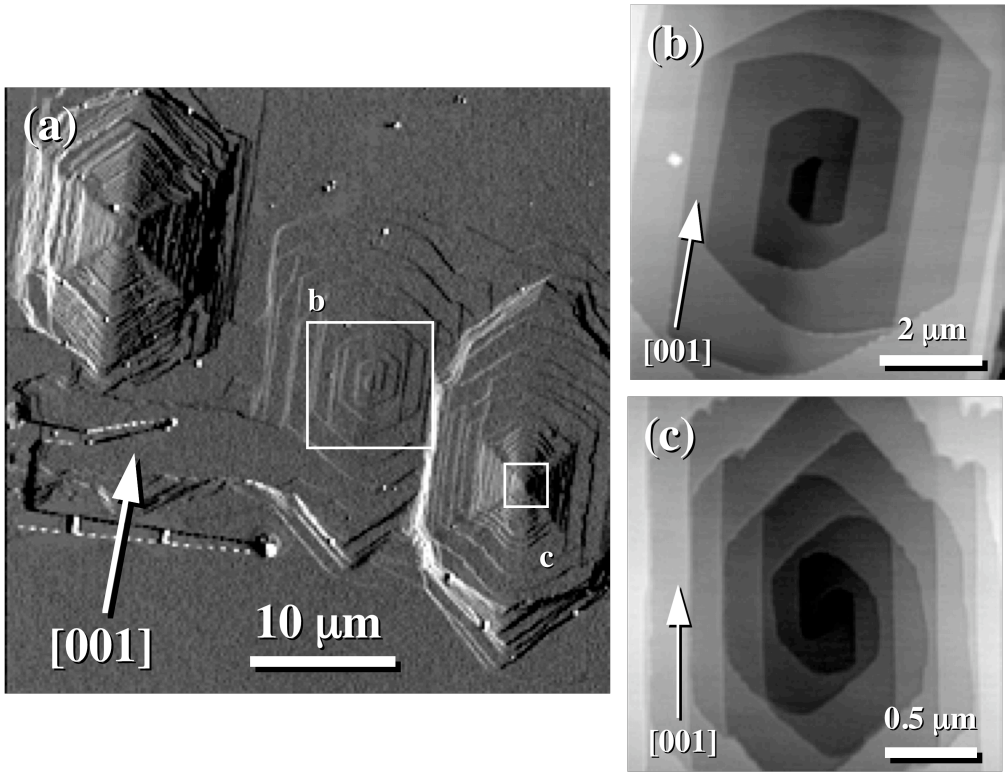

Figure 5.10 (a) AFM deflection image of a group of dissolution spirals on the MoO_3(010) surface. This surface was annealed in static air at ambient humidity for 3.5 hours at 400 ˚C. The center spiral, "b", is a partial dislocation, while the two on the edges of the image have perfect cores. The dislocation at the lower right, "c", shows both partial and perfect character and it appears that the complementary partial is the central partial screw, b. AFM topographs of the partial and perfect core are shown in (b) and (c) respectively.

H_2O in the gas phase. The latter gradient is much larger and probably responsible for the faster reduction kinetics.

Unreduced MoO_3(010) surfaces also volatilize and pit when they are annealed in air at 400 ˚C, however, pitting is confined exclusively to step edges and dislocation/surface intersections. When one considers the amount of material removed from each etch pit, it is clear that volatilization at the surface/dislocation intersections is driven by the elastic strain around the defects. Because the elastic strain energy around a dislocation line is proportional to the square of the Burgers vector, the driving force to remove material from the perfect dislocation etch pits, Fig. 5.10c ($|\mathbf{b}|$ = 14 Å), should be 4 times that of the partial dislocations, Fig. 5.10b ($|\mathbf{b}|$ = 7 Å). Measuring the depths of the etch pits and the lateral dimensions of the terraces surrounding the defect cores verified that the pits associated with perfect dislocations were 4 times deeper than those associated with partial dislocations.

Based on the observations presented here and in the last section (5.1), the two necessary conditions for pit formation are water vapor and elastic strain from extended defects such as dislocations and CS planes. CS planes introduce strain because, as they form, oxygen sites in the lattice are eliminated and the reduced surface layers of the crystal are along <**a**/2 **b**/7 0> on $\{1\bar{2}0\}$ for every CS plane formed [3,4,6]. As a result, the reduced surface layers are strained with respect to the unreduced crystal below. Furthermore, since CS planes can be thought of as stacking faults bounded by partial dislocations [6], they will have an associated long range strain field [21]. Because surface/dislocation intersections are rather infrequent, volatilization rates in oxidizing conditions are much lower than those in reducing environments where CS planes form. This implies that the density of pits should correlate with the density of CS planes and the partial pressure of oxygen in the reactor. In support of this, the results in the previous section demonstrated that pits only formed in regions of the crystal where CS planes were present. If reduction was accelerated by the presence of Ta, the pit formation process was also accelerated. Finally, we note that volatilization around step edges can also be attributed to the localized strain associated with these surface defects.

The reorientation of the pit boundaries and faceting of irregular step edges during oxidation implies that the composition of the gaseous environment influences the relative stability of the different facets during volatilization. The increase in pit depth during reoxidation is interesting because material is apparently removed from the {010} surfaces exposed at the bottom of the pits much faster than the {010} terraces introduced during cleavage. On the cleaved surface, volatilization only occurs slowly at step edges and does not lead to the erosion of entire {010} layers in the absence of an extended defect. There are two possible explanations for this.

During the initial stages of oxidation, CS planes are still present in the crystal and so is the strain associated with the defects. This strain might hasten volatilization in the same manner that it does during reduction. Once the CS planes are removed this process should cease and the bottom of the pit should flatten out. At this point, the bottom of the pit should volatilize at the same rate as the other {010} terraces. When surfaces are reoxidized completely, this appears to be the case. The increase in pit depth may also be an artifact of the AFM imaging process. Because the initial lateral sizes of the pits are comparable to the AFM tip's radius, the tip probably never reaches the bottom of narrow pits. As a result, the pit depths are underestimated. As the pits increase in size, it becomes possible to more accurately measure the depth. In all likelihood, both mechanisms probably play some role in the increasing pit depth during reoxidation.

Because volatilization does not occur below 350 ˚C, it should be possible to use the pitting process to control the morphology of the (010) surface and possibly the selectivity of MoO_3 catalysts. Appropriate heat treatments at temperatures above 400 ˚C allow one to create well defined pit structures, with {101} or {100} and {001} bounded pits, that should remain stable for indefinite periods of time when the catalyst is used below 350 ˚C.

5.4 Summary and Conclusions

During reduction in the presence of H_2O above 350 ˚C, the MoO_3(010) surface is modified by the introduction of two defects: crystallographic shear (CS) planes and surface pits. The (010) surface is not modified by thermal treatments below 300 ˚C. The presence of strain in the crystal and water in the atmosphere leads to the volatilization of MoO_3 when the temperature exceeds 350 ˚C. In oxidizing atmospheres, volatilization is confined to step edges and dislocation/surface intersections. Under reducing conditions, CS planes provide an abundant source of strain and volatilization leads to the nucleation and growth of a large population of surface pits bounded by {101}. Volatilization is facilitated by the formation of volatile Mo-oxide-hydroxides that form when MoO_3 reacts with H_2O. Reoxidation of MoO_{3-x} in air proceeds more slowly than reduction of MoO_3 in 10%H_2-N_2 at the same temperature. At 400 ˚C, it takes between 30 and 90 min to eliminate the CS planes created in only 8 min during reduction. The difference in reaction kinetics is probably determined by the difference in the chemical potential gradient during the two processes. During reoxidation, the lateral dimensions and depths of the surface pits increase. With very long oxidation treatments, the bounding edges of the pits reorient to <001> and <100>. As a result, thermal treatments can be used to alter and control the morphology of the MoO_3(010) surface.

5.5 References

[1.] R.L. Smith and G.S. Rohrer, *J. Catal.* **163** (1996) 12.

[2.] R.L. Smith and G.S. Rohrer, *in* "Catalyst Materials For High-Temperature Processes", p. 139, American Ceramic Society, Westerville, OH (1996).

[3.] L.A. Bursill, *Proc. Roy. Soc. A* **311** (1969) 267.

[4.] B.G. Hyde and L.A. Bursill, *in* "The Chemistry of Extended Defects in non-Metallic Solids", (L. Eyring and M. O'Keeffe), North Holland, Amsterdam (1970) 347.

[5.] L.A. Bursill, W.C.T. Dowell, P. Goodman, and N. Tate, *Acta Cryst.* **A34** (1974) 296.

[6.] P.L. Gai-Boyes, *Catal. Rev.-Sci. Eng.* **34** (1992) 1.

[7.] L. Kihlborg, *Arkiv Kemi* **21** (1963) 471.

[8.] G.S. Rohrer, W. Lu, R.L. Smith, and A. Hutchinson, *Surf. Sci.* **292** (1993) 261.

[9.] H. Schäfer, Chemical Transport Reactions, Academic Press, New York, NY (1964).

[10.] T. Millner and J. Neugebauer, *Nature* **163** (1949) 601.

[11.] G.R. Belton and A.S. Jordan, *J. Phys. Chem.* **69** (1965) 2065.

[12.] A.W. Sleight, *in* "Solid State Chemistry Compounds", (A.K. Cheetham and P. Day, Eds.) Oxford University Press, New York (1992) 171.

[13.] I. Nicolau, A. Aguiló, and P. DeGroot, *in* "The Chemistry and Uses of Molybdenum", (H.F. Barry and P.C.H. Mitchell, Eds.) Climax Molybdenum Company, Ann Arbor, Michigan (1992) 234.

[14.] D.R. Gaskell, Introduction to Metallurgical Thermodynamics, 2nd Ed., Hemisphere Publishing Corp., NY (1983).

[15.] E. Broclawik and J. Haber, *J. Catal.* **72** (1981) 379.

[16.] M. O'Keeffe, *in* "Fast Ion Transport in Solids, Solid State Batteries, and Devices, Proceedings of the NATO Advanced Study Institute", (W. Van Gool, Ed.) North Holland, Amsterdam (1973) 233.

[17.] M. Greenblatt, *Chem. Rev.* **88** (1988) 31.

[18.] M.R. Smith and U.S. Ozkan, *J. Catal.* **141** (1993) 124.

[19.] J.M. Tatibouet, Ch. Phichitkul, and J.E. Germain, *J. Catal.* **99** (1986) 231.

[20.] K. Brückman, R. Grabowski, J. Haber, A. Mazurkiewicz, J. Sloczynski, and J. Wiltowski, *J. Catal.* **104** (1987) 71.

[21.] D. Hull and D.J. Bacon, Introduction to Dislocations, 3rd. Ed., Pergamon Press Inc., Elmsford, NY (1984).

6

The Protonation of MoO_3 during Reactions with Alcohols

6.1 Introduction

The results of O^{18} isotopic labeling experiments [1] and temperature programmed desorption (TPD) spectroscopy [2-4] studies support the conclusion that the selective oxidation of methanol and ethanol by MoO_3 can be described by a redox mechanism of the Mars - van Krevelen type [5]. In other words, the catalyst acts as a renewable oxygen source that is able to create and annihilate stoichiometry compensating defects as it is reduced and reoxidized during the reaction. Because the mechanisms by which MoO_3 accommodates nonstoichiometry are believed to influence its reactivity [6], a number of investigators have previously studied its bulk structural evolution during reduction reactions. X-ray diffraction (XRD) studies have shown that when MoO_3 is reduced by methanol at 200-215 °C, the oxide is converted to a hydrogen bronze, H_xMoO_3 [7,8]. Numerous transmission electron microscopy (TEM) studies [9-23] have shown that a domain microstructure develops during the early stages of all reduction treatments, but this observation has not always been interpreted in the same way. In the most recent study, the notion that a hydrogen bronze forms during reduction by methanol was rejected [21], despite compelling evidence from earlier diffraction studies [7,8,15]. In this chapter, the results of AFM and X-ray diffraction (XRD) experiments designed to determine how the MoO_3(010) surface is altered by reactions with alcohol-nitrogen mixtures between 200 and 400 ˚C are described. These results lead to the conclusion that H_xMoO_3 is formed during alcohol oxidation and, therefore, provide evidence for a second and fundamentally different mechanism by which the oxide is reduced during reactions with alcohols; in addition to losing oxygen, MoO_3 intercalates H removed from the alcohol.

6.2 Reaction of MoO_3(010) with Methanol

The reaction between methanol (MeOH) and MoO_3 was studied between 200 ˚C and 400 ˚C. The single crystal samples were reacted in flowing MeOH-N_2 mixtures in the single crystal reactor described in Chapter 3. For all of the reactions at 400 ˚C, the N_2 (prepurified, Matheson) carrier gas was passed through Cu turnings at 400 ˚C and then through a column of $CaSO_4$ prior to saturating it in a bubbler of MeOH (Aldrich, 99.9+%, A.C.S. HPLC grade) maintained at 0 ˚C (unless otherwise noted). Lower temperature ($T \leq 350$ ˚C) experiments were performed with N_2 that was either passed over Cu and then dried or N_2 that was simply dried. Differences between surfaces reacted with the two different carrier gas treatments were not detected. Reactions were performed on both mounted and unmounted cleaved single crystal surfaces at atmospheric pressure with flow rates between 100 and 200 cc/min. The mounting procedure did not appear to influence the structural evolution of the surface during this reaction.

6.2.1 Reaction with MeOH at High Temperatures (T = 400 ˚C)

The atomically flat terraces of the MoO_3(010) surface are modified in two ways during a 2 min reaction in MeOH-N_2 at 400 ˚C (see Fig. 6.1). First, crystallographic shear (CS) planes intersect the surface parallel to <001>. In AFM images, the defects appear as 2 Å high surface steps with edges parallel to <001> [24,25]. The observation of CS plane formation under these conditions is consistent with previous *in situ* TEM studies and indicative of oxygen loss [21]. The second modification is the nucleation of small acicular precipitates along well defined directions of the MoO_3(010) surface plane. The angle between the axis of each precipitate and <001> is 35.5° ± 2° and this corresponds approximately to the <203> directions, which are inclined from the <001> axis by 35.56 °. The precipitates are up to a few microns long, parallel to <203>, and, as is evident by their white contrast in AFM images, they rise out of the (010) surface. After 2 min, the height of the precipitates exceed that of the matrix by 5-10 Å.

The concentration, lateral size, and height of the <203> precipitates increase with the extent of the reaction. After 4 min, they are up to 10 μm in length and rise above the MoO_3 matrix by approximately 30 Å (see Fig. 6.2). After 6 min (see Fig. 6.3), the length and height of the precipitates can be up to 40 μm and 100 Å, respectively. During later stages of the reaction, new surface steps form parallel to <001>. These step defects, which can be seen in Fig. 6.3, sometimes originate near the end of a precipitate and we distinguish them from the surface/CS plane intersections because their height is typically greater than 20 Å. After a 10 min reaction at 400 ˚C in MeOH-N_2 (see Fig. 6.4), the surface microstructure is dominated by large <203> precipitates that can have lengths in

excess of 100 μm and heights of up to 200 Å. At this stage, the precipitates can easily be observed with a conventional optical microscope. Across the surface, the precipitates bound distinct regions within which many <001> steps and smaller <203> precipitates can be found.

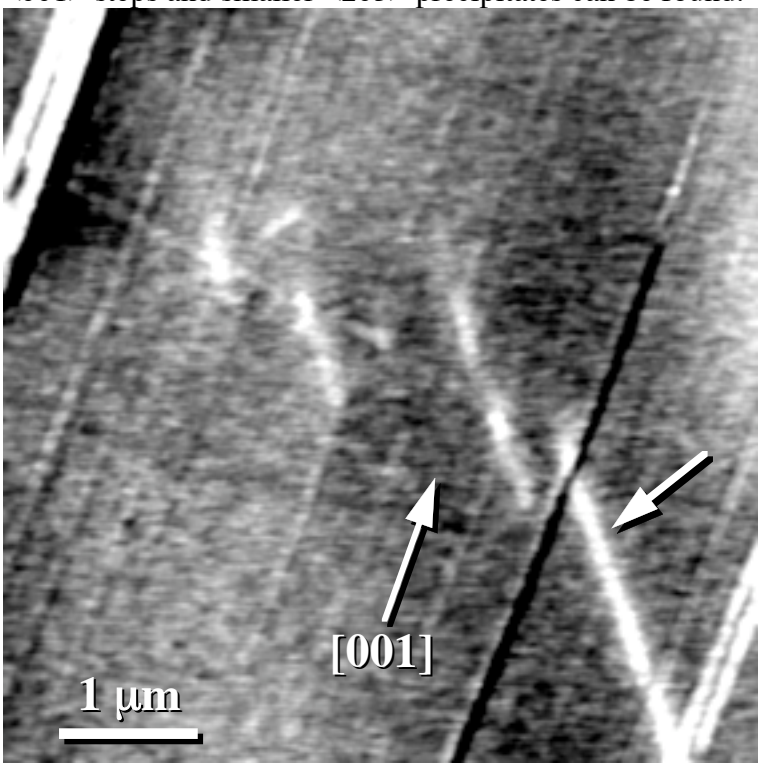

Figure 6.1 AFM topograph of a MoO_3(010) surface which was reacted for 2 min at 400 ˚C in N_2 saturated with MeOH at 0 ˚C. CS planes are visible along <001> and precipitates are seen parallel to <203>. One of the <203> precipitates is indicated with and arrow in the figure. The black-to-white contrast in the image is 20 Å.

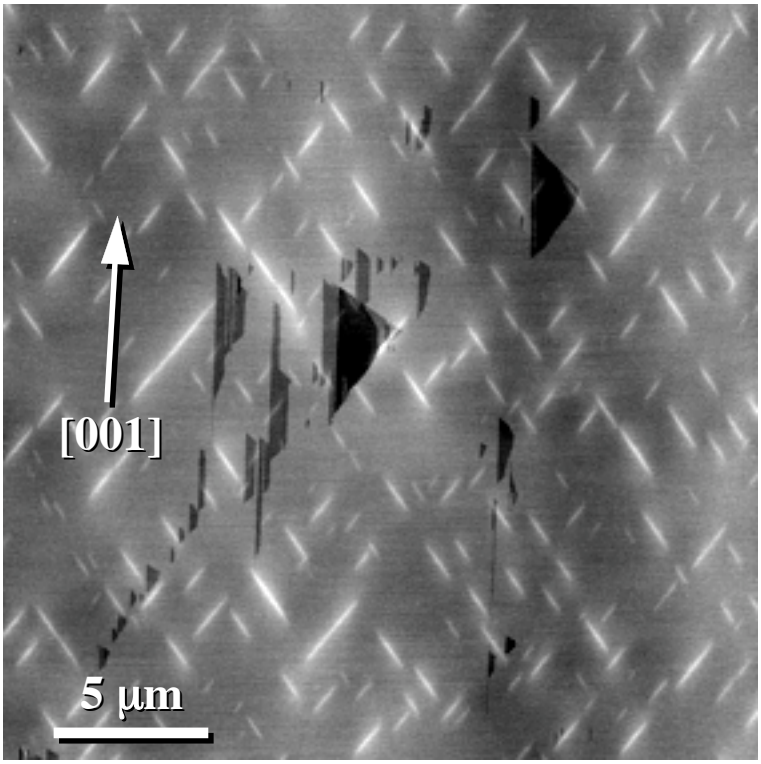

There are several noteworthy features of the surface

Figure 6.2 AFM topograph of a MoO_3(010) surface after a 4 min reaction at 400 ˚C in N_2 saturated

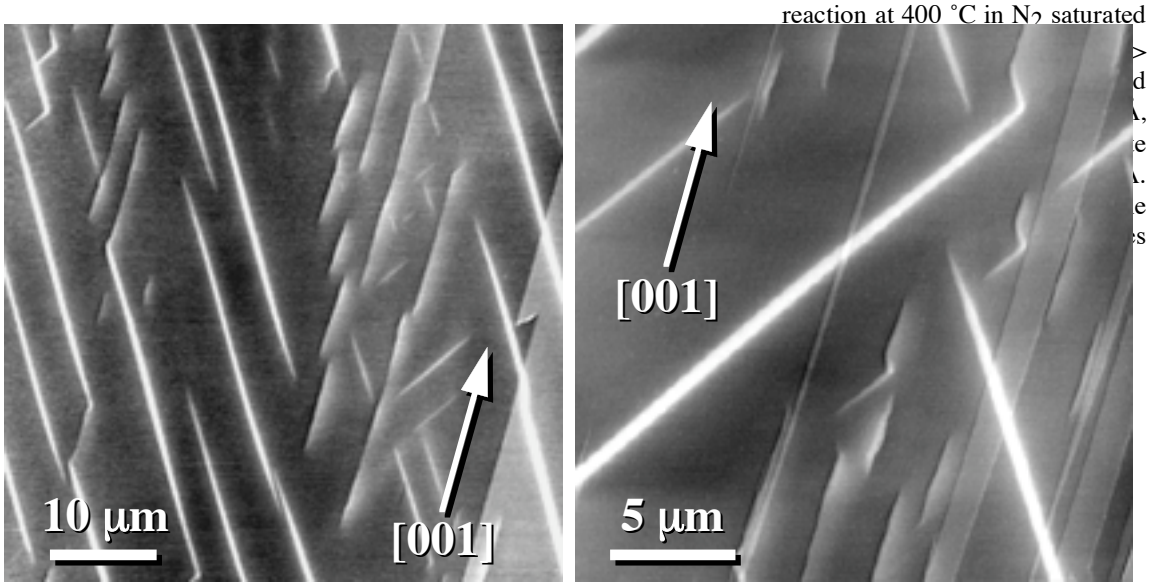

Figure 6.3 AFM topographs of a MoO_3(010) surface which was reacted with N_2 saturated with MeOH at 0 ˚C for 6 min at 400 ˚C. Note the interaction between the <203> precipitates and the <001> steps, especially in the image on the right. At this stage, the precipitates may have heights of up to one hundred angstroms, while the <001> steps have heights of up to 50 Å. The black-to-white contrast in the images is 150 Å.

microstructure formed during the MeOH reaction. First, precipitates oriented parallel to [203] rarely intersect those oriented parallel to [$\bar{2}$03] and vice versa. They always terminate in a point just before making contact with another precipitate. However, if both precipitates terminate at a common point on the surface, they appear to coalesce. A second interesting feature is the depletion zone, directly adjacent to the precipitates and normal to their long <203> axis, in which no surface defects are observed. This indicates that the largest precipitates are growing at the expense of the smaller ones. The width of the depletion regions is approximately 2 microns on the surface in Fig. 6.4. Time-lapse studies, in which the same areas of the surface were imaged after consecutive 2 min heating intervals, demonstrated that many of the precipitates which nucleated during the first treatment grew during subsequent treatments and, therefore, the precipitates persist throughout the heating and cooling cycle. The large <203> precipitates persist up to reaction times in excess of 20 min at 400 ˚C. Within 40 min, however, the surface becomes very rough (see Fig. 6.5). At this point, only the largest <203> precipitates are clearly resolvable with AFM and it appears that these are also be disappearing into the roughened (010) surface.

Control experiments were conducted to ensure that exposing the surface to the ambient, after the MeOH reaction, did not alter the surface microstructure. After reaction, these MoO_3 samples were transferred directly to a glove box (with a dry, oxygen free atmosphere) without exposing them to the ambient. They were then imaged within the controlled atmosphere of the glove box. The surface structures observed in Ar and the ambient were identical and exposure of the surface to the ambient, for up to a day, did not alter the surface structure at the detection level afforded by AFM. Finally, as the reaction progresses, the color of the single crystals change from transparent, pale green (fresh) to transparent, dark blue ($t \approx 6$ min) to opaque, blue-purple ($t \approx 10$ min) to dark, purple-black ($t \approx 40$ min).

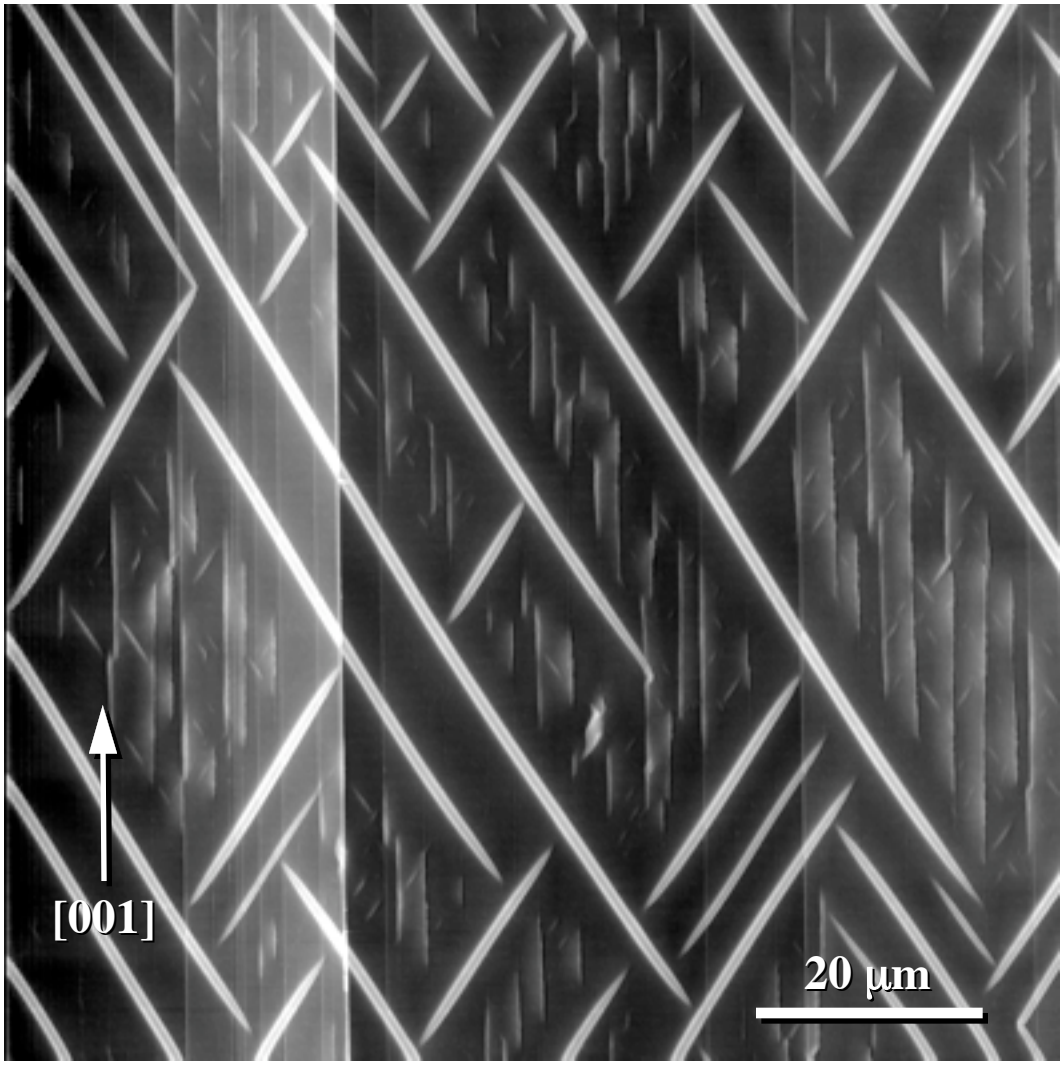

Figure 6.4 AFM topograph of a MoO_3(010) surface which was reacted for 10 min at 400 ˚C with N_2 saturated with MeOH at 0 ˚C. The acicular <203> precipitates never cross one another unless their ends terminate at a common point on the surface. The precipitates are bordered by a depletion region in which <203> precipitates and <001> steps are not observed. The black-to-white contrast in the image is 300 Å.

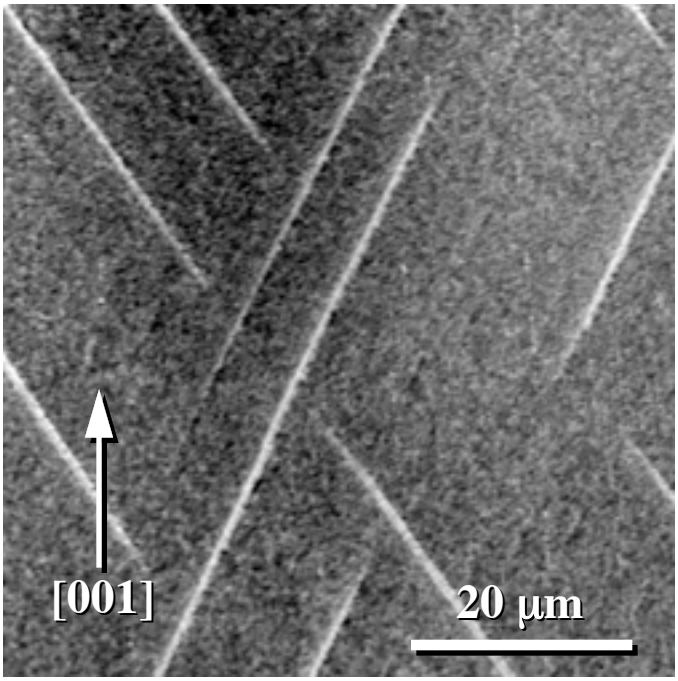

Figure 6.5 AFM topograph of a MoO_3(010) surface which was reacted with N_2 saturated with MeOH at 0 ˚C for 40 min at 400 ˚C. Within this period of time, the surface has roughened substantially and the <203> precipitates have begun to disappear. The black-to-white contrast in the image is 400 Å.

6.2.2 Reaction with MeOH at Low Temperatures (T ≤ 350 ˚C)

Identical <203> precipitates form on MoO_3(010) surfaces during reactions with MeOH-N_2 mixtures below 350 ˚C. At this temperature, however, CS plane/surface intersections are never observed and the <001> step defects do not form until the surface is covered with a dense, cross hatched pattern of <203> precipitates. Another noteworthy difference between the high and low temperature reactions is that surfaces reacted at less than 330 ˚C were almost impossible to image with contact AFM in the ambient. These surfaces were prone to image artifacts and tip induced etching. The surfaces could, however, be studied with noncontact AFM, optical microscopy, and with contact AFM within the dry Ar atmosphere of a glove box.

At 330 ˚C, the precipitation reaction occurs more slowly than it does at 400 ˚C, with equivalent gas mixtures (i.e. N_2 saturated with MeOH at 0 ˚C.) However, if the *p*MeOH is increased, by saturating the N_2 at ~ 25 ˚C, the speed of the reaction can be increased. The MoO_3(010) surface in Fig. 6.6 was reacted with N_2 saturated with MeOH at 25˚C for 8 min at 330 ˚C. Within this time, a dense cross-hatched pattern of <203> precipitates has formed. With longer reaction times, the precipitates coarsen and then begin to coalesce along <001>, see Fig. 6.7. These long straight features typically nucleate at the {001} edges of single crystals and then grow along <001> toward the center of the crystal. The swelling of the surface along these features can be up to 500 Å, while the precipitates between them are only 200 Å high. In gray scale images the

features look similar to the <001> steps formed at 400 ˚C However, in cross section, they look like two steps of opposite sign facing each other. In other words, they look like a pyramidal cone with a straight crack propagating along its length. A second difference is that the height of these long, straight features is always greater than that of the precipitates, not less, as was the case for the <001> steps observed at 400 ˚C. Eventually, the features extend the entire length of the crystal. If the reaction is run at the same temperature, but with a lower *p*MeOH, the same microstructural features are observed but they take longer to form.

At 300 ˚C, the nucleation and growth rates of the precipitates are significantly slower, but again, the rate can be increased by using a higher *p*MeOH. After reaction times of 15 min in N_2 saturated with MeOH at 0 ˚C, the observed precipitates are small and they are often confined to local regions of the crystal's surface. However, small

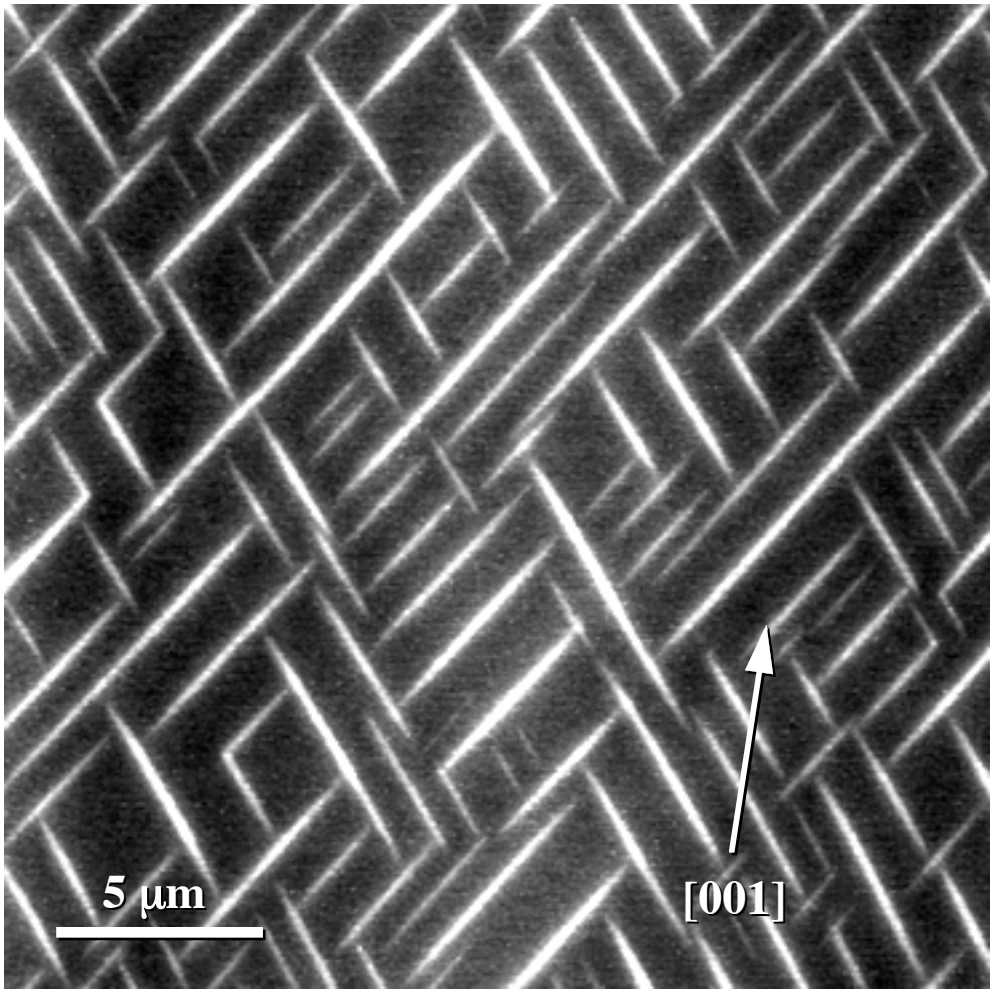

Figure 6.6 Contact AFM image of a MoO_3(010) surface which was reacted for 8 min at 330 ˚C in N_2 saturated with MeOH at 25 ˚C. This image was acquired in an Ar atmosphere. The black-to-white contrast in the image is 50 Å.

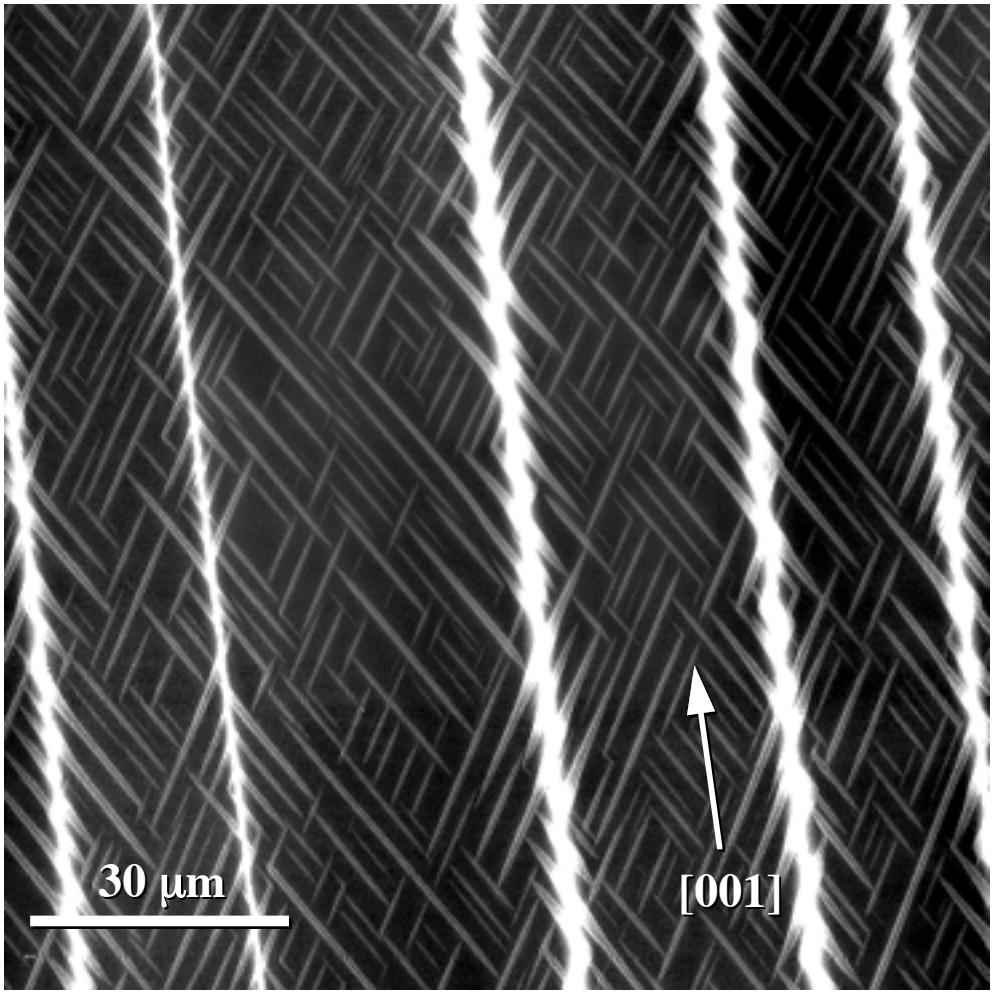

Figure 6.7 AFM topograph of a MoO_3(010) surface which was reacted for 30 min at 330 ˚C in N_2 saturated with MeOH at 25 ˚C. The black-to-white contrast in the image is 500 Å. The height of the long, straight precipitates oriented along <001> may exceed 500 Å. The <203> precipitates between the <001> precipitates are less than 300 Å high. This image was acquired in Ar.

crystallites, which were reacted along with the single crystals, always contained the precipitates and they could be resolved with the optical microscope (see Fig. 6.8). After one hour at 300 ˚C, {010} surfaces are populated with large <203> precipitates with sizes and concentrations comparable to those observed after 10 min at 400 ˚C. This is illustrated in the optical micrograph in Fig. 6.9 and the noncontact AFM image in Fig. 6.10. Finally, surfaces reacted at 200 ˚C in N_2 saturated with MeOH at room temperature were unchanged after reaction times of up to two hours.

In summary, Three distinct modifications are introduced to the MoO_3(010) surface during reactions with MeOH-N_2 mixtures: CS planes, <203> precipitates, and <001> steps. The <203> precipitates and <001> steps were observed between 300 ˚C and 400˚C while CS planes were only observed at 400 ˚C. It is not clear, however, if the

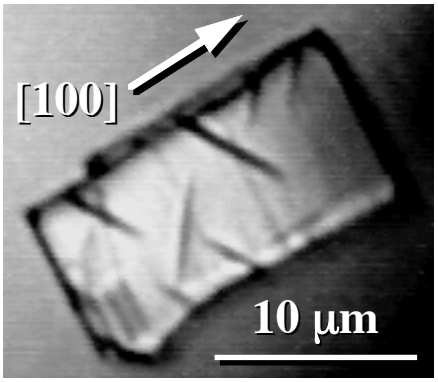

Figure 6.8 Optical micrograph of <203> precipitates on a MoO_3 particle which was reacted with N_2 saturated with MeOH at 0 ˚C for 15 min at 300 ˚C.

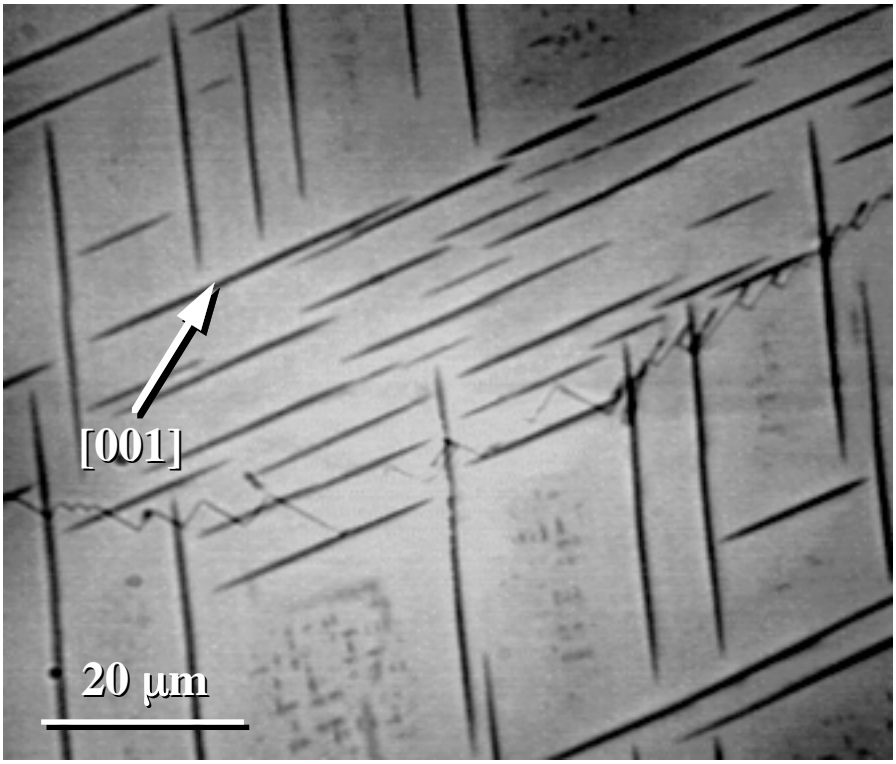

Figure 6.9 Optical micrograph of a MoO_3 (010) surface which was reacted with N_2 saturated with MeOH at 0 ˚C for one hour at 300 ˚C. The <203> precipitates appear as a dark contrast. Note the presence of smaller precipitates within the regions between the largest precipitates.

steps observed at high temperature are the same steps observed at low temperatures. At high temperatures, the steps were usually small and always shorter (topographically) than the precipitates. Conversely, the <001> features formed at low temperatures were long (up several mm) and continuous and always topographically higher than the precipitates. The existence range of the CS planes in N_2-MeOH was identical to that observed in forming gas, $T \geq 350$ ˚C.

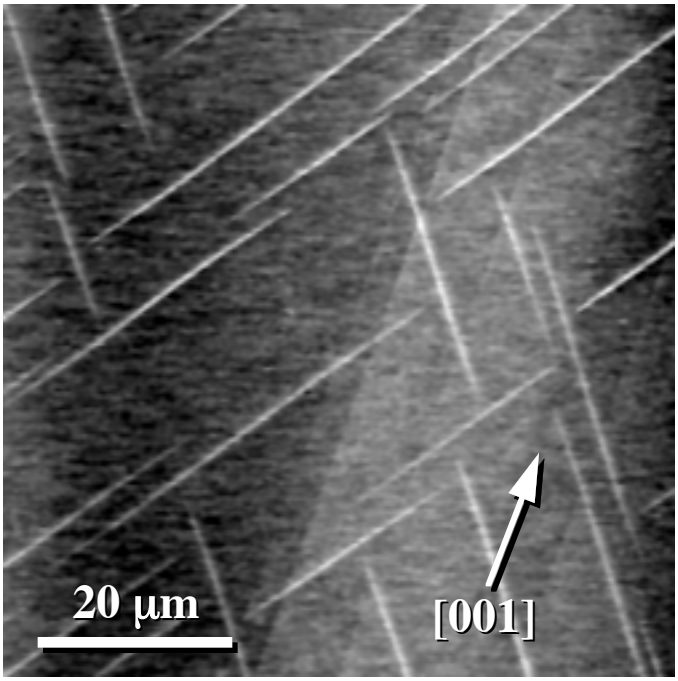

Figure 6.10 Noncontact AFM image of a MoO_3(010) surface which was reacted for one hour at 300 ˚C in N_2 saturated with MeOH at 0 ˚C. The <203> precipitates have heights of up to 100 Å.

6.2.3 <203> Precipitate Identification

X-ray Analysis of the <203> Precipitates. X-ray diffraction (XRD) was used to unambiguously identify the <203> precipitates which form during reactions with MeOH. First, several MoO_3 single crystals were reacted with MeOH-N_2 for 10 min at 400˚C to produce a surface microstructure dominated by the large acicular precipitates, as in Fig. 6.4. Subsequently, thin surface layers, rich in the precipitate phase, were cleaved from these crystals with adhesive tape, pulverized, and subjected to powder XRD analysis. The powder pattern from these reacted surface layers clearly shows that it is a two phase mixture. In Fig. 6.11, a portion of the XRD pattern from the reacted surface layers is compared to that of unreacted MoO_3 so that the peaks from the second phase can be easily identified. The new peaks in the XRD pattern of the reacted material, which we associate with the <203> precipitates, can be indexed to a C-centered orthorhombic cell with refined lattice parameters (a = 3.8830 (9), b = 14.0538 (25), c = 3.7282 (16)) identical to those of the hydrogen bronze phase, H_xMoO_3, where $0.23 \leq x \leq 0.4$ [28]. Every peak in the XRD pattern can be indexed to either MoO_3 or H_xMoO_3. A search of the JCPDS-ICDD file revealed that this hydrogen bronze, H_xMoO_3, is the only known phase containing combinations of Mo, O, C, N, or H that has a structure and lattice parameters consistent with the diffraction patterns. In Table 6.1, the refined lattice

parameters of the <203> precipitates and the MoO_3 matrix produced during the reaction with MeOH-N_2 are compared to the established lattice parameters of MoO_3 and $H_{0.34}MoO_3$ [28,33].

The cleaved surface layers from samples treated for 1 h at 300˚C in MeOH-N_2 gave identical X-ray diffraction patterns. Because these samples did not contain CS planes or step defects, we can be confident in our association of the new diffraction peaks with the <203> precipitates. Powdered MoO_3 samples reacted with MeOH-N_2 at 300 ˚C for times between 30 and 60 min had an improved signal to noise ratio and exhibited the same characteristic peaks of H_xMoO_3. These powder patterns confirmed the lattice parameters of the bronze and displayed the systematic absences characteristic of space group Cmcm. Like the patterns from cleaved surface layers, all the peaks in the powder pattern could be indexed to either MoO_3 or H_xMoO_3. Finally, XRD patterns of surfaces reacted to form microstructures similar to that Fig. 6.7 also exhibited only the

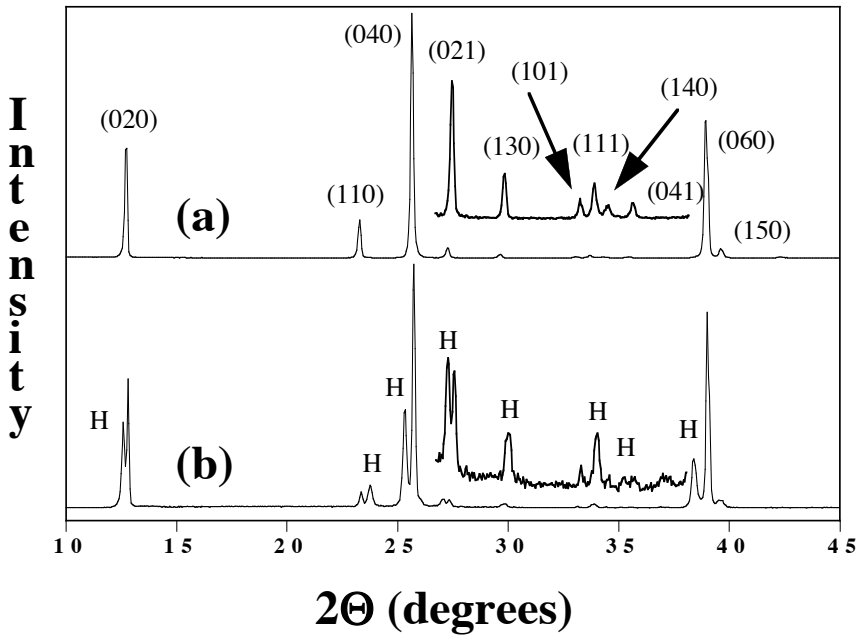

Figure 6.11 (a) Powder XRD pattern of unreacted MoO_3. This phase has a primitive orthorhombic cell (Pbnm) and its lattice parameters are a = 3.963 Å, b = 13.856 Å, c = 3.6966 Å. The intensities in the section between 26 ° and 37 ° have been magnified in the inset to show detail. (b) Powder XRD pattern of pulverized surface layers, cleaved from MoO_3 single crystals which were reacted for 10 min in MeOH-N_2 at 400 °C. Peaks that do not arise from MoO_3 are labeled with an H. This subset of new peaks can be fully indexed to the C-centered orthorhombic cell (Cmcm) of H_xMoO_3, where $0.23 \leq x \leq 0.4$ (28); its lattice parameters are a = 3.8830(8) Å, b = 14.0538(25) Å, c = 3.7282(16) Å. The (130) and (111) peaks of both phases overlap and the (101) and (140) peaks of the H-bronze are absent due to the Bravais lattice symmetry.

Table 6.1 Lattice parameters of pure MoO_3 [33], $H_{0.34}MoO_3$ [28], the MoO_3 matrix of a crystal reacted in MeOH-N_2 at 400 ˚C (matrix), and the <203> precipitates which form during the reaction with MeOH.

Phase	a (Å)	b (Å)	c (Å)	error (R)
MoO_3	3.9630	13.856	3.6966	NA
$H_{0.34}MoO_3$	3.8962	14.066	3.7361	NA
MoO_3 (matrix)	3.9588(8)	13.8395(34)	3.6931(18)	1.399
<203> precipitate	3.8830(9)	14.0538(25)	3.7282(16)	1.340

characteristic diffraction peaks of MoO_3 and H_xMoO_3. It is therefore possible that the long, straight precipitates are a second bronze habit.

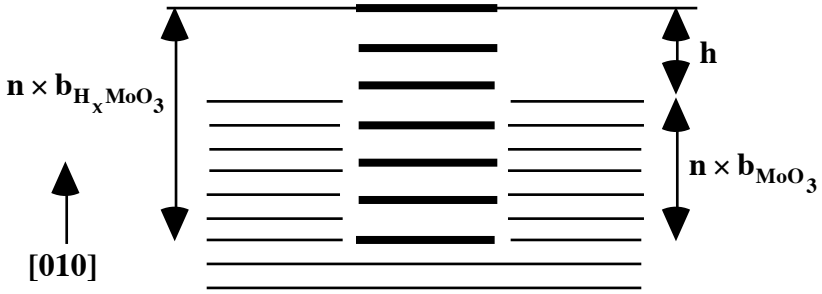

Figure 6.12 Schematic representation of the geometric relationship between the H_xMoO_3 precipitates and the MoO_3 matrix. The difference in the interlayer spacings of the bronze and the MoO_3 matrix are exaggerated in this illustration.

Diffraction experiments with reacted single crystals demonstrated that the **b** lattice vectors of the matrix and the H_xMoO_3 precipitates were parallel. Thus, this transformation progresses in a topotactic manner that is characteristic of intercalation reactions [32]. Because the b lattice parameter of the protonated phase is 0.2 Å larger than that of pure MoO_3, the precipitates swell 0.2 Å above the matrix phase for every unit layer of the structure that has been transformed to H_xMoO_3. The geometric relationship between the two phases is illustrated schematically in Fig. 6.12. Based on this geometric relationship, a 200 Å high precipitate consists of 1000 unit layers of H_xMoO_3 and has a thickness of approximately 1.4 μm parallel to **b**.

Infrared (IR) Spectroscopy. As a final check of the identification of the <203> precipitates as a hydrogen bronze, powdered MoO_3 samples were reacted with MeOH-N_2 at 300˚C and then characterized with FTIR spectroscopy. The powder was first reacted with N_2 saturated with MeOH at 25 ˚C for one hour at 300 ˚C and, subsequently,

transferred to a glove box, without exposing the sample to the ambient. It was then combined with CsI (or KBr) to produce a mixture which was approximately 5% (volumetrically) reacted MoO_3 powder. This mixture was then loaded into a 1 cm diameter steel die and transferred to a uniaxial press in the ambient where a thin pellet was pressed. The pellet was immediately analyzed with a FTIR spectrometer (Mattson) in the ambient.

The IR transmission spectrum obtained from this powder, shown in Fig. 6.13, is qualitatively consistent with those that have been published previously for H_xMoO_3 [35-39]. However, there is not general agreement on the wave numbers associated with the Mo-O bonds in the bronze structure. In particular, the bands centered at approximately 635, 576, and 444 cm^{-1} may vary by ± 20 cm^{-1} in the literature. Similar inconsistencies are apparent in the published IR spectra of α-MoO_3 samples [40]. These differences in the observed wave numbers are most likely attributable to differences in sample preparation and, in particular, its effect on the stoichiometry of the oxide. Because of this, we should expect no less variation in the spectra of hydrogen bronzes synthesized in different ways with different source powders. For example, the combined XRD and IR studies of Eda [35] and Sotani et al. [36,37] have demonstrated that the vibrational

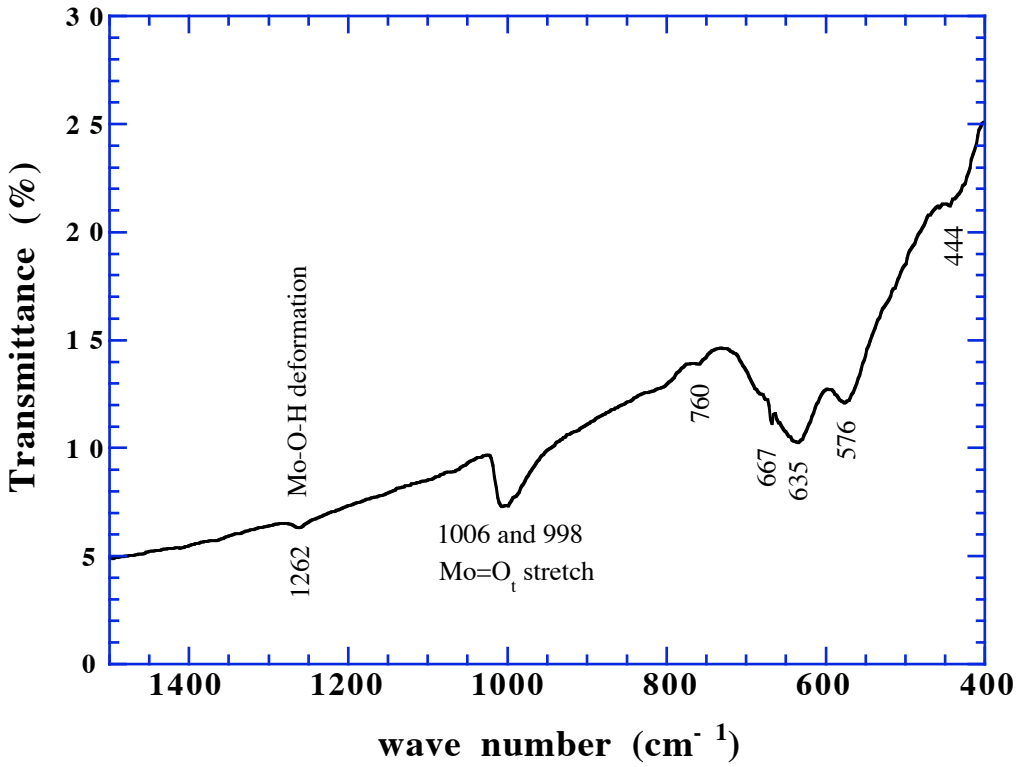

Figure 6.13 IR transmission spectrum of MoO_3 powder which was reacted with N_2 saturated with MeOH at 0 °C for one hour at 300°C.

frequencies of the bronze can vary with the hydrogen and oxygen content of partially dehydrated bronzes. Although dehydration does not always lead to changes in the XRD pattern below ~390 ˚C, it invariably leads to shifts in the vibrational frequencies.

Birtill [28,38] has performed the most thorough structural studies of the hydrogen molybdenum bronzes and has also used IR spectroscopy to characterize the orthorhombic "blue bronze", H_xMoO_3, where $0.23 \leq x \leq 0.40$. The IR spectrum in Fig. 6.13 is essentially identical to that published by Birtill et al. [38]. Most importantly, this spectrum reproduces the Mo-O-H deformation band, at 1267 cm^{-1}, associated with the hydroxylated Mo-O-Mo bridging oxygen atoms within the double octahedral layers of the H_xMoO_3 structure. During the course of the present study, additional IR spectra were recorded of MoO_3 samples which had been dried in air at 300 ˚C, reduced in wet H_2 between 200 and 300 ˚C, or allowed to equilibrate with the ambient for months at room temperature. The band at 1267 cm^{-1} was not reproduced in any of the samples. It was only observed in samples which were reduced with gas phase MeOH and samples reduced with Zn/HCl, conditions under which the bronze is known to form [28,31,32].

6.3 Reactions with Ethanol and 2-Propanol

Additional experiments were conducted to explore the conditions under which H_xMoO_3 forms during gas phase redox reactions. When analogous experiments were conducted with N_2-ethanol (EtOH) and N_2-propanol (2-PrOH) mixtures, identical <203> oriented precipitates were observed with AFM and X-ray diffraction patterns from the reacted surface layers of these crystals showed the same characteristic peaks of H_xMoO_3. Topographic AFM images of MoO_3(010) surfaces reacted with EtOH and PrOH at 400 ˚C are presented in Figs. 6.14 and 6.15, respectively. During the course of this study, H_xMoO_3 precipitates were never observed on MoO_3(010) cleavage surfaces which had been reacted with N_2, 10%H_2-N_2, or CO between 200 and 400 ˚C.

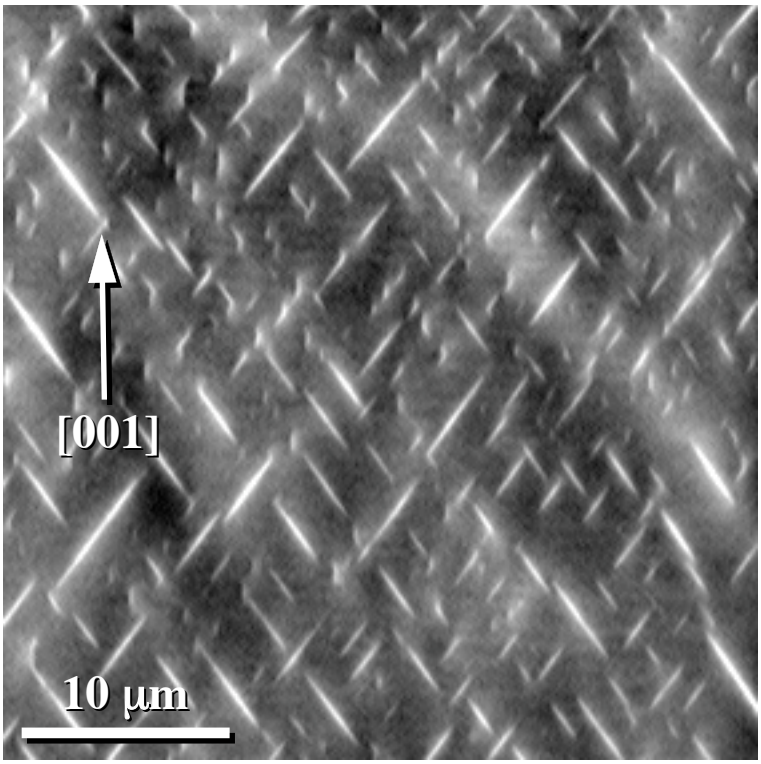

Figure 6.14 AFM topograph of a MoO_3(010) surface which was reacted for 5 min at 400˚C in N_2 saturated with EtOH at 0 ˚C. The black-to-white contrast in the AFM image is 45 Å.

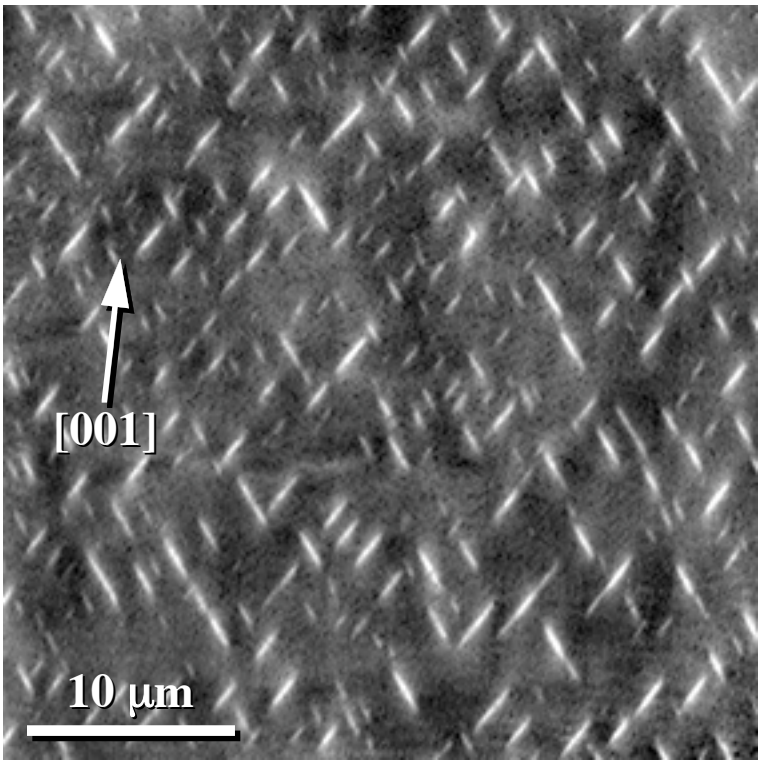

Figure 6.15 AFM topograph of a MoO_3(010) surface which was reacted for 5 min at 400˚C in N_2 saturated with 2-PrOH at 25 ˚C. The black-to-white contrast in the AFM image is 40 Å.

6.4 Reoxidation of H_xMoO_3 in Air

Several experiments were performed to explore the reoxidation behavior of MoO_3(010) surfaces which had been protonated via reduction in MeOH-N_2. Samples were first reacted with MeOH-N_2 at 400 ˚C and then oxidized at the same temperature in static air in a muffle furnace. The results of these experiments demonstrated that reoxidation occurs quickly and possibly as fast as protonation. For example, the surface in Fig. 6.16a was reacted for 8 min at 400 ˚C with N_2 saturated with MeOH at 0 ˚C. After a reoxidation treatment of 10 min at 400 ˚C, the surface relief associated with the H_xMoO_3 precipitates and <001> steps disappeared (Fig 6.16b). Closer inspection of the surface, however, reveals that the process is not completely reversible as the surface is left scarred after reoxidation (Fig. 6.16c). In particular, the surface is recessed in the regions which contained precipitates and <001> steps prior to oxidation. The surface of the crystal is transparent blue following oxidation and, therefore, probably remains oxygen deficient.

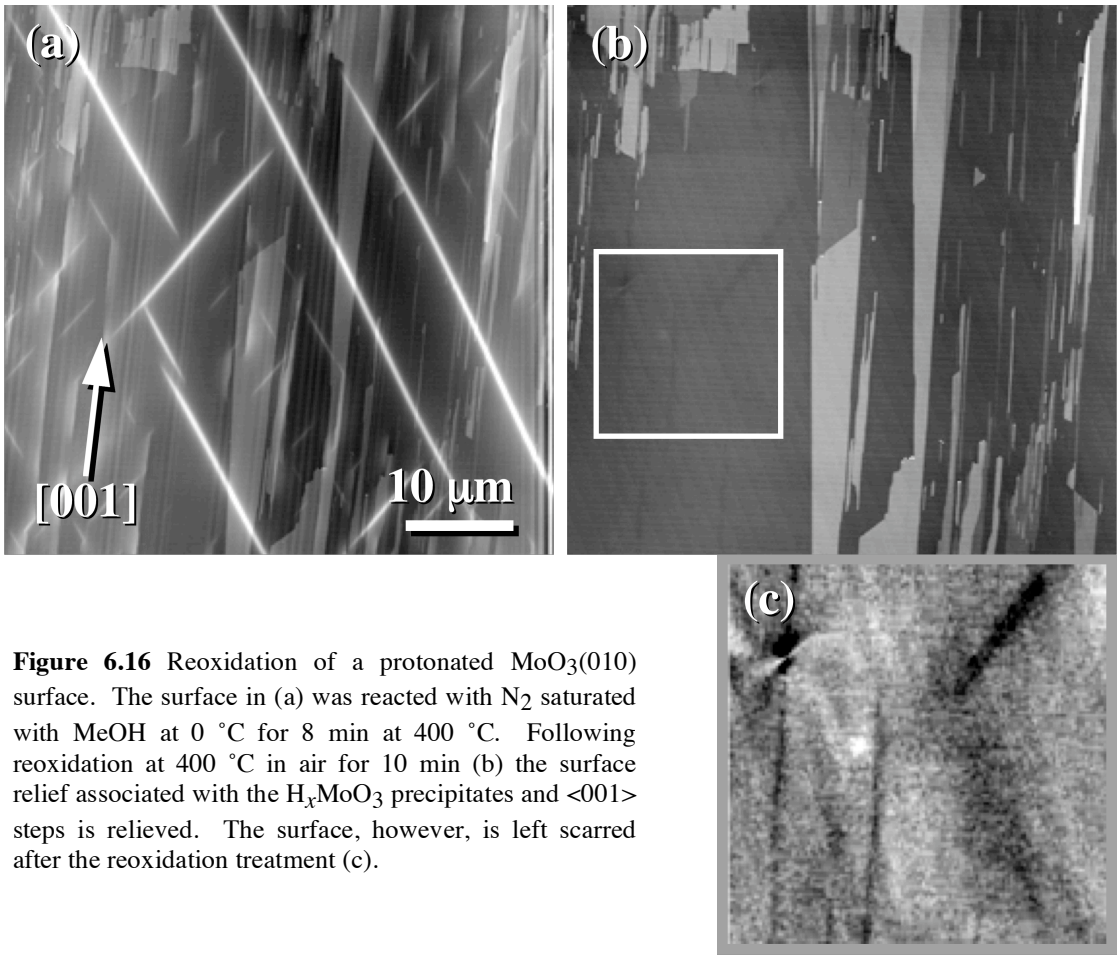

Figure 6.16 Reoxidation of a protonated MoO_3(010) surface. The surface in (a) was reacted with N_2 saturated with MeOH at 0 ˚C for 8 min at 400 ˚C. Following reoxidation at 400 ˚C in air for 10 min (b) the surface relief associated with the H_xMoO_3 precipitates and <001> steps is relieved. The surface, however, is left scarred after the reoxidation treatment (c).

6.5 Protonation of MoO_3 during H Spill Over

H_xMoO_3 is a well known product of reactions with atomic H produced by "spill over" from supported or admixed Pt particles [26-30] and, therefore, the surface evolution under these conditions should provide an interesting comparison to that observed during reactions with alcohols. The interaction between the MoO_3(010) surface and atomic hydrogen was studied between 25˚C and 200 ˚C. Pt-supporting {010} surfaces were prepared by dipping cleaved, mounted single crystals in a dilute (0.08 w/o) suspension of Pt black in methanol that was prepared by sonication. Following deposition, the solvent was evaporated by heating the samples overnight in air at 160˚C. Experiments were also conducted with excess Pt. These samples were prepared by sprinkling a ~1 mm thick layer of Pt black on cleaved, mounted single crystals which were held in an alumina crucible. To avoid contaminating the quartz reaction tube with the noble metal, the Pt-excess samples were reacted in a flow of dry forming gas in a Pyrex 3-neck flask that was heated with a spherical, resistive heating mantle. The temperature was monitored with a thermocouple that was positioned in contact with the alumina crucible in which the sample was held. At the conclusion of the reaction, the surface was blasted with N_2 (g) to remove the excess Pt. All reactions were performed at atmospheric pressure in a 200 cc/min flow of gas. Control experiments were conducted with dry CO and N_2.

When Pt-supporting MoO_3 crystals are reacted with dry forming gas at 130 ˚C, the (010) surface is modified in a manner similar to that observed during reactions with alcohols. The AFM deflection image in Fig. 6.17 shows a Pt-supporting (010) surface which was reacted with forming gas for 60 min at 130 ˚C. Small, acicular precipitates, oriented along <203>, originate at the Pt particles and form preferentially along the <001> axis of the MoO_3 matrix. In topographic AFM images, the precipitates appear as a white contrast and they rise up to 30 Å above the matrix.

When crystals are reacted with excess Pt, by covering the surface with a thick (~1 mm) layer of Pt black, the formation of the <203> precipitates is significantly faster. After 30 min at 130 ˚C, most of the (010) surface is decorated with a well-developed, cross-hatched pattern of <203> precipitates, as in Fig. 6.18. A secondary feature of the reaction surface is the regions of enhanced swelling (the whitest portions of the image) which are parallel to the <001> axis of the MoO_3 crystal. In these regions, it appears that the <203> precipitates may be coalescing.

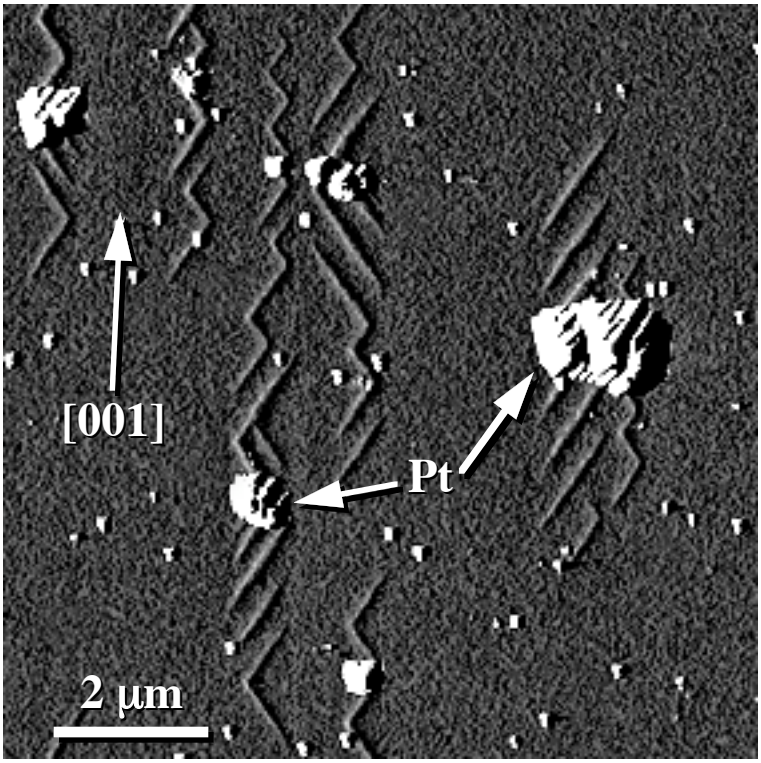

Figure 6.17 AFM deflection image of a Pt-supporting MoO_3(010) surface which was reacted with 10%H_2-N_2 at 130 ˚C for 60 min. For clarity, two Pt particles are indicated with arrows. The deflection image is used here to maximize the dynamic contrast range in the image. The <203> precipitates are up to 40 Å high while the Pt particles may be up to 1 μm high.

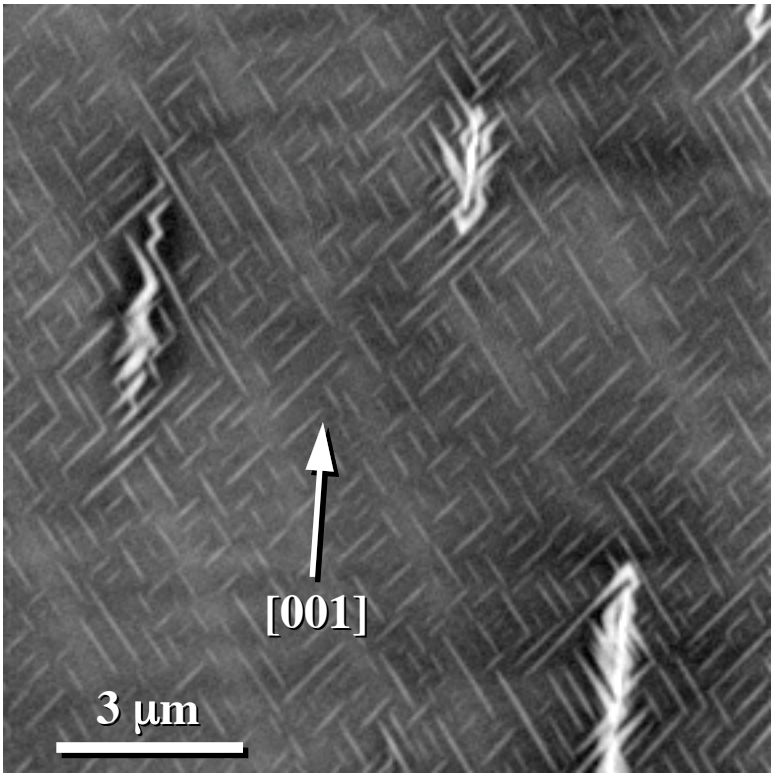

Figure 6.18 AFM topograph of a MoO_3(010) surface which was reacted with atomic H for 30 min at 130 ˚C. This surface was coated with excess Pt and reacted in 10%H_2-N_2. Note the cross-hatched pattern of precipitates oriented parallel to <203>. Regions of white contrast, along <001>, have heights on the order of 50 Å. The black-to-white contrast in the image is 50 Å.

After 60 min (Fig. 6.19), the crystals take on a dark blue color and the <203> precipitates coarsen. The surface relief which they introduce is now on the order of 75 Å. The density of the diffuse swollen regions parallel to <001>, which were seen after 30 min on Pt-excess samples, increases and, in some cases, they develop into steps with edges that are parallel to <001>. The surface relief introduced by the steps is always greater than that introduced by the precipitates. These small steps may be precursors to the macroscopic <001> steps which have been observed optically on MoO_3 crystals that have been transformed to $H_{1.68}MoO_3$ by spill over [29,30]. The regions of the surface which do not contain the <203> precipitates roughen to the extent that they are nearly impossible to image with AFM. The surface topography in these rough regions typically shows height variations in excess of 5 μm. These large (up to 40,000 μm^2) areas are always elongated along <001> and are distinguishable, in the optical microscope, by their dark blue color. The highest concentration of <203> precipitates is usually found directly adjacent to these rough areas of the (010) surface. We presume that these optically distinct regions reacted (protonated) at an accelerated pace.

Phase analysis, with XRD, of the surface layers of crystals reacted with Pt-excess for 30 min and Pt/MoO_3 powders reacted for as little as 2 min in $10\%H_2$-N_2 confirmed the expected presence of MoO_3 and H_xMoO_3. However, in addition to the hydrogen bronze with $0.23 \leq x \leq 0.4$, a second intercalated phase with

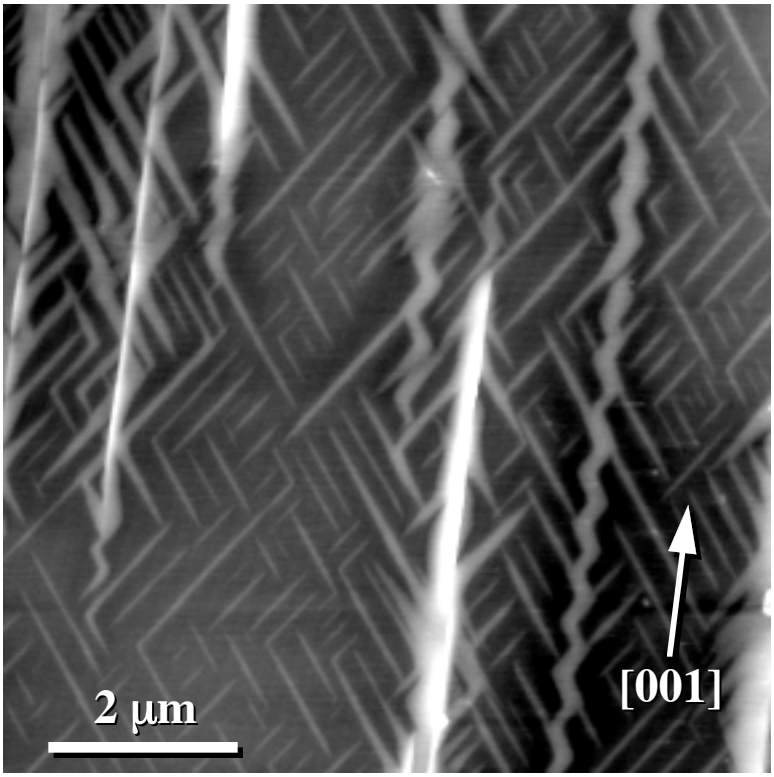

Figure 6.19 AFM topograph of a MoO_3 (010) surface (which was coated with excess Pt) after reaction with forming gas for 60 min at 130˚C. The black-to-white contrast in the image is 75 Å.

$0.85 \leq x \leq 1.04$ [28], was also present. In Fig 6.20, a XRD pattern from a powdered Pt/MoO_3 mixture reacted for 5 min at 25 ˚C with $10\%H_2$-N_2 is compared to a XRD pattern of pure MoO_3. All the peaks in the XRD pattern of the reacted material can be indexed to MoO_3, one of the hydrogen bronzes, or Pt. We assume that the less protonated phase is the first to form and, therefore, corresponds to the <203> precipitates which originate at the Pt particles on Pt-supporting surfaces (as seen in Fig. 6a). The higher H content bronze is most likely present in the rough, optically distinct regions that were observed on surfaces reacted with excess Pt.

The rate of precipitation shows some dependence on the reaction temperature. For example at 25 ˚C, it may take several hours to approach precipitate densities realized on samples reacted at 130 ˚C for 30 min. When Pt-supporting or Pt-excess samples were reacted with dry CO or N_2, H_xMoO_3 precipitates were not observed with AFM, even after reactions in excess of three hours at 130 ˚C. With the exception of the presence of Pt particles, AFM images of these surfaces were indistinguishable from those of the fresh cleavage surface. XRD analysis of powdered Pt/MoO_3 samples which were reacted in dry CO for various times between 1 and 24 h at room temperature or 130 ˚C always

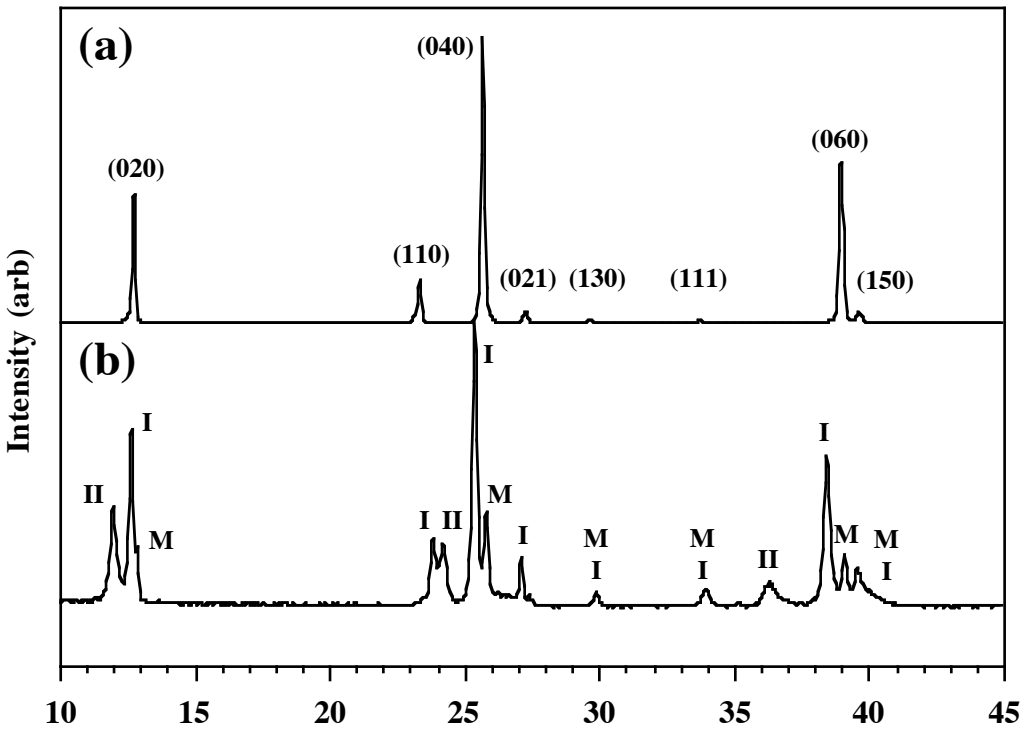

Figure 6.20 XRD patterns of pure MoO_3 (a) and a powdered Pt/MoO_3 mixture which was reacted with forming gas for 5 min at room temperature (b) All peaks in the XRD pattern can be associated with MoO_3 (M), $H_{0.34}MoO_3$ (I) or $H_{0.93}MoO_3$ (II) [28].

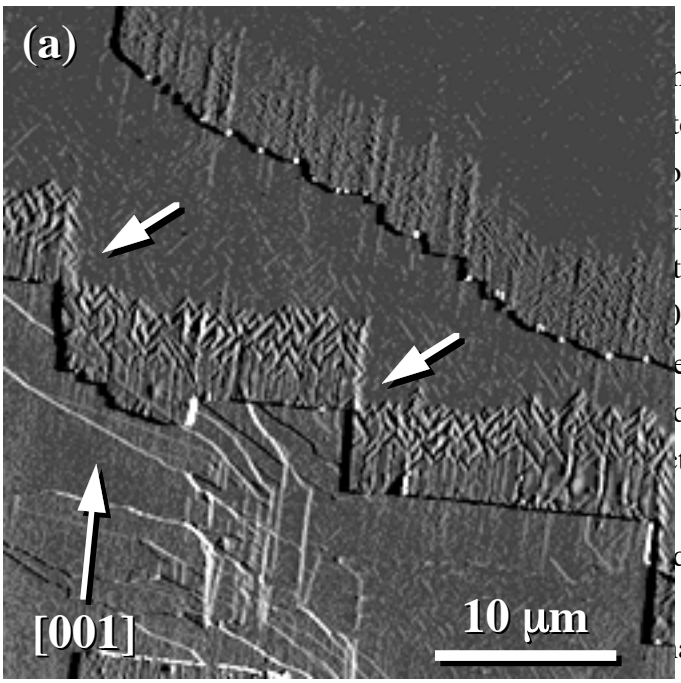

ne steps which populate the (010) tepped region which was reacted with of the <203> precipitates and <001> he depletion regions, arrowed in Fig. t. Their presence indicates that the 001> axis of the crystal. When tiny eacted along with the single crystal d they were visible with an optical tion at {001} facets was provided by

ds more quickly at step edges is not to the van der Waals gap between at the H reside in H_xMoO_3. The observation that H appears to enter at {001} facets and diffuse along <001> preferentially is surprising. Although <001> and <100> are not equivalent in the MoO_3 structure, there is no structural feature suggesting enhanced H diffusion along <001>. While the MoO_6 octahedra in each layer of the structure only share corners along <001>, as opposed to edges along <100>, it is anticipated that the H diffuse along sites between the layers, not within them. However, in the $H_{0.34}MoO_3$ structure, the protons are known to be associated with the bridging oxygen atoms where the MoO_6 octahedra share edges along <100> [32]. These oxygen atoms run along <001> and, perhaps, this is why diffusion is favored along this direction.

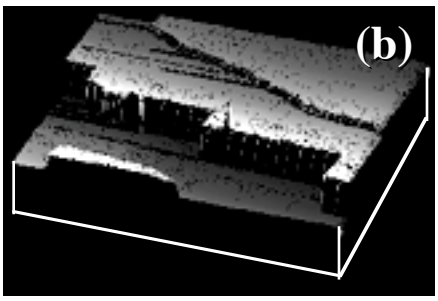

Figure 6.21 (a) AFM deflection image of a MoO_3(010) surface which was reacted for 30 min at 150 ˚C in atomic H. Note the high density of <203> precipitates and new <001> steps in the vicinity of native steps and the absence of these features in the regions where {001} and {100} bounded steps intersect (arrowed). (b) A three dimensional topograph of the same region illustrating the configuration of the native steps.

6.6 Discussion

Based on the evidence presented in sections 6.1 through 6.4, the <203> precipitates which form on the MoO_3(010) surface during reactions with alcohols are the hydrogen molybdenum bronze phase, H_xMoO_3, where $0.23 \leq x \leq 0.4$ [28,32,37]. The support for this assignment is based not only on observations during reactions with alcohols, but also on observations during H spill over reactions, where the relevant intercalation chemistry is already well established by earlier studies [26-30,32]. During H spill over, atomic H dissolves into MoO_3 after H_2 is dissociated by the Pt catalyst. When the MoO_3(010) surface was treated in environments from which atomic H was excluded (for example, N_2 or CO), the <203> precipitates were never observed. The results presented here show that during reactions with alcohols, H removed from the alcohol during the oxidation reaction also dissolves into MoO_3.

The observation that H_xMoO_3 forms as a by-product of reactions with alcohols is consistent with earlier XRD studies [7,8]. The habit and morphology of the observed H_xMoO_3 precipitates are identical to microstructural features called domains that have been observed during past TEM experiments [9-21,23]. The domains were first reported more than 50 years ago and have been described in different ways and with different indices. While some groups have also described the orientation as the <203> direction [15], which makes a 35.54° angle with <001>, Gai and coworkers [20,21,23] indexed the direction as <304>, which makes a 38.8 ° angle with <001>. However, regardless of this choice, a comparison of the micrographs in the references cited above makes it clear that the various groups observed the same two phase microstructure. The domains have been observed both during beam heating in the microscope's vacuum [9-15] and during *in situ* reduction in an environmental cell [16-18,20,21,23]. Selected area electron diffraction patterns indicate that the structure of the domains is similar to that of the MoO_3 matrix [14,15,20,23] and this observation has been interpreted previously in two different ways.

The first interpretation, provided by Bursill et al. [15], is that the domains are a hydrogen molybdenum bronze, H_xMoO_3, formed due to the incorporation of surface hydroxyl impurities during beam heating. In this case, phase identification was supported by convergent beam electron diffraction results which demonstrated that the domains exhibited the same space group and a and c lattice parameters as the hydrogen bronze $Mo_4O_{10}(OH)_2$ [31]. This oxide-hydroxide has more recently been formulated as H_xMoO_3, where $0.23 \leq x \leq 0.4$, and we prefer the latter of the two expressions [28]. Since the samples used in the current study were at the opposite extreme with respect to the surface-to-volume ratio, we do not expect the incorporation of surface hydroxyls to saturate the bulk and lead to precipitation of the bronze. This is consistent with our

observation that the <203> precipitates only form in conditions where H was available either from the spill over reaction or from the decomposition of an alcohol. In all other respects, our conclusions regarding the nature of the precipitates are consistent with those of Bursill et al. [15]. It should be noted that the tendency of MoO_3 to react with trace H impurities is well documented and supports this model. For example, in ultrahigh vacuum, with gaseous H_2 at pressures as low as 10^{-8} Torr, hydrogen molybdenum bronzes are formed when MoO_3 is placed in the vicinity of a hot W filament [30]. Without the filament, the reaction can still be catalyzed at this low pressure either by Pt or by the bronze itself [29,30]. In fact, there are a wide variety of conditions under which this phase is known to form [26-32].

The second interpretation, provided by Gai et al. [20,21,23], is that the domains are an oxygen deficient phase having an ordered arrangement of oxygen vacancies. This assignment was supported on the basis of selected area electron diffraction patterns. However, it had already been demonstrated by Bursill et al. [15] that these same patterns were entirely consistent with the presence of the hydrogen bronze phase. While the bronze was already well characterized at the time, the superlattice phase proposed by Gai et al. [20,21,23] has never been detected in any other study of the Mo-O system [33,34]. Furthermore, the current and previous XRD studies [7,8] show no evidence for the superlattice peaks expected from the proposed oxygen deficient phase. Gai et al. [21,23] provided two reasons for rejecting the idea that the domains were a protonated phase. The first was that the domains form in all environments, even CO/He mixtures where no source of H was thought to be present. However, this is not inconsistent with the model proposed by Bursill et al. [15]. If the bronze is actually formed due to the incorporation of surface hydroxyl impurities, then the source of H is from the sample itself and the environment is irrelevant. In fact, none of the TEM studies cite any conditions under which the domains do not form. This observation supports the idea that the formation mechanism is related to the high surface area sample itself and/or the inevitable electron irradiation that occurs during TEM observations. The second reason for rejecting the earlier assignment was the erroneous assumption that H_xMoO_3, where $0.23 \leq x \leq 0.4$, is not stable above 200°C [21]. In fact, the existing data indicate that this bronze is stable until at least 390 °C during vacuum heating [35]. We expect this stability range to be extended when the activity of H in the atmosphere is increased, as it is during the dissociative chemisorption of an alcohol. In summary, the observations described by Gai et al. [20,21,23] provide no evidence to contradict the conclusion that the <203> precipitates are H_xMoO_3.

In the present study, the well defined conditions under which the precipitates are observed combined with the XRD and IR signatures of H_xMoO_3 leave little doubt that the <203> precipitates which form during H spill over and reactions with alcohols are H_xMoO_3. Considering the wide variety of conditions under which this phase is known to form [26-32], its precipitation during reactions with alcohols is not too surprising. In fact, earlier XRD studies showed that the H-bronze formed after low temperature annealing in methanol [7,8] and the authors of an earlier report on the oxidation of methanol by MoO_3 speculated on the possibility of hydrogen bronze formation as the surface methoxy decomposes to yield formaldehyde [4]. Based on the new evidence presented here, it is interesting to reconsider the mechanism of alcohol oxidation on MoO_3.

When an alcohol molecule is oxidized by MoO_3, two hydrogens are removed. According to the accepted model (shown in Fig. 2.7), the first is removed during the initial dissociative chemisorption of the alcohol and the second is removed when the surface alkoxy decomposes to the aldehyde [4]. Both liberated protons are then thought to react with lattice O to form H_2O and a surface oxygen vacancy [2,3]. Under the experimental conditions detailed here, however, some portion of the liberated H intercalates into the MoO_3 lattice and H_xMoO_3 is formed. The H that reacts with MoO_3 might be formed during the dissociative chemisorption, the alkoxide decomposition, or both steps. Farneth et al. [4] suggested that bronze formation might explain the temperature lag between aldehyde desorption and H_2O desorption during TPD of MeOH and EtOH from MoO_3. However, this temperature lag is not observed during TPD of 2-PrOH and we still observe H_xMoO_3 precipitation during this reaction [3]. Machiels and Sleight [1] have studied MeOH oxidation in the absence of gas phase O_2, conditions identical to those studied here. Because the product distribution they observed included dimethyl ether, H_2, and methane, but not formaldehyde, we surmise that while the dissociative chemisorption of MeOH still occurs, the methoxy do not decompose to formaldehyde. Instead, they may combine (leading to dimethyl ether) or react with H from the bronze (leading to methane). This suggests that in the absence of O_2, the bronze must be formed during the dissociative chemisorption of the alcohol. However, we cannot rule out the possibility of protonation during both steps of the reaction. This modified reaction mechanism is presented in Fig. 6.22. The formation of a protonated phase implies that H can be removed from the alcohol without creation of an O vacancy, a process that might become more important at lower temperatures where vacancy generation is less probable.

There are a number of materials properties often associated with partial oxidation catalysts. For example, they must be able to easily form and transport stoichiometry compensating defects. Considering the fact that many of the molybdates and vanadates used as oxidation catalysts are able to form H-bronzes or at least dissolve some H [41], one could speculate that this also is an important, but previously unrecognized, property of useful partial oxidation catalysts.

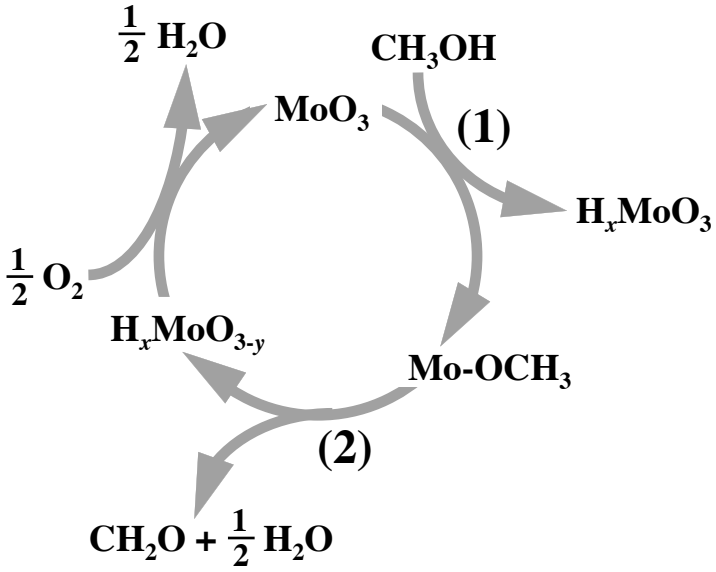

Figure 6.22 Modified mechanism of MeOH oxidation on MoO_3. During the dissociative chemisorption of MeOH, a surface methoxy species is formed and the liberated proton intercalates into the MoO_3 lattice to form H_xMoO_3. Upon decomposition of the methoxy group and formation of formaldehyde, a second proton is liberated and, here, we assume that it reacts with lattice oxygen to form water.

6.7 Summary and Conclusions

Atomic force microscopy and X-ray diffraction have been used to characterize the structural evolution of the MoO_3(010) surface during gas phase reactions with nitrogen-alcohol (methanol, ethanol, and 2-propanol) mixtures between 200 and 400 ˚C [42]. The results of this study demonstrate that MoO_3 intercalates H during these reactions ($T \geq 300$ °C) and that protonation leads to the precipitation of a well known hydrogen molybdenum bronze, H_xMoO_3, where $0.23 \leq x \leq 0.4$. The acicular precipitates of H_xMoO_3 form topotactically and are aligned along the <203> directions of the MoO_3(010) surface plane. Based on previously published product distributions under identical conditions, it can be concluded that the intercalating H is formed during the initial dissociative chemisorption of the alcohol. Identical H_xMoO_3 precipitates form

when MoO_3(010) surfaces are reacted with atomic H produced by spill over from supported Pt particles. While higher bronzes form during the course of the spill over reaction, H_xMoO_3 ($0.23 \leq x \leq 0.4$) is the only phase which has been detected during reactions with alcohols.

6.8 References

[1.] Machiels, C.J. and Sleight, A.W., *in* "Proceedings of the 4th International Conference on the Chemistry and Uses of Molybdenum" (H.F. Barry and P.C.H. Mitchell, Eds.), p. 411. Climax Molybdenum Co., Ann Arbor, MI, 1982.

[2.] Farneth, W.E., Ohuchi, F., Staley, R.H., Chowdhry, U., and Sleight, A.W., *J. Phys. Chem.* **89** (1985) 2493.

[3.] Farneth, W.E., Staley, R.H., and Sleight, A.W., *J. Am. Chem. Soc.* **108** (1986) 2327.

[4.] Farneth, W.E., McCarron III, E.M., Sleight, A.W., and Staley, R.H., *Langmuir* **3** (1987) 217.

[5.] Mars, R. and van Krevelen, D.W., *Chem. Eng. Sci.* **3** (1954) 41.

[6.] Haber, J., *in* "Solid State Chemistry in Catalysis" (R. Grasselli and J. Brazdil, Eds.), p. 1. American Chemical Society, Washington, D.C., 1985.

[7.] P. Vergnon and J.M. Tatibouet, *Bull. Soc. Chim. Fr.* **11-12** (1980) 455.

[8.] J. Guidot and J.E. Germain, *React. Kinet. Catal. Lett.*, **15** (1980) 389.

[9.] Heidenreich, R.D., and Sturkey, L., *J. Appl. Phys.* **16** (1945) 97.

[10.] Glemser, O. and Lutz, G., *Kolloid-Z.* **119** (1950) 99.

[11.] König, H., *Z. Physik.* **130** (1951) 483.

[12.] Hashimoto, H., *J. Phys. Soc. Japan* **9** (1954) 150.

[13.] Pernoux, E. and Borrelly, R., *J. Microscopie* **2** (1963) 407.

[14.] Bursill, L.A., *Proc. Roy. Soc.* **A311** (1969) 267.

[15.] Bursill, L.A., Dowell, W.C.T., Goodman, P., and Tate, N., *Acta Cryst.* **A34** (1974) 296.

[16.] Thöni, W. and Hirsch, P.B., *Phil. Mag.* **33** (1976) 639.

[17.] Thöni, W., Gai, P.L., and Hirsch, P.B., *Phil. Mag.* **35** (1977) 781.

[18.] Thöni, W., Gai, P., and Hirsch, P.B., *J. Less-Common Metals* **54** (1977) 263.

[19.] Bertrand, O. and Dufour, L.C., *Phys. Stat. Sol. A* **60** (1980) 507.

[20.] Gai, P.L., *Phil. Mag. A* **43** (1981) 841.

[21.] Gai, P.L. and Labun, P.A., *J. Catal.* **94** (1985) 79.

[22.] Hansen, S. and Andersson, A., *J. Solid State Chem.* **75** (1988) 225.

[23.] Gai-Boyes, P.L., *Catal. Rev.-Sci. Eng.* **34** (1992) 1.

[24.] Smith, R.L. and Rohrer, G.S., *J. Catal.* **163** (1996) 12.

[25.] Smith, R.L. and Rohrer, G.S., *J. Solid State Chem.* **124** (1996) 104.

[26.] Sermon, P.A. and Bond, G.C., *Catal. Rev.* **8** (1973) 211.

[27.] Sermon, P.A. and Bond, G.C., *J. Chem. Soc. Faraday I* **72** (1976) 730.

[28.] Birtill, J.J. and Dickens, P.G., *Mat. Res. Bul.* **13** (1978) 311.
[29.] Erre, R., van Damme, H., and Fripiat, J.J., *Surf. Science* **127** (1983) 48.
[30.] Erre, R., Legay, M.H., and Fripiat, J.J., *Surf. Science* **127** (1983) 69.
[31.] Glemser, O. and Lutz, G., *Z. Anorg. Allg. Chem.* **264** (1951) 17.
[32.] Jacobson, A.J., *in* "Solid State Chemistry Compounds" (A.K. Cheetham and P. Day, Eds.), p. 182. Clarendon Press, Oxford. 1992.
[33.] L. Kihlborg, *Ark. Kemi* **21** (1963) 471.
[34.] L.L.Y. Chang and B. Phillips, *J. Am. Ceram. Soc.* **52** (1969) 527.
[35.] N. Sotani, Y. Kawamoto, and M. Inui, *Mat. Res. Bull.* **18** (1983) 797.
[36.] N. Sotani, N. Yoshida, Y. Yoshioka, and S. Kishimoto, *Bull. Chem. Soc. Jpn.* **58** (1985) 1626.
[37.] P.G. Dickens, S.J. Hibble, and G.S. James, *Solid State Ionics* **20** (1986) 213.
[38.] T. Ohno, H. Miyata, F. Hatayama, and N. Sotani, *Bull. Chem. Soc. Jpn.* **60** (1987) 3435.
[39.] K. Eda, *J. Solid State Chem.* **83** (1989) 292.
[40.] L. Seguin, M. Figlarz, R. Cavagnat, J.-C. Lassègues, *Spectrochim. Acta A* **51** (1995) 1323.
[41.] Schöllhorn, R., *Angew. Chem. Int. Ed. Engl.* **19** (1980) 983.
[42.] R.L. Smith and G.S. Rohrer, *J. Catal.* **173** (1998) 219.

7

The Structure Sensitivity of Methanol Chemisorption on MoO_3

7.1 Introduction

The results presented in Chapter 6 demonstrated that MoO_3 intercalates H during reactions with MeOH and that protonation leads to the precipitation of H_xMoO_3 at the (010) surface. Because previous product distributions indicate that the surface methoxy do not decompose in the absence of oxygen, it was concluded that the intercalating H must be formed during the initial dissociative chemisorption of the alcohol. If this is the case, then the amount of H_xMoO_3 formed at the surface provides a quantifiable indicator of MeOH chemisorption. The objective of the experiments described in this chapter was to directly observe how undercoordinated Mo sites influence the rate of H_xMoO_3 precipitate formation and, therefore, MeOH chemisorption.

Because no primary Mo-O bonds are broken during the creation of an ideally planar MoO_3(010) surface, the only possible undercoordinated Mo atoms are adjacent to vacant O sites. All real surfaces contain some steps and the edges of these steps will have local bonding geometries similar to the lateral {h0l} facets. For example, creation of a (100) surface (or a step along the <001> direction) requires breaking one of the Mo-O bonds in each bridging Mo-O-Mo unit across the interface. For every Mo-O-Mo linkage broken, one Mo will be exposed in a five-coordinate site while the other will remain octahedrally coordinated. Therefore, the Mo on this surface have an average coordination number of 5.5. To create a (001) surface or a step along <100>, two Mo-O-Mo links must be broken and this leaves the exposed Mo with an average coordination number of 5. From this geometric point of view, the Mo atoms on a general {h0l} surface or <h0l> step have an average coordination number that must be between these two limits.

The concentration of undercoordinated surface Mo arising from oxygen vacancies is thermodynamically controlled and limited [1]. The V_O concentration increases with increasing temperature and/or diminishing partial pressure of oxygen. However, at a

fixed temperature, the maximum achievable oxygen vacancy concentration will be limited by the appearance of new defect structures (CS planes) or reduced phases. Definitive data concerning the equilibrium V_O concentration in MoO_3 are not available, however, previous estimates of $[V_O]$ in the 300 °C to 330 °C temperature range have been on the order of 10^{-4} [2]. If this is the case, and we take the concentration of surface Mo, on (010) to be 6.8 x $10^{14}/cm^2$, the maximum number of active sites due to V_O is 6.8 x $10^{10}/cm^2$. The concentration of undercoordinated Mo sites due to the presence of steps, on the other hand, is variable and depends on surface preparation. On a typical (010) growth surface, the density of single layer steps is on the order of 2 x 10^3/cm (cm/cm^2). Taking the density of Mo along such a step to be 2.7 x 10^7/cm, the density of active sites due to steps is 5 x $10^{10}/cm^2$. So, for a typical (010) facet at 330 °C, the concentrations of undercoordinated surface Mo sites arising from V_O and steps are comparable.

There is an important distinction between the active sites arising from oxygen vacancies and steps. While the concentration of undercoordinated surface Mo arising from V_O is fixed and limited, those arising from steps can be controlled. In Chapter 5, the conditions under which pits form and change shape on the MoO_3(010) surface were described [3,4]. Based on the geometric arguments presented above, these pits must be bounded by undercoordinated surface Mo and the density of such sites increases with the density and size of the pits. By determining the density and configuration of H_xMoO_3 precipitates which form on {010} surfaces with different populations of undercoordinated surface Mo sites during reactions with MeOH-N_2 mixtures at ~330 ˚C, we are able to quantify the influence that these sites have on the chemisorption of MeOH.

7.2 Experimental Procedure

7.2.1 Surface Reactions

Pits were introduced on the MoO_3(010) surface by reducing single crystal samples in a 250 cc/min flow of as-received forming gas (10%H_2-N_2 with ~20 ppm H_2O) at 400˚C. Crystals were reduced in a silica boat with a small piece of Ta foil (1 mm x 10 mm x 0.1 mm) which acts as an O getter. Voids formed by this reducing treatment are elongated along the <101> direction. Reoxidation treatments were carried out in the same reactor, with the ends of the tube open to the ambient atmosphere, to enlarge and/or reorient the bounding edges of the pits. The reactions with MeOH-N_2 mixtures were carried out between 300 and 330˚C in a 150 cc/min flow of gas at atmospheric pressure. The N_2 carrier gas was dried by passing it through a column of

$CaSO_4$ (Drierite) and then saturated with MeOH (99.9%, Aldrich) in a bubbler at 0 ˚C or room temperature (25 ± 1 ˚C). Following reaction, the samples were transferred to the cold zone and cooled to room temperature under a flow of MeOH-N_2. No special precautions were taken to prevent exposure of the samples to the ambient between pit formation and reaction with MeOH.

7.2.2 AFM Image Analysis

To quantify the amount of H_xMoO_3 formed during any given reaction, the total volume of the phase formed in a given surface area was estimated. For example, the AFM image in Fig. 7.1a shows a typical precipitate and its lateral dimensions. The precipitate's shape is idealized as a diamond elongated along <203> whose area in the (010) plane is the product of its length (l) and width (w), as illustrated in Fig. 7.1 and 7.2. The thickness of the particle is estimated based on the measured surface relief (h) and X-ray diffraction data which shows that the b axis of the precipitate phase is 0.2 Å larger than that of the matrix phase. Assuming that all the strain between the precipitate and the matrix is relieved at the free surface, then the number of unit cells transformed is the measured height (in Å) divided by 0.2 Å. This number, multiplied by the b lattice parameter of the precipitate (14.05 Å), gives the particle thickness, t (see Section 6.2.3) [5]. The volume of any given particle is then calculated as the product of its length, width, and thickness. The volume of H_xMoO_3 per unit surface area is calculated by summing the volumes of all of the particles in an image and dividing by the observed area.

As a final note, the finite size of the AFM tip leads to a systematic overestimation of the particle volume. Considering that the features described here are much wider than they are high, this overestimation is negligible for most of the precipitates. However, for those with dimensions less than 100 nm, the details of the tip shape can become significant. No attempt has been made to correct for this effect, however, for any two surfaces where quantitative numerical comparisons are made, the observations were recorded with the same probe. Therefore, the magnitude and sign of the error is the same in both cases. There is an additional error in the magnitude of the measured volumes that derives from the simplified view of the particle's shape. However, since the sign of the error should always be the same, it affects only the absolute values of the volumes and not the outcome of our comparisons.

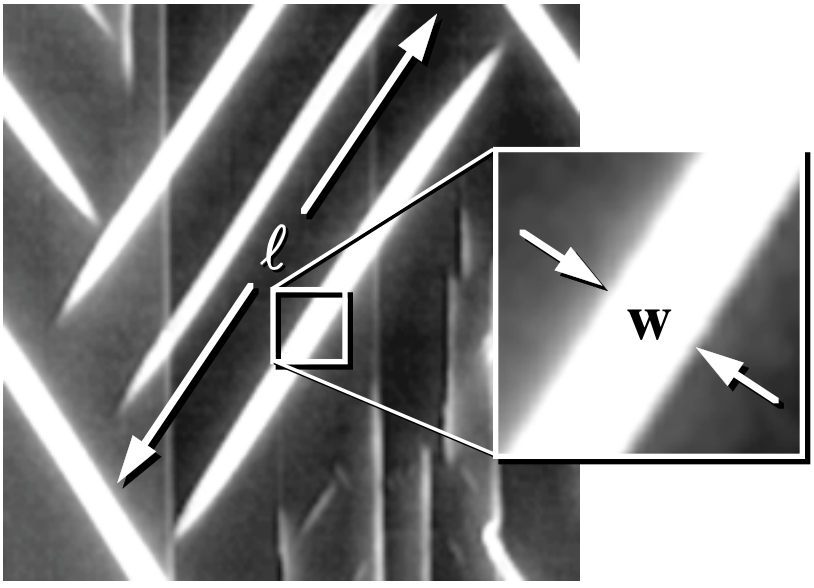

Figure 7.1 Lateral dimensions (l and w) of the H_xMoO_3 precipitates formed at the $MoO_3(010)$ surface during reactions with MeOH.

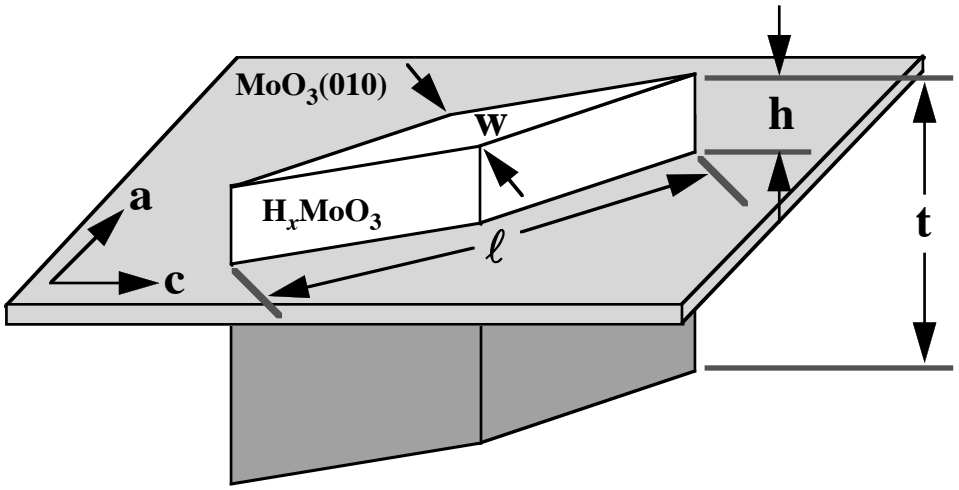

Figure 7.2 Schematic representation of the idealized, diamond shaped H_xMoO_3 precipitates.

7.3 Results

7.3.1 H_xMoO_3 Formation on Pitted Surfaces

The objective of this study was to compare the amounts of H_xMoO_3 formed on surfaces that were identical in every respect except for the density of undercoordinated surface Mo. To prepare pairs of surfaces that were identical in the step configuration, impurity concentration, and extended defect population, single crystals were cleaved to produce two mated surfaces that were mirror images. To test the reliability of this procedure, two halves of the same crystal were reacted with MeOH saturated N_2 at the same time. The size and density of the H_xMoO_3 precipitates in mirrored areas of these surfaces was identical. In fact, when any two fresh crystals were treated in the reactor at the same time, the H_xMoO_3 precipitate densities in the center of the (010) facet were comparable. In the experiments described in this section, the reactions with MeOH were always carried out on two halves of the same crystal. However, pits were introduced differently on the two halves so that they had different populations of undercoordinated surface Mo.

When MoO_3 samples are reduced in 10%H_2-N_2 at 400 ˚C and then reacted in MeOH-N_2 at 330 ˚C, the (010) surface is modified in much the same way that the freshly cleaved surface is modified; acicular precipitates of H_xMoO_3 nucleate along <203>. However, the precipitation reaction is favored at the pits introduced during the treatment in 10%H_2-N_2. After 2 min at 330 ˚C in N_2 saturated with MeOH at 0 ˚C, H_xMoO_3 precipitates are only found in the vicinity of pits. In the image in Fig. 7.3, an H_xMoO_3 precipitate can be seen emerging from the pit labeled with a "p". Additional defects with a distinct <001> character also form near the voids. These features are similar to defects observed at higher temperatures (400 ˚C) during reactions with MeOH (see Chapter 6 or [5]) and they are distinguished from the surface/CS plane intersections because the height over the defects is greater than that observed over the CS planes (2 Å). In most cases, these features coincide with a CS plane, but they are only as long as the width (along <001>) of the pit to which they are adjacent. If one follows a CS plane along <001>, the height over the defect is only 2 Å, but adjacent to voids the height may be increased to more than 10 Å. This swelling is not seen on surfaces which have only been reduced in 10%H_2-N_2. The feature arrowed in Fig. 7.3 shows both <001> and <203> character.

The preferential nucleation of H_xMoO_3 in the vicinity of the pits becomes more apparent with longer reaction times. The image in Fig. 7.4 shows a surface that was first reduced in forming gas for 4 min at 400 °C to introduce pits, and then reacted at 300 °C

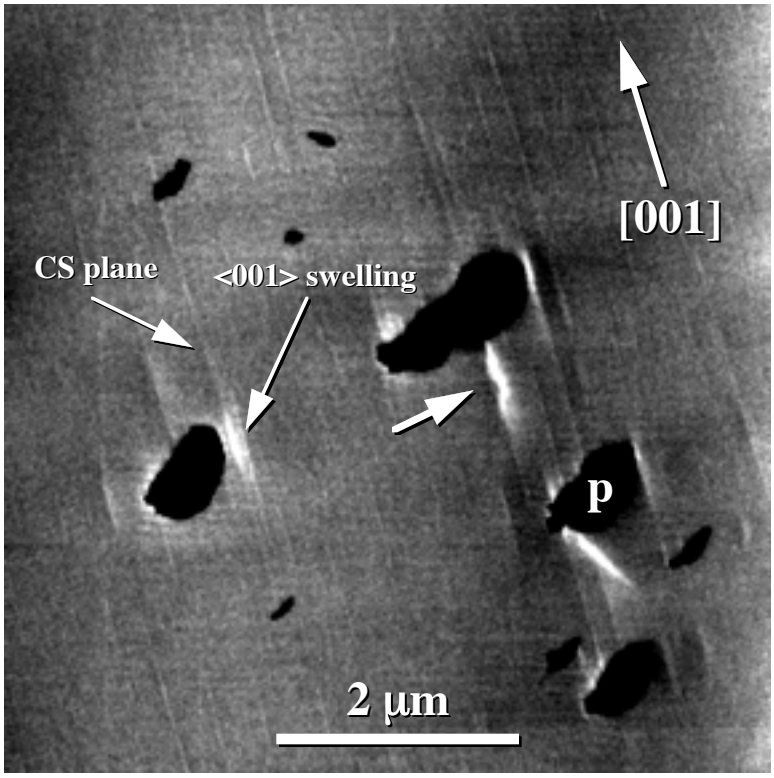

Figure 7.3 AFM topograph of a MoO_3(010) surface which was first reduced for 8 min at 400 ˚C in 10%H_2-N_2 and then reacted for 2 min at 330 ˚C in N_2 saturated with MeOH at 0 ˚C. The black-to-white contrast in the image is 20 Å.

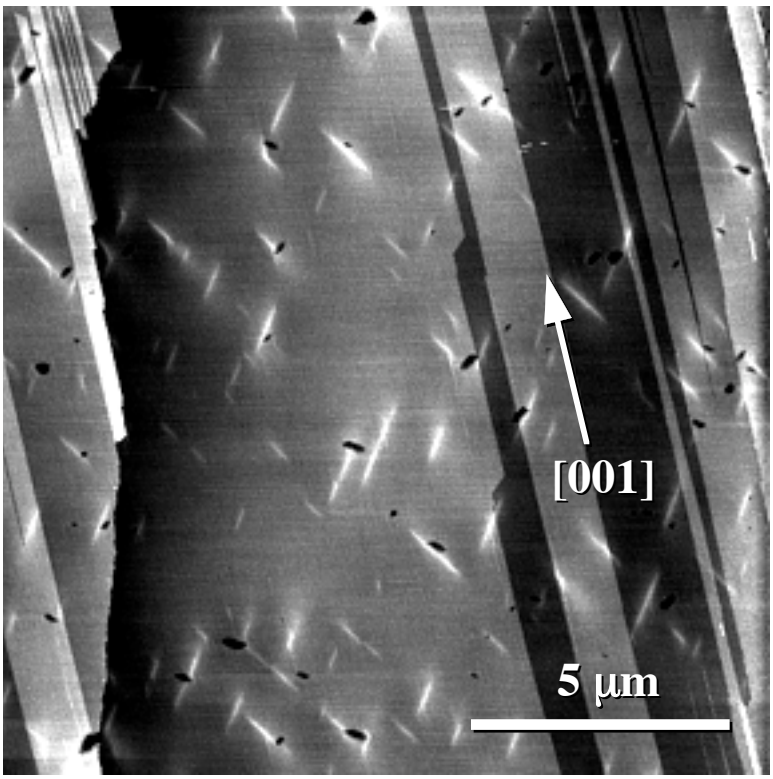

Figure 7.4 AFM topograph of a MoO_3(010) surface which was first reduced for 4 min at 400 ˚C in 10%H_2-N_2 and then reacted for 15 min at 300 ˚C in N_2 saturated with MeOH at 0 ˚C. The largest H_xMoO_3 precipitates are localized at the pits introduced during reduction. The black-to-white contrast in the image is 40 Å.

for 15 min in N_2 saturated with MeOH at 0˚C. The H_xMoO_3 precipitates on this surface are clustered around the surface pits introduced during reduction. In most cases, the largest precipitates intersect a pit or are very near a pit while the pit free areas have few or very small precipitates. The other half of this crystal was not reduced in forming gas. Although it was reacted with MeOH alongside the pitted crystal, no H_xMoO_3 was detected in mirrored areas on the cleavage surface.

With longer reaction times, very large H_xMoO_3 precipitates grow from the pits and extend into the MoO_3 matrix. The image in Fig. 7.5a shows a surface that was reduced for 10 min at 400 ˚C in forming gas, reoxidized for 2 h at 400˚C in the ambient, and, finally, reacted for 20 min at 330 ˚C in N_2 saturated with MeOH at 0 ˚C. The enhanced formation of H_xMoO_3 at the pit edges is obvious. Although smaller precipitates can also be found on the surface, the largest precipitates always originate at a pit. The other half of this crystal was not reduced in forming gas, but it was annealed in air and MeOH alongside the pitted crystal. A mirrored area of this surface is shown in Fig. 7.5b. On this flat surface, the precipitates are more numerous, but much smaller. The average height of the precipitates on the pitted surface is 43 Å while the average height on the flat surface is only 6 Å. The volume of H_xMoO_3 per surface area is 1×10^{-6} cm on the pitted surface and 1×10^{-7} cm on the flat surface. Thus, the surface with pits intercalated 10 times more hydrogen than the flat surface.

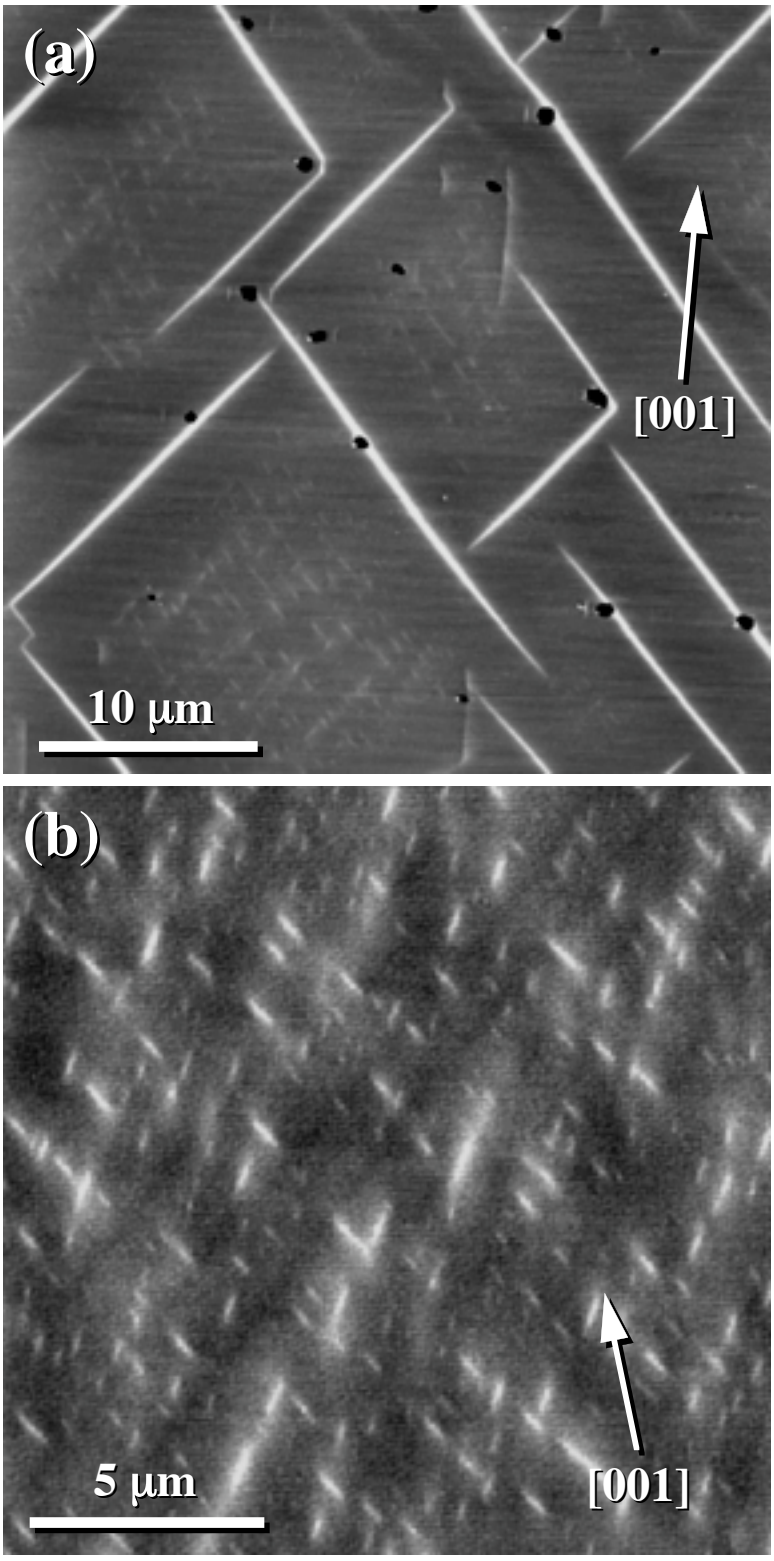

Figure 7.5 AFM topographs of mirrored areas of pitted (a) and flat (b) MoO_3(010) surfaces reacted for 20 min at 330 ˚C in N_2 saturated with MeOH at 0 ˚C. The pitted surface was reduced for 10 min at 400˚C in forming gas and then oxidized for 2 hr at 400˚C in the ambient prior to the MeOH reaction. The volume of H_xMoO_3 per surface area is 10^{-6} cm on the pitted surface and 10^{-7} cm on the flat surface. Note that the area in (a) is four times larger than the area in (b). The black-to-white contrast in (a) and (b) is 100 and 20 Å, respectively.

A similar effect is observed on surfaces oxidized for times sufficient to produce large rectangular pits. For example, the image in Fig. 7.6 is of a surface that was reduced in forming gas at 400 ˚C for 10 min and then oxidized for 3 h at 410 ˚C in the ambient. Finally, it was exposed to N_2 saturated with MeOH at 25 ˚C for 15 min at 330 ˚C. While most of the surface is covered with small H_xMoO_3 precipitates, large ones grow from the pit edges and extend into the matrix.

With the oxidation treatments, we can exercise some control over the size and shape of the pits. For example, two halves of the same crystal were reduced for 5 min at 400 ˚C in forming gas. One half was then oxidized in ambient air at 410 ˚C for 1 h. Both surfaces were then reacted for 10 min at 330 ˚C in N_2 saturated with MeOH at 25 ˚C. Characteristic AFM images from the same regions of the two surfaces are shown in Fig. 7.7. The pits in Fig. 7.7a are all less than 200 Å deep. On the other hand, the pits on the surface that received the oxidation treatment (Fig 7.7b) are all deeper than 500 Å. The H_xMoO_3 precipitates on the surface with the larger pits are larger and more numerous than those on the surface with shallower pits. Furthermore, the calculated volumes of H_xMoO_3 per area on the surfaces with shallow and deep pits are 5×10^{-7} cm and 2×10^{-6} cm, respectively. Finally, note that with extended MeOH reactions and high pit densities, the preferential nucleation at particular voids is less pronounced. The same effect is also observed on {010} surfaces with a large population of

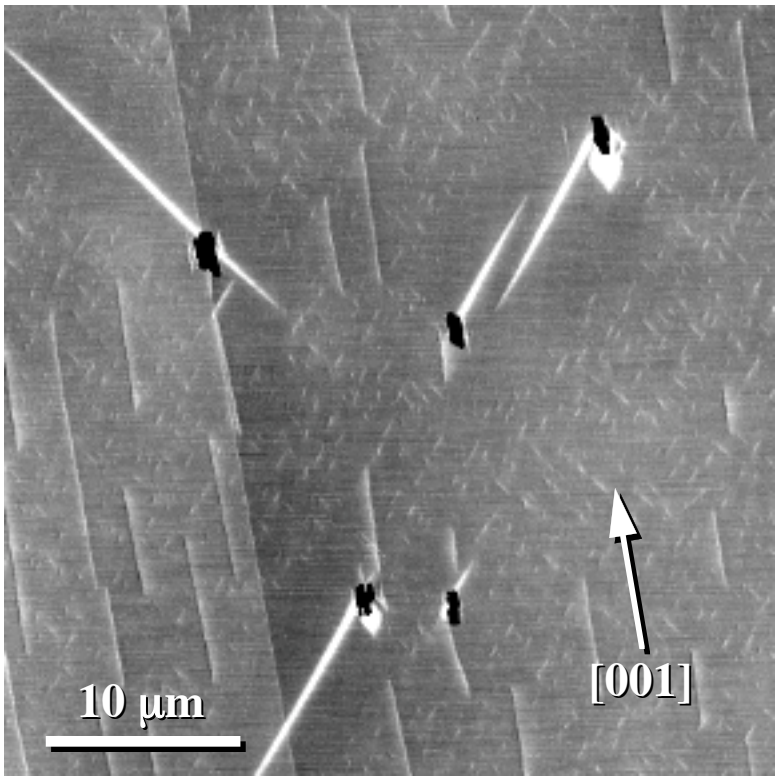

Figure 7.6 AFM topograph of a MoO_3(010) surface that was, first, reduced in forming gas at 400˚C for 10 min, oxidized for 3 hr at 410˚C in air, and, finally, exposed to N_2 saturated with MeOH at 25˚C for 15 min at 330 ˚C. The black-to-white contrast in the image is 100 Å.

oxidized, rectangular pits.

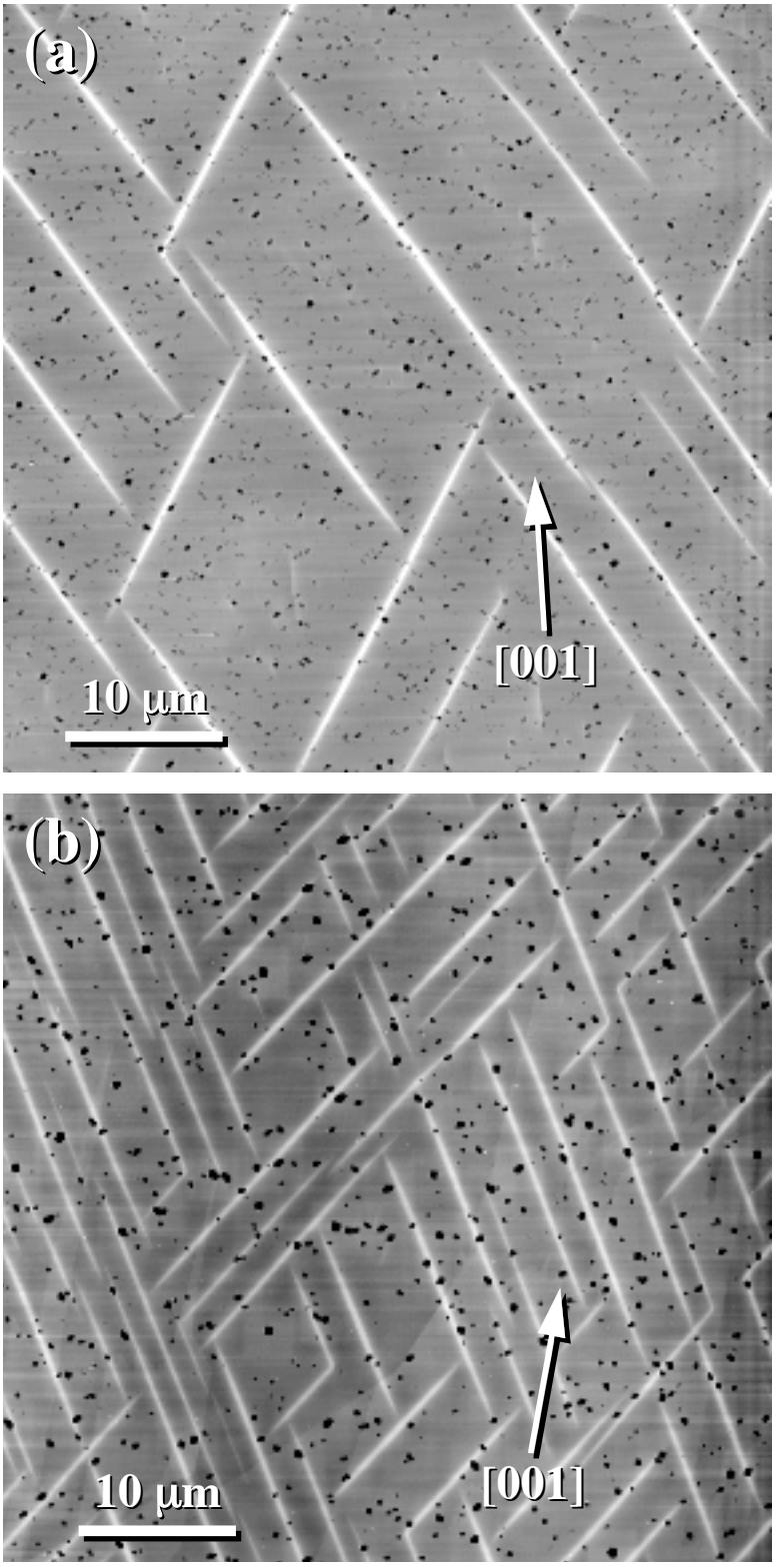

Figure 7.7 AFM topographs illustrating the effect of void size on H_xMoO_3 precipitation during a 10 min reaction at 330 ˚C with N_2 saturated with MeOH at 25 ˚C. Both surfaces were initially reduced for 5 min at 400˚C in forming gas. The surface in (b) was then oxidized in the ambient for 1 hr at 410˚C. The pits in (a) are less than 200 Å deep while those in (b) are greater than 500 Å deep. The calculated volumes of H_xMoO_3 per surface area are $5x10^{-7}$ cm (a) and $2x10^{-6}$ cm (b). The black-to-white contrast in (a) is 200 Å while that in (b) is 400 Å.

7.3.2 The Effect of Native Lateral Facets

Steps and pits on the (010) surface introduce out of plane components where the local bonding geometry should be similar to that found on the lateral facets. Indeed, when regions of the (010) surface near the lateral facets are examined, it is clear that the rate of H_xMoO_3 formation is enhanced. However, a number of qualifying statements should be made. First, the enhanced reaction at the crystal edges is observed only in the 100 μm thick region closest to the edge. The central regions have a uniform, homogeneous precipitate density that is unaffected by the proximity to the edges. So, while hydrogen is preferentially intercalated at the edges of the crystal, it also enters through the (010) surface, but at a slower rate. All of the images presented here were recorded in the central region of crystals with lateral dimensions greater than 1 mm and were not subject to edge effects.

In Chapter 6, it was shown that with extended reaction times (t > 30 min) at 330 °C, H_xMoO_3 adopted a second precipitate morphology (see Fig. 6.7). These swollen surface regions along <001> nucleate at {001} facets and grow until they extend several mm into the crystal. The surface relief over these features can be as high as 500 Å. The nucleation of these features can also be observed at large steps occasionally created by the cleavage process (see Fig. 7.8). Although large cleavage steps (height > 200 Å) behave as lateral facets, enhanced reactivity is not obvious at steps that are only a few

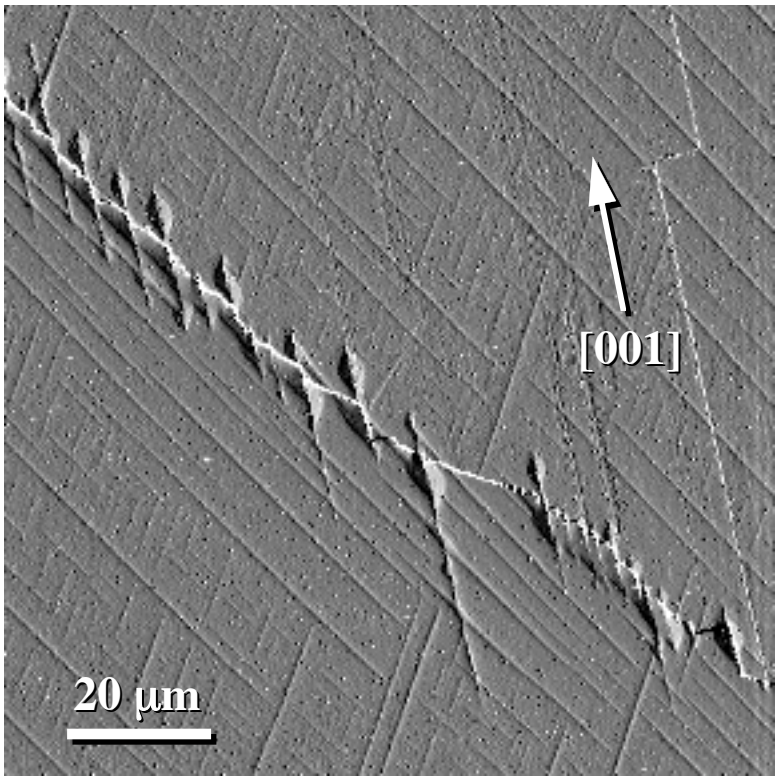

Figure 7.8 Preferential formation of the <001> habit of H_xMoO_3 at a large cleavage step on the MoO_3(010) surface during reactions with MeOH-N_2 at 300 °C. In this deflection image, the step edge is the white line of contrast which extends diagonally (left to right) across the image. The terrace to the left of the step edge is topographically higher than the terrace to the right.

unit cells in height.

7.4 Discussion

The results presented above demonstrate that two halves of the same crystal, reacted together under the same conditions, intercalate different amounts of hydrogen if they have different surface morphologies. We can be certain that the mated sample surfaces used for the comparisons were indistinguishable in the macroscopic structure of the basal plane, the impurity concentration, and the dislocation density. However, the procedures used to modify the surface topography and density of {h0l} sites also alter the absolute surface area of the basal plane and the stoichiometry of the sample. The magnitude of these changes and the potential effect that they might have on the formation of the intercalated phase are discussed below.

The changes in the absolute surface area can be estimated based on the AFM data. For example, the images in Fig. 7.5 show that the total volume of the bronze formed on the pitted surface is 10 times larger than that which is formed on the ideally flat surface. The basal component of the area in Fig. 7.5a is 1.6×10^{-9} m^2. With AFM data, the additional surface area contributed by the 17 pits in this area of the surface was approximated. Assuming that the pits are idealized right cylinders, the total {h0l} surface area is only 4×10^{-12} m^2, about 0.3 % of the total surface area. Based on these numbers, we conclude that the order of magnitude increase in the amount of hydrogen intercalated by the pitted surface is not simply due to the increase in the surface area, but to the local structure of the new surfaces.

By using mated halves of the same crystal and characterizing the size and density of the pits formed on these surfaces, we have established experimental control over the density of undercoordinated Mo contributed by {h0l} type facets. However, additional undercoordinated Mo are found next to vacant oxygen sites and this source is controlled by the temperature and partial pressure of oxygen in the reactor. Under the assumption that the surface plane responds to environmental changes rapidly, both halves of the crystal should have equal concentrations of surface oxygen vacancies during the final side-by-side reactions in MeOH. It might be argued, however, that if bulk oxygen diffusion determines the surface vacancy concentration, then surfaces reduced in forming gas to create pits are relatively enriched with surface oxygen vacancies and undercoordinated Mo with respect to the flat surface. When we consider the observations discussed in the last section, we conclude that this can not be the case.

Consider, for example, the results depicted in Fig. 7.7. Both samples were initially reduced in forming gas to generate identical pit distributions. At this stage, the defect structure of the two samples should have been identical. One sample was then

annealed in air to enlarge the surface pits. While this sample should be relatively depleted of oxygen vacancies, it intercalated four times more hydrogen than the reduced sample. Therefore, existing oxygen vacancies in either sample apparently play a subordinate role to the undercoordinated sites on the {h0l} surfaces.

With this observation in mind, it is interesting to estimate the possible ranges for the surface oxygen vacancy concentration. If we assume that the undercoordinated sites introduced by oxygen vacancies and step edges have the same activity, we can use the measured site density on pitted surfaces to place an upper limit on the vacancy concentration. For example, consider the surfaces in Fig. 7.5. The introduction of pits on one surface (Fig. 7.5a) leads to the creation of $4x10^{-12}$ m^2 of new surface area and the exposure of approximately 2.7×10^7 new Mo sites, assuming that there are 6.8×10^{18} Mo/m^2. On a basal surface of the same area, there are 8.3×10^9 Mo sites and 3 O sites for each Mo. If we introduce 2.7×10^7 new Mo sites by creating this many oxygen vacancies, the V_O concentration is 1×10^{-3}. Therefore, if we assume that the pitted and oxygen deficient (010) surfaces are identical in all other respects, then the vacancy concentration on the surface in Fig. 7.5b must be less than 10^{-3}. Clearly, the concentration of undercoordinated surface Mo sites associated with the edges of the pits dominates the surface vacancy concentration for all reasonable native defect concentrations.

The observation that hydrogen intercalation is enhanced by the relatively deep pits, large surface steps, and the lateral edges of the crystal, but not by single layer surface steps can be used to place a lower limit on the vacancy concentration. Based on images of cleavage surfaces, we estimate that the typical density of undercoordinated Mo associated with small steps is $10^{10}/cm^2$. The equivalent concentration of undercoordinated basal plane sites can be created using a vacancy concentration of 1×10^{-5}. Since H_xMoO_3 is not observed to nucleate preferentially on the small step edges of a cleavage surface, we conclude that the vacancy concentration is greater than 10^{-5}. It is interesting to note that the oxygen vacancy concentration estimated by researchers in the past is 10^{-4} and this figure falls between the limits we predict [2].

The results presented here lead to essentially the same conclusion reached by Farneth and coworkers on the basis of temperature programmed desorption studies in vacuum [6,7]. On the other hand, Tatibouët and Germain's [8] study of catalyst particles with different morphologies in atmospheric pressure reactor studies indicated that the basal planes were responsible for formaldehyde formation while the edge facets were responsible for the formation of higher order products such as dimethyl ether and dimethoxy methane. It might be possible to reconcile these observations by assuming

that the lateral facets provide sites for dissociative chemisorption and formation of the H_xMoO_3, but that decomposition of the methoxy, which is rate limiting, requires the presence of the basal surface. If it is true that both types of surfaces are required for a selective reaction, then the basal facet alone would be inert, as reported by Farneth and coworkers [6,7], while increasing the relative basal plane surface area in the presence of some lateral facets would enhance the concentration of products from the rate limiting step, as reported by Tatibouët and Germain.

7.5 Summary and Conclusions

The structure sensitivity of MeOH chemisorption at ~ 330 ˚C has been examined by characterizing the density and configuration of H_xMoO_3 precipitates that form during reactions between MeOH-N_2 and MoO_3(010) surfaces with different morphologies. Based on the AFM observations presented in this chapter, we can say that as the density of {h0l} surfaces increases, more hydrogen is intercalated into MoO_3 during reactions with MeOH-N_2 mixtures at $300 \leq T \leq 330$ ˚C. The observed increase is greater than can be explained by differences in the absolute surface area or the potential differences in the surface vacancy concentration. This result, taken together with the observation that H_xMoO_3 precipitates emerge from intentionally introduced and native nonbasal surfaces, leads us to conclude that the chemisorption properties of the {h0l} planes are much different than the {010} planes. These results are consistent with the idea that the active sites for dissociative chemisorption are the undercoordinated Mo that must exist on the {h0l} facets [6,7].

7.6 References

[illegible]

[illegible]

[illegible]

[illegible]

[illegible]

[illegible]

[6.] W.E. Farneth, F. Ohuchi, R.H. Staley, U. Chowdhry, and A.W. Sleight, *J. Phys. Chem.* **89** (1985) 2493.

[7.] W.E. Farneth, R.H. Staley, R.H., and A.W. Sleight, *J. Am. Chem. Soc.* **108** (1986) 2327.

[8.] J.M. Tatibouët and J.E. Germain, *J. Catal.* **72** (1981) 375.

8

The Morphological Evolution of the MoO_3(010) Surface during the Partial Oxidation of Methanol

8.1 Introduction

The influence of molybdenum trioxide's surface structure on its reactivity during the partial oxidation of methanol (MeOH) is the subject of debate. While it is believed that the active sites for MeOH chemisorption and oxidation are undercoordinated surface Mo sites, there is disagreement concerning the crystallography and chemical nature of these sites. It was first proposed by Tatibouët and Germain [1] that the basal {010} facets of MoO_3 were responsible for formaldehyde formation while the {h0l} (lateral) facets were responsible for the formation of higher order products. However, the results of temperature programmed desorption (TPD) spectroscopy studies by Farneth and coworkers [4,5] later led to the conclusion that the basal surfaces play a subordinate role in the reaction and that the lateral facets are responsible for the formation of all products. The anisotropic atomic structure of MoO_3 provides support for this conclusion. If free surfaces are created by breaking the smallest number of bonds, the Mo atoms on the {010} surfaces remain fully coordinated while those on lateral facets will have reduced coordination and unsaturated bonds. The results presented in Chapter 7 also support the idea that lateral facets are more active for MeOH chemisorption than {010}.

The basis of previous structural arguments have rested on a knowledge of the gross shape of MoO_3 catalyst particles, the apparent crystallographic distribution of the catalyst's surface area, and the expected termination of the crystallographically distinct MoO_3 facets. While this information is valuable, little is known about the morphology and structure of the individual facets of the MoO_3 catalyst particles. Furthermore, the surface morphology of the catalyst is expected to change during reactions, as stoichiometry compensating defects are continuously created and annihilated.

In this chapter, atomic force microscopy was used to characterize the evolution of the MoO_3(010) surface during reactions with air-N_2-MeOH mixtures between 200 ˚C and 300 ˚C. In addition to {010} cleavage surfaces, the structure and evolution of the {010}

growth surfaces of crystallites grown by sublimation were examined. This preparatory technique has been used previously to produce coarse MoO_3 catalyst samples for the oxidation of MeOH and other organics [1,11]. The results presented here demonstrate that the detailed morphology of the (010) surface changes during the reaction as a result of the continuous nucleation and growth of closed step loops bounded by undercoordinated surface Mo sites. The exact density and crystallographic orientation of these sites depends on the composition of the reactor feed.

8.2 Experimental

8.2.1 Surface Reactions

Prior to reaction, CVT grown samples were cleaved with a razor blade (in the ambient) normal to <010> along <100> to produce a fresh (010) surface. The samples were then placed in a silica boat (attached to the magnetic transfer rod) and loaded into the cool zone of the reaction tube under a flow of an air-N_2-MeOH mixture. While the samples were typically loaded immediately after cleavage, exposing them to the ambient for up to one week did not appear to affect the experimental observations. Crystals grown by sublimation were not cleaved prior to reaction. They were simply loaded into the boat in an as-grown state. The mixtures of dry air (Matheson) and N_2 (prepurified, Matheson) were passed through a column of $CaSO_4$ (Drierite) prior to saturating them in a MeOH (99.9+%, Aldrich) bubbler maintained at 0 ˚C or room temperature (25±1˚C). The air:N_2 mixtures used in these experiments ranged from 100:0 to 2:98 (by volume). All of the surface reactions were performed at atmospheric pressure in a 200 cc/min flow of the feed gas. Additional experiments were also conducted with air-N_2 mixtures which were either dried, untreated, or saturated with water at room temperature.

8.2.2 AFM Analysis

After reaction, the samples were momentarily exposed to the ambient before being transferred to the glove box where AFM measurements were performed. During the analysis period (several hours), changes in surface structure were not observed and at the detection level afforded by AFM, the surfaces were stable indefinitely at room temperature in the glove box or the ambient.

The step edge density in the AFM images was estimated with the aid of the image analysis software, Image SXM, which is a sub-version of the public domain analysis program, NIH Image. The step edges in each image were first isolated by applying an edge detection filter. A binary contrast threshold was then applied to the edge enhanced

image so that the edges were black and all other areas were white. By determining the fraction of black pixels in the binary image, one can estimate the total step edge length per unit area. All of the linear step densities cited in this paper are in units of the length of a half unit (6.93 Å) step per unit area of the (010) surface. Considering the atomic structure of orthorhombic MoO_3 and assuming that steps are formed by breaking the fewest number of bonds [13], we can obtain the approximate area density of unsaturated surface Mo sites by multiplying by a factor of 2.5 x 10^7 Mo/cm. However, since the quantity actually measured in these experiments is the linear density of half unit step edges, only this number is referred to in the discussion of the results.

8.2.3 Gravimetric Measurements

Parallel experiments were conducted on powdered MoO_3 samples to assess any mass changes that might occur during the reactions. Prior to use, the MoO_3 powder was calcined in air at 400 ˚C for 24 h and then gently ground in an alumina mortar to break up any powder aggregates. Approximately 0.0350 g of the powder was loaded into a small, dry, porcelain boat which was weighed just before (mass = 0.8670 g) and after loading. The loaded boat was then placed into the quartz reaction tube where it was subjected to a 100 cc/min flow of an air-N_2-MeOH or air-N_2-H_2O mixture at 300 ˚C for 10 to 48 h. The MeOH or H_2O was introduced by passing the air-N_2 mixture through a bubbler at room temperature. At the conclusion of the treatment, the boat was removed from the reaction tube and weighed. As a check, the boat was cleaned, dried, and reweighed at the conclusion of each experiment to ensure that its mass had not changed by more than ± 0.0002 g during the course of the experiment.

8.3 Results

8.3.1 The Structure of the MoO_3(010) Surface

The morphology of the MoO_3(010) surface depends on the method of preparation. The fresh cleaved surfaces of CVT grown samples are composed of atomically flat terraces separated by steps which have heights that are an integer multiple of ~7 Å (see Fig. 4.1). This characteristic height is half the unit cell repeat length along <010> and corresponds to the distance between the van der Waals gaps which separate the adjacent layers of the structure (6.93 Å). We refer to these features as "half unit" steps. The steps on the cleavage surface are characteristically oriented along <001> and frequently extend unperturbed for distances greater than 100 μm. The distance between the steps is inhomogeneous and can be as small as a few microns or larger than 100 μm.

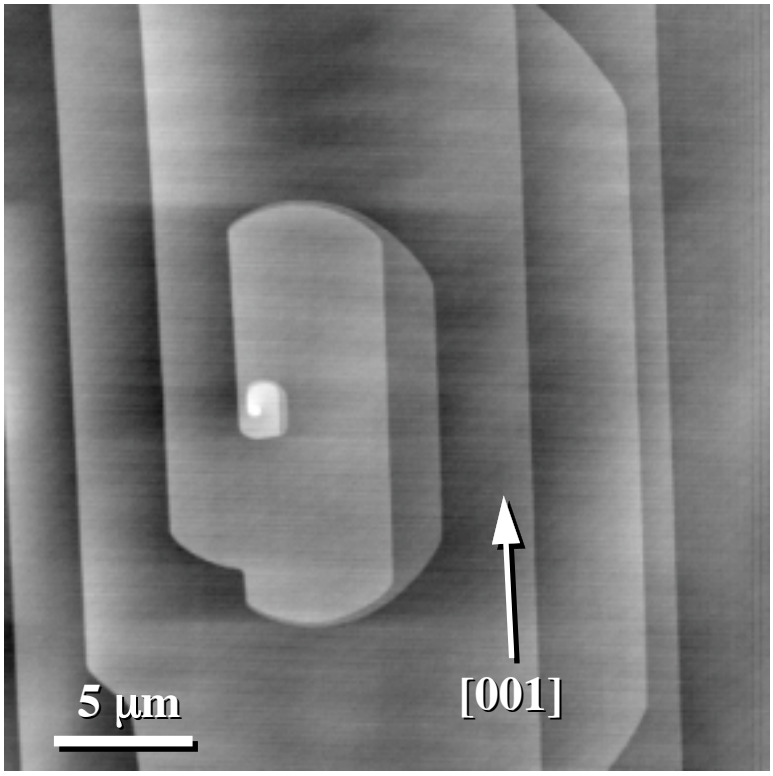

Figure 8.1. AFM topograph of a screw dislocation intersecting the (010) growth surface of a MoO_3 crystal grown by sublimation in the ambient. The black-to-white contrast in the image is approximately 50 Å. The calculated step edge density is 2.58 x 10^3/cm. On growth surfaces, the step edge density may vary between 0 and 2 x 10^3/cm over .01 mm^2.

The morphology of the growth surfaces of the sublimed crystals is governed by the configuration of screw dislocations which act as step sources and facilitate growth (see Fig. 8.1). Surfaces formed by this mechanism differ from the cleavage surfaces in two characteristic ways. First, the most frequently encountered steps are integer multiples of the b lattice parameter (~14 Å) rather than b/2. This is because only screw dislocations with Burgers vectors equal to an integer multiple of the lattice repeat distance are able to spiral and create new crystal without introducing stacking faults. The second difference is that in addition to the steps along <001>, other orientations are frequently observed. This is a natural consequence of growth by the screw dislocation mechanism which leads to significant populations of spiral steps.

8.3.2 Surface Structure of MoO_3(010) during the Partial Oxidation of MeOH

When MoO_3(010) surfaces are reacted with air-N_2-MeOH mixtures at 300 ˚C, loops of steps surrounding shallow pits nucleate on the previously flat terraces of the surface. For example, the cleavage surface in Fig. 8.2a was reacted for 2 h at 300 ˚C in air saturated with MeOH at room temperature. While the lateral dimensions of the pits (darker contrast) can be as large as several microns, they are always bounded by half unit steps and are therefore only 7 Å deep. The size of the pits varies from trial to trial but, when all the observations are considered together, it appears that they nucleate as small

pits (see Fig. 8.2a), grow larger, and, eventually, coalesce (Fig. 8.2b), leaving behind small, irregularly shaped terraces which are one half unit cell in height. As these terraces

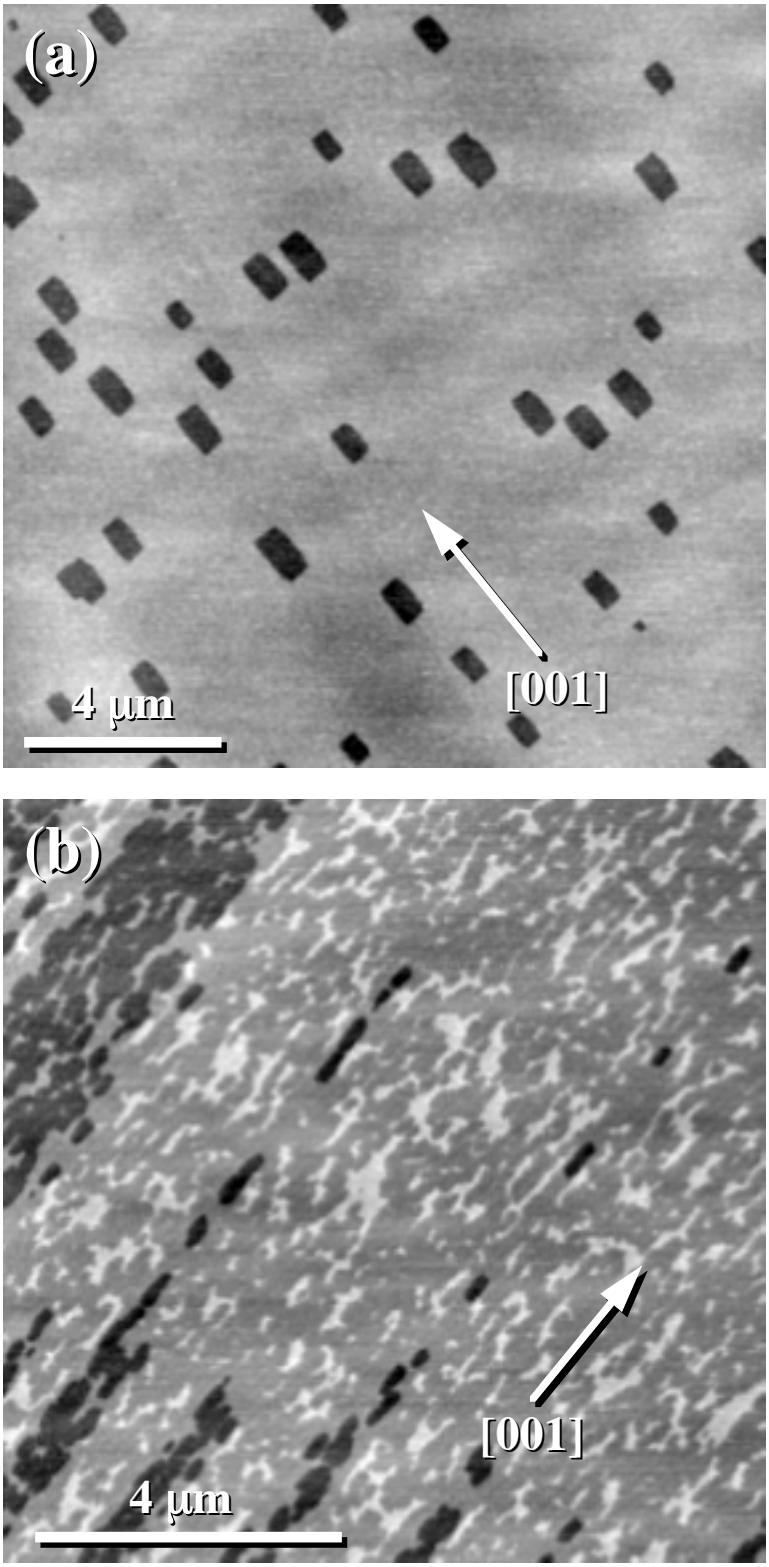

Figure 8.2. AFM topographs of MoO_3(010) surfaces reacted with air-MeOH at 300 ˚C. The surface in (a) was reacted with air saturated with MeOH at 25˚C for 2 h and has a step edge density of 4.75 x 10^3/cm. The surface in (b) was reacted for 1 h in air saturated with MeOH at 0 ˚C and has a step edge density of 4.6 x 10^4/cm. The black-to-white contrast in the images is 40 Å. The residual morphology of the cleavage terraces is evident in (b) by the well defined regions of pits along <001>.

disappear, new pits nucleate in the next layer. For O_2 rich conditions in which the air:N_2 ratio was greater than 60:40, the differences between the sizes and density of the pits were not noticeably correlated to small differences in the length of the reaction or the exact MeOH content of the feed. For this reason, it appears that we are observing a dynamic process, interrupted at various stages.

The pitting process was observed in all of the air-N_2-MeOH mixtures tested with air:N_2 ratios between 100:0 and 02:98. However, the shapes of the pits and their evolution depended on the amount of air in the mixture. Under oxygen rich conditions, the pits had a rectangular or ovular shape, were always elongated along <001>, and only one or two {010} surface layers were exposed at any given time. As the mixture approached the 50:50 concentration, the pits become more equiaxed and are often shaped like a "D" (see Fig. 8.3). With still lower air concentrations, the pits elongate along <100> and assume a triangular habit. For example, the surface in Fig. 8.4a was reacted for 1 h at 300 °C in a 20:80 mixture saturated with MeOH at 0 ˚C. The roughly triangular pits have their long axis oriented along <100>. As the air concentration is further decreased, the edges of the triangular pits become straighter and the tips of the triangles become more pointed. The AFM image in Fig. 8.4b is of a surface reacted for 1 h at 300 °C in a 10:90 mixture saturated with MeOH at 0˚C. On any given layer, all of the triangular pits are oriented in the same way, with the triangle pointing toward the [100] or [$\bar{1}$00] direction. However, this orientation is reversed as the pits form in the next layer.

A second difference between the higher and lower O_2 feeds is that in the lower O_2 feeds, pits form and grow simultaneously on more than one surface layer. For example, it is not uncommon to observe pits forming in 4 or more layers, while only two are affected under the O_2 rich (air:N_2 > 50:50) conditions. This effect can also be seen by increasing the MeOH concentration while maintaining a constant air:N_2 ratio. For example, the surfaces in Fig. 8.5a and b were reacted for 2 h at 300 ˚C in 30:70 (a) and 10:90 (b) mixtures saturated with MeOH at room temperature. Comparison of Fig. 8.5b with Fig. 8.4b shows that more layers are affected and higher step edge densities (note the difference in the lateral scale) are realized when the MeOH to air ratio is higher. Surfaces reacted in 02:98 (air:N_2) mixtures saturated with MeOH at room temperature are roughened to the extent that individual steps are difficult to resolve with AFM. When air is completely eliminated from the feed, H_xMoO_3 precipitates form as described in Chapter 6 [10].

At lower oxygen concentrations, the single crystals sometimes begin to change color during the treatment. In particular, traces of blue are observed near {001} faces after approximately 2 h at 300 °C. This color is similar to that observed when H_xMoO_3

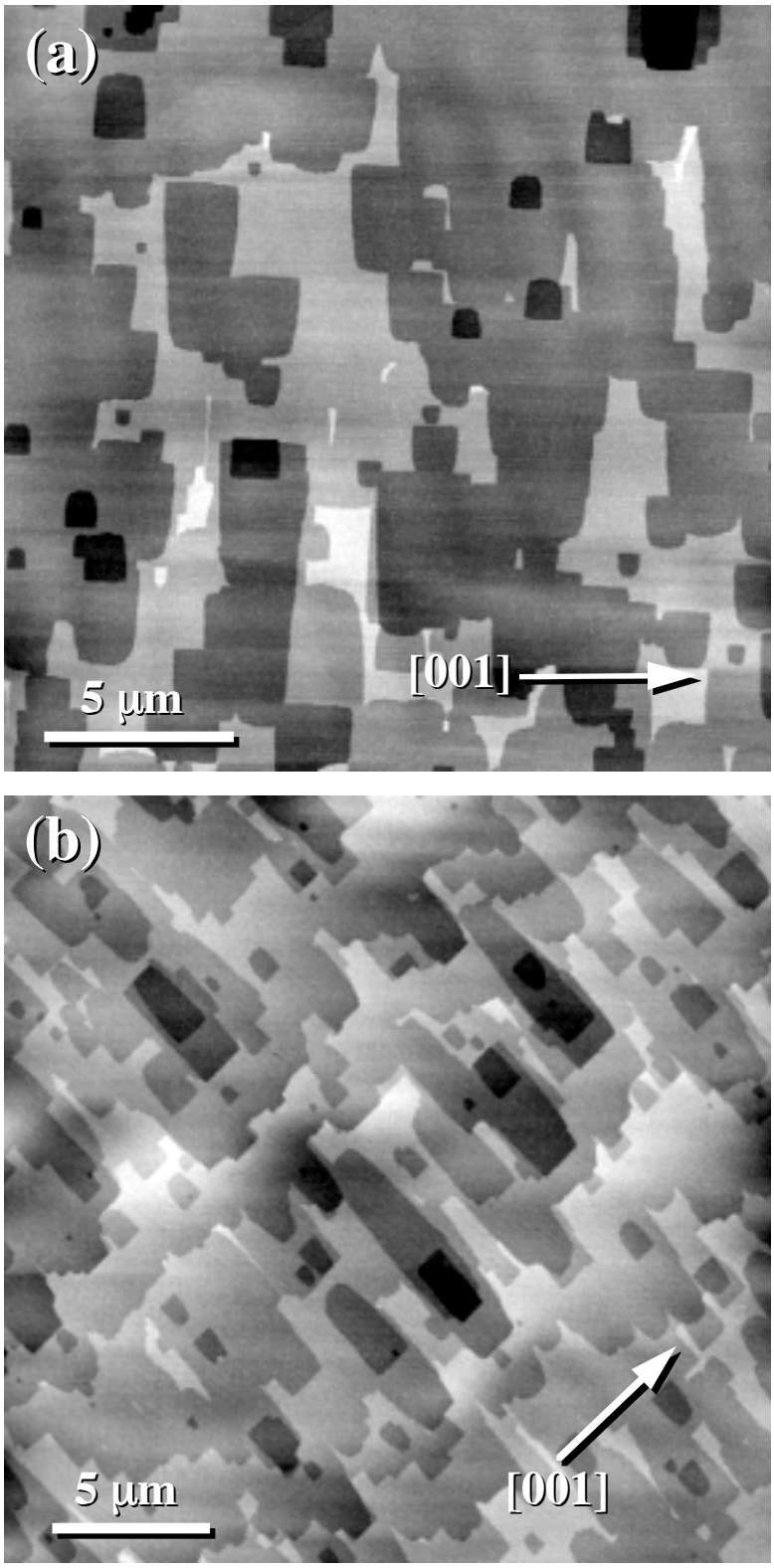

Figure 8.3. AFM topographs of a MoO_3(010) surface reacted for 2 h at 300 ˚C with a 50:50 air:N_2 mixture saturated with MeOH at 25 ˚C. The calculated step edge density in (a) and (b) is 7.70 x 10^3/cm and 1.04 x 10^4/cm, respectively. In (b) there is evidence of <001> step edges from the initial cleavage process. The black-to-white contrast in (a) and (b) is 40 and 60 Å, respectively.

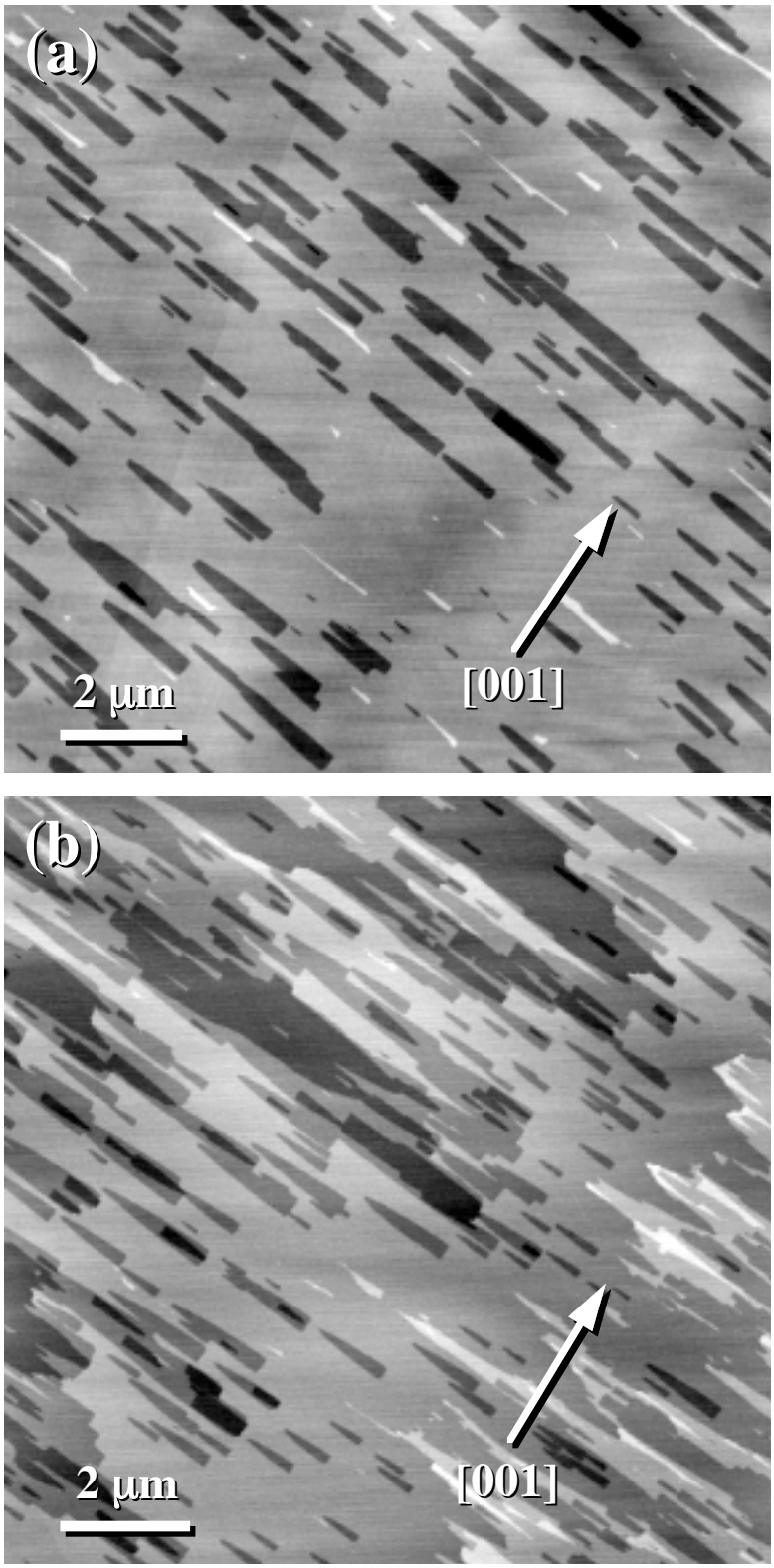

Figure 8.4. AFM topographs of MoO_3(010) surfaces reacted for 3 h at 300 ˚C in 20:80 (a) and 10:90 (b) air:N_2 mixtures saturated with MeOH at 0 ˚C. The calculated step edge densities in (a) and (b) are 2.14 x 10^4/cm and 3.52 x 10^4/cm, respectively. The black-to-white contrast is 35 Å (a) 50 Å (b).

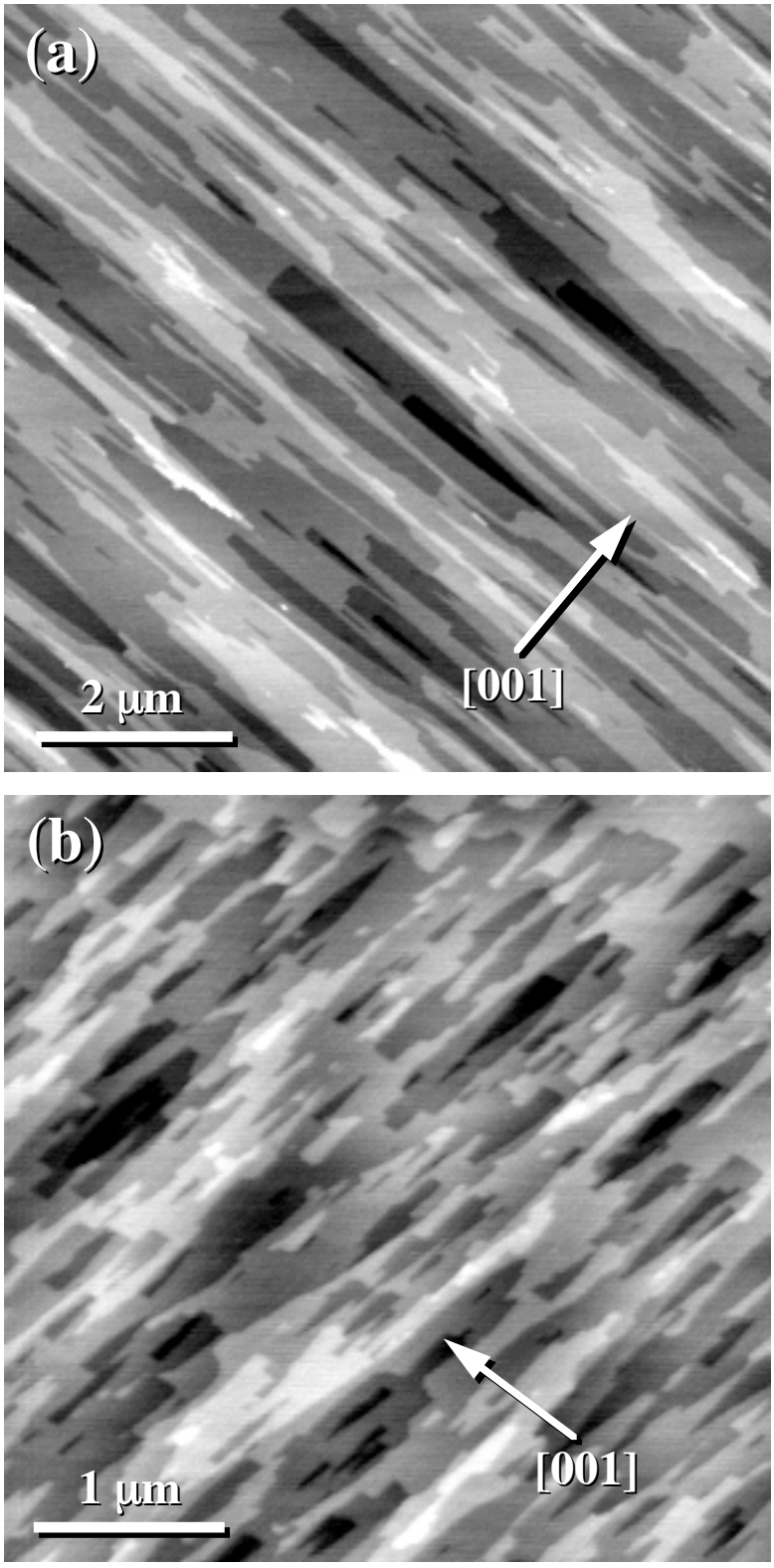

Figure 8.5. AFM topographs of MoO_3(010) surfaces reacted for 2 h at 300 ˚C in 30:70 (a) and 10:90 (b) air:N_2 mixtures saturated with MeOH at 25 ˚C. The calculated step edge densities in (a) and (b) are 6.10 x 10^4/cm and 1.51 x 10^5/cm, respectively. The black-to-white contrast in the images is 50 Å.

precipitates form in crystals treated in MeOH saturated N_2 without oxygen. However, based on AFM analysis of the blue regions, there is no evidence for the formation of H_xMoO_3 as long as some O_2 remains in the feed. Therefore, we assume that the color change is associated with the formation of isolated point defects.

In some regions of the crystal, the pitting process is greatly accelerated. Within 3 h of reaction at 300 ˚C in any of the air-N_2-MeOH mixtures, large, isolated etch pits can easily be seen with the aid of an optical microscope. These pits generally have the same habit as the shallow 7 Å pits, but the spiraling structure of the steps around them leads us to believe that they are dislocation etch pits. The fact that they form in the equivalent surface regions on two halves of the same cleaved crystal also supports the conclusion that they are associated with extended defects. Because the dislocation etch pit density was inhomogeneous and varied from crystal to crystal, it is difficult to quantify. However, measurements of cleaved CVT crystals yielded an average value of 1.5 x $10^4/cm^2$. The etch pits continually enlarged with extended reaction times. After 3 h in 100:0 mixtures, the pits are approximately 200 nm deep and equiaxed with edge lengths of 6 μm. In air lean conditions, the pits are up to 80 nm deep and rectangular in shape with edges that are 5 μm x 1 μm.

Several experiments were conducted to test the effect of temperature on the process and to see if pitting can be initiated without MeOH. While shallow pits still formed on MoO_3(010) surfaces reacted in air-N_2-MeOH mixtures at 250 ˚C, pits were not observed after comparable treatments at 200 ˚C for 3 h. When MeOH is eliminated from the feed and the MoO_3(010) surfaces are reacted in an air-N_2 mixture between 200 and 300 ˚C, the surface structure is not modified in any manner detectable with AFM. Surfaces reacted with dry or water saturated air, N_2, and air-N_2 mixtures for as long as 6 h could not be distinguished from virgin surfaces. Therefore, below 300 °C, the pitting process is connected to the reaction with methanol. Finally, we note that when subjected to the same reaction conditions, the growth surfaces of sublimed crystals and the cleavage surfaces of CVT grown samples evolved in an identical manner.

8.3.3 Weight Loss during MeOH Oxidation

The observations reported above indicate that the MoO_3(010) surface is eroding or decomposing in an almost layer-by-layer fashion during reactions with air-N_2-MeOH mixtures. There are two possible limiting cases for the fate of the MoO_3 removed from the surface during the nucleation and growth of the surface pits: it might volatilize and be carried away in the flowing gas or it may be transported to other regions (perhaps the side

facets) of the crystal. These two scenarios are easy to distinguish. In the first case, the sample loses mass and in the second case, the mass will remain constant.

Simple observations favor the first interpretation. After many crystals were reacted in the air-N_2-MeOH mixture for 3 h, a blue film accumulated on the thermocouple sheath and the relatively cool walls of the reaction tube where the gas exits the furnace. Because we estimated that the mass lost from any given crystal in a reasonable amount of time was negligible, we conducted a number of experiments on powder samples. In a typical experiment, powdered samples reacted with air saturated with MeOH at room temperature experienced a weight loss of approximately 20% over a 15 h period at 300 ˚C. For example, a 0.0367 g sample reacted in a 100 cc/min flow of air-MeOH at 300 ˚C for 16.1 h weighed 0.0076 g less at the conclusion of the treatment. Although the powder changed from yellow-white to light green-blue during the reaction, X-ray diffraction confirmed that the samples were phase pure MoO_3. While the color change probably indicates a small amount of reduction during the experiment, the weight loss associated with the formation of isolated oxygen vacancies can not account for a significant fraction of the lost mass.

The blue film at the reactor exhaust accumulated more rapidly during the experiments on powders than during the experiments on single crystals. In one case, the film was collected and analyzed with scanning electron microscopy, energy dispersive X-ray (EDX) analysis, and X-ray diffraction (XRD). The deposit was composed of plate-like particles which had dimensions ranging from less than 1 μm up to 5 μm. EDX analysis revealed only Mo and O in the deposit. Powder XRD patterns had peaks with d-spacings (in Å) of 7.41, 4.76, 3.85, 3.78, 3.22, 3.11, 2.31, and 1.85. The peak at 7.41 Å was intense and well developed while all the others had relative intensities of less than 15%. Inspection of all the available XRD patterns of Mo-O phases in the JCPDS-ICDD file revealed that the deposit was $Mo_2O_5(OCH_3)_2$ [14]. When exposed to UV light, heat, or X-ray radiation, this phase is known to decompose to yield formaldehyde and a blue amorphous hydrogen bronze; one of our samples, exposed to the laboratory ambient for several days, was found to be X-ray amorphous.

Gravimetry experiments at lower air concentrations gave mass losses which were comparable to those experienced in the air-MeOH mixtures at 300 ˚C. However, for mixtures with air:N_2 ratios less than 50:50, the interpretation is complicated by the fact that the powder is not phase pure at the conclusion of the reaction. The XRD patterns from samples treated in 50:50 and 30:70 mixtures each included peaks characteristic of MoO_2. Based on the relative intensities, the amount of material transformed to MoO_2 in the 30:70 sample was greater than in the 50:50 sample. However, even if the entire

sample were reduced to MoO_2 during the treatment, the mass would decrease only by 11%, approximately half of the total mass lost. Therefore, some portion of the mass loss must still be due to the volatilization process. Finally, control experiments, conducted with dry and water saturated air-N_2 mixtures without MeOH, displayed no detectable mass losses over periods as long as 48 h at 300 ˚C.

8.4 Discussion

The results of these AFM and weight loss experiments clearly demonstrate that during the partial oxidation of MeOH, volatilization leads to changes in the morphology of the MoO_3(010) surface. For MeOH containing air:N_2 mixtures with ratios between 100:0 and 02:98, 7 Å deep pits nucleate and grow on the (010) surface such that it evaporates in an almost layer-by-layer fashion. At high oxygen partial pressures, only the first one or two {010} layers of the structure appear to be affected, while at lower oxygen pressures, more than five surface layers may be exposed simultaneously. The types of sites exposed along the edges of the pits are influenced by the composition of the gas phase. In O_2 rich environments, the steps are generally oriented along <001>, while in lower oxygen partial pressures, step edge orientations closer to <100> are favored. As a result of this process, new undercoordinated surface Mo sites, which would not be found on an ideally flat (010) surface, are continuously created during the oxidation reaction.

The volatility of MoO_3 is enhanced by the presence of atmospheric water impurities and the process is linked to the formation and evaporation of volatile oxide-hydroxides, such as $MoO_2(OH)_2$ (g) [15,16]. Above 400 °C, MoO_3 is known to volatilize in both oxidizing and reducing atmospheres containing water vapor [12]. The results presented here demonstrate that at temperatures of 300 ˚C or less, volatilization does not occur at any measurable rate, even in flowing gases saturated with H_2O. However, when MeOH is added to the gas stream in this same temperature range, MoO_3 volatilizes and a Mo oxide-methoxide, $Mo_2O_5(OCH_3)_2$, is deposited in the cooler exhaust region of the reaction tube.

Based on the generally accepted mechanism of MeOH oxidation on MoO_3, we can propose two possible evaporation pathways [5]. The first step of the oxidation reaction is the dissociative chemisorption of MeOH which results in the formation of a surface methoxy and a surface hydroxyl. At this point, if a molybdenum oxide-hydroxide molecule desorbs, then the volatilization process is similar to what occurs at higher temperatures in the presence of water vapor. However, in this case, the hydrogen for the process comes from the MeOH rather than from water. The Mo oxide-hydroxide might

then react with gas phase MeOH during transport or after condensation to form the observed $Mo_2O_5(OCH_3)_2$ deposit at the reactor exhaust. A second and perhaps more plausible explanation is that the surface methoxides which form during the dissociative chemisorption are capable of desorbing as molybdenum oxide-methoxide molecules, which then condense to form crystalline $Mo_2O_5(OCH_3)_2$ at the reactor exhaust. In either case, the desorption of the volatile molecule leads to the loss of Mo and O from the crystal and results in the growth of surface pits. While both mechanisms are viable, our results do not allow us to distinguish between them. Finally, it should be noted that our weight loss data represent the minimum quantity of material that evaporated; any material which recondensed within the powder bed does not contribute to the total weight loss.

It is believed that MeOH chemisorption occurs at undercoordinated surface Mo sites, which occur at surface oxygen vacancies, step edges on the basal surface, and on lateral {h0l}-type facets of the crystal [4-6]. It is tempting to speculate that the pits initially nucleate at or very near undercoordinated Mo sites. The observation that more surface layers are affected in lower oxygen partial pressures supports the idea that the pits nucleate at oxygen vacancies on the (010) surface. As the partial pressure of O_2 is reduced, the vacancy concentration should increase, allowing more pits to be created. Once a pit is nucleated, it is then free to grow outward since the edges provide additional undercoordinated Mo sites which are active for chemisorption. One interesting aspect of our observations is that they show that the active sites on this surface are not static. As each pit grows and more material is removed, fresh sites, free of reactor contaminants (such as H_2O), are revealed.

Existing data on the structure sensitivity of MeOH oxidation by MoO_3 are contradictory. Tatibouët and Germain [1] reported that the {010} facets had a high activity and selectivity for formaldehyde, while Farneth and coworkers [4,5] have shown that at low temperatures, the MoO_3(010) surface chemisorbs very little MeOH. The second result was explained using the idea that the absorption sites are undercoordinated surface Mo and that while these sites occur abundantly on {h0l} surfaces, they can only be found at step edges and oxygen vacancies on the (010) surface. In part, our results are consistent with this explanation. The density of sites on a fresh (010) surface is initially very low (approximately 10^3/cm) and we do not expect a significant number of new sites to be generated during a few TPD cycles. On the other hand, our results also show that for longer experiments approaching a steady state, many new sites can be generated on the basal plane and the density of these sites depends on the experimental conditions. Therefore, it is interesting to consider the conditions under which the population of

unsaturated Mo sites at the step edges on the basal facets might rival the population of similar sites on the lateral facets of the crystal.

To estimate the relative importance of these new sites, we can consider the MoO_3 catalyst which Tatibouët and Germain [1] found to be most selective for formaldehyde formation. The sample they designated "S_4" had average dimensions of W = 0.045 cm, L = 0.214 cm, and t = 0.004 cm, where W is the width along <100>, L is the length along <001>, and t is the thickness along <010> [1]. If we assume that the lateral {h0l} faces are composed of stacks of steps, each with a half unit height of b/2 = 6.93 x 10^{-8} cm, then the total linear density of step edges associated with the lateral facets, per unit area of the basal face, $\rho_{\{h0l\}}$, can be calculated as the total length of the steps divided by the area of the basal plane.

$$\rho_{\{h0l\}} = \frac{2t(L + W)}{bLW} \qquad (1)$$

Therefore, the linear density of step edges associated with the side facets on the particles used by Tatibouët and Germain [1] was 1.5 x 10^6/cm.

For comparison, we can consider the linear density of sites associated with the basal facets, $\rho_{\{010\}}$. For an as-grown crystal, such as the one shown in Fig. 8.1, $\rho_{\{010\}}$ is only 2.6 x 10^3/cm. This is less than 1% of $\rho_{\{h0l\}}$ and, therefore, we expect the properties of the particles to be dominated by the lateral facets. However, as the reaction progresses, there are two new observed sources of sites active for chemisorption: those associated with the step loops and those associated with the dislocation etch pits. The image in Fig. 8.2b illustrates that after extended reaction times in the air-MeOH mixtures, the contribution to $\rho_{\{010\}}$ from step loops can be as high as 4.6 x 10^4/cm or approximately 3% of $\rho_{\{h0l\}}$. The contribution from the etch pits increases with time (the pits grow continuously) and depends on the dislocation density. Our observations indicate that a typical density is 1.5 x 10^4/cm^2, so that for a square etch pit with a 6 μm edge length and a depth of 200 nm that forms in 3 h, the contribution to $\rho_{\{010\}}$ is 1.5 x 10^4/cm. Therefore, under air-rich conditions, the total value of $\rho_{\{010\}}$ is approximately 4% of $\rho_{\{h0l\}}$.

On the basis of these estimates, it does not appear that the high reactivity of Tatibouët and Germain's [1] plate-like particles can be explained by the presence of new edge sites forming on the basal plane. However, we should allow the possibility that an isolated step on the (010) surface might be different from a site on a lateral facet of the crystal in its geometric configuration, energy, and selectivity for specific products. This

idea could be tested by using experimental conditions where the ratio of $\rho_{\{010\}}/\rho_{\{h0l\}} \geq 1$. For example, it is possible to increase the linear density of step edges either by reducing the concentration of air in the feed, increasing the depth of the pits by higher temperature treatments [12], or by increasing the aspect ratio of the particles. Increasing $\rho_{\{010\}}$ or decreasing $\rho_{\{h0l\}}$ by a factor of 10 will make the two quantities comparable. By comparing the reactivity of particles with similar values of $\rho_{\{h0l\}}$ but different values of $\rho_{\{010\}}$, it will be possible to determine whether or not the sites on the basal plane behave differently from those on the lateral edges.

As a final note, it should be pointed out that since the $\rho_{\{010\}}/\rho_{\{h0l\}}$ ratio depends on the details of the experiment (time, temperature, gas composition), the results from previous studies of the structure sensitivity of reactions on MoO_3 should be applied with caution. In particular, conclusions from experiments of extremely short duration are not expected to hold universally and those based wholly on the macroscopic form of the crystal might not accurately depict the density of active sites.

8.5 Summary and Conclusions

Atomic force microscopy (AFM) has been used to characterize the evolution of MoO_3(010) growth and cleavage surfaces during reactions with air-N_2-MeOH mixtures between 200 ˚C and 300 ˚C. At reaction temperatures greater than 250 °C, closed step loops, bounded by undercoordinated surface Mo sites, nucleate and grow as the (010) surface volatilizes in a nearly layer-by-layer fashion. The density and crystallography of the new surface sites depend on the composition of the gas mixture in the reactor. In air rich environments, the step loops have a rectangular shape and are elongated along the <001> direction. At any instant, only the top-most one or two {010} layers are affected by the process. As the concentration of O_2 in the feed is reduced, the shape evolves to elongated triangles oriented along <100> and the loops exist on multiple layers simultaneously. During reactions, the observed linear step edge densities can increase from 1 x 10^3/cm to greater than 1.5 x 10^5/cm.

8.6 References

[1.] J.M. Tatibouët and J.E. Germain, *J. of Catal.* **72** (1981) 375.

[2.] C.J. Machiels and A.W. Sleight, *in* "Proceedings of the 4th International Conference on the Chemistry and Uses of Molybdenum" (H.F. Barry and P.C.H. Mitchell, Eds.), p. 411, Climax Molybdenum Co., Ann Arbor, MI, 1982.

[3.] C.J. Machiels and A.W. Sleight, *J. of Catal.* **76** (1982) 238.

[4.] W.E. Farneth, F. Ohuchi, R.H. Staley, U. Chowdhry, and A.W. Sleight, *J. Phys. Chem.* **89** (1985) 2493.

[5.] W.E. Farneth, R.H. Staley, and A.W. Sleight, *J. Am. Chem. Soc.* **108** (1986) 2327.

[6.] J.S. Chung, R. Miranda, and C.O. Bennett, *J. of Catal.* **114** (1988) 398.

[7.] R. Mars and D.W. van Krevelen, *Chem. Eng. Sci.* **3** (1954) 41.

[8.] P. Vergnon and J.M. Tatibouët, *Bull. Soc. Chim. Fr.* **11-12** (1980) 455.

[9.] J. Guidot and J.E. Germain, *React. Kinet. Catal. Lett.* **15** (1980) 389.

[10.] R.L. Smith and G.S. Rohrer, *J. of Catal.* **173** (1998) 219.

[11.] K. Bruckman, R. Grabowski, J. Haber, A. Mazurkiewicz, J. Sloczynski, and T. Wiltowski, *J. of Catal.* **104** (1987) 71.

[12.] R.L. Smith and G.S. Rohrer, *J. of Catal.* **163** (1996) 12.

[13.] R.L. Smith and G.S. Rohrer, *J. Solid State Chem.* **124** (1996) 104.

[14.] E.M. McCarron III, R.H. Staley, and A.W. Sleight, *Inorg. Chem.* **23** (1984) 1043.

[15.] T. Millner and J. Neugebauer, *Nature* **163** (1949) 601.

[16.] G.R. Belton and A.S. Jordan, *J. Phys. Chem.* **69** (1965) 2065.

9

Summary, Conclusions, and Future Work

9.1 MoO_3(010) Surface Structure during Redox Reactions

The research in this thesis has led to a description of how the MoO_3(010) surface is modified during redox reactions. Interestingly, the structural evolution during reduction depends on the reducing agent. The schematic diagram in Fig. 9.1 summarizes the limiting conditions under which modifications are introduced to the MoO_3(010) surface during reduction and oxidation reactions at 400 ˚C. Below ~ 350 ˚C, the surface structure is not modified in any manner detectable with AFM. The schematic diagram in Fig. 9.2 describes the morphology and structure of the MoO_3(010) surface and the phase composition of bulk MoO_3 powders during reactions with air-N_2-MeOH mixtures at ~ 300 ˚C.

9.2 Conclusions

Molybdenum Oxides cleave at their longest weakest bonds. The termination of the cleavage surfaces of anisotropically bonded molybdates can be determined by assuming that cleavage occurs at the longest, weakest bonds of the structure [1,2]. The contrast in atomic resolution SPM images of the molybdate surfaces studied could be interpreted based solely on the arrangement of surface polyhedra that was expected to result from cleavage of the longest, weakest bonds normal to the surface. This conclusion also applies to vanadates [3,4] and probably to anisotropically bonded transition metal oxides in general.

MoO_3(010) surface morphology is determined by H_2O and strain during reduction and oxidation reactions. Water vapor and strain are prerequisites for the volatilization of MoO_3 at temperatures above 350 ˚C. The distribution of defects (with associated strain fields) at the (010) surface determines the surface morphology which results from this process during redox reactions. Under oxidizing conditions, strain and volatilization are localized at surface steps and dislocation/surface intersections. Under reducing

conditions, the CS planes which form to accommodate nonstoichiometry introduce strain and lead to pitting of the (010) surface. This process can be controlled and used to produce {010} surfaces with distinct morphologies and site populations [5,6].

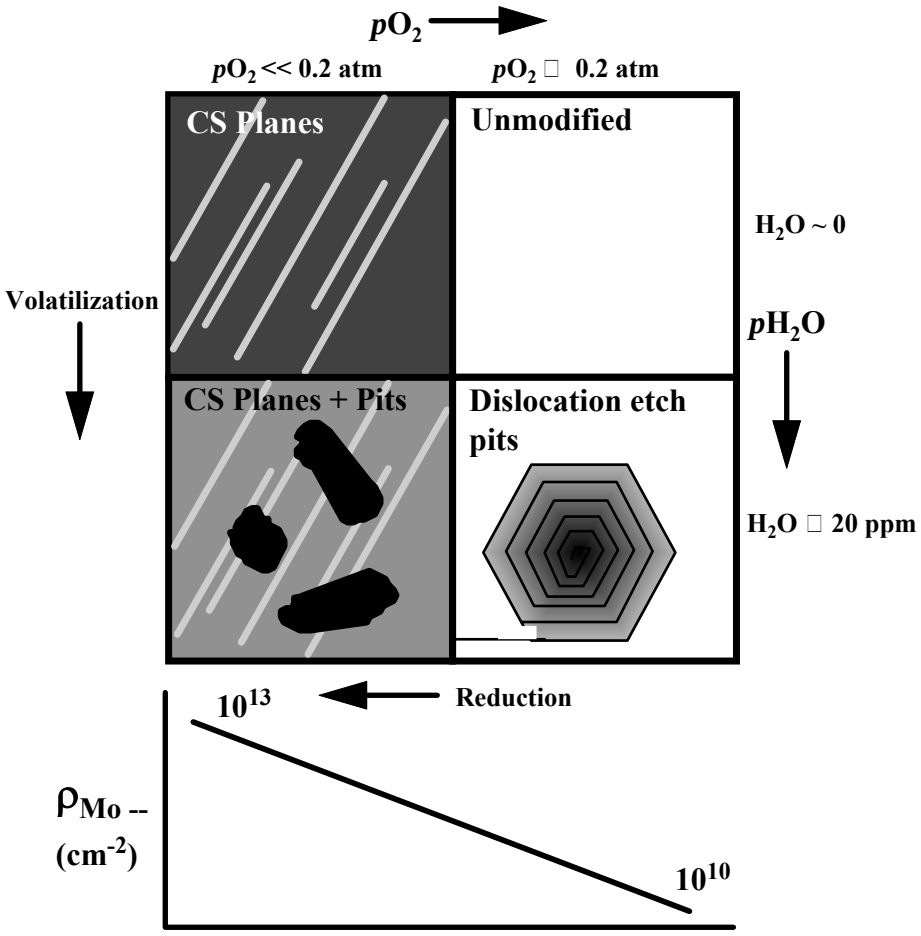

Figure 9.1 (top) The limiting conditions under which structural modifications are introduced to the MoO_3(010) surface during the early stages of reduction (t < 30 min) and oxidation (t < 3 h) reactions at 400 ˚C. Low partial pressures of O_2 lead to reduction and the formation of crystallographic shear (CS) planes. Water vapor catalyzes volatilization where strain is concentrated at the surface and this process leads to changes in the morphology of the (010) surface. Below 350 ˚C, the (010) surface was not modified in any manner detectable with AFM. (bottom) Schematic representation of the density of undercoordinated surface Mo sites, ρ_{Mo--}, introduced during redox reactions in the presence of H_2O. It has been assumed that there is a linear relationship.

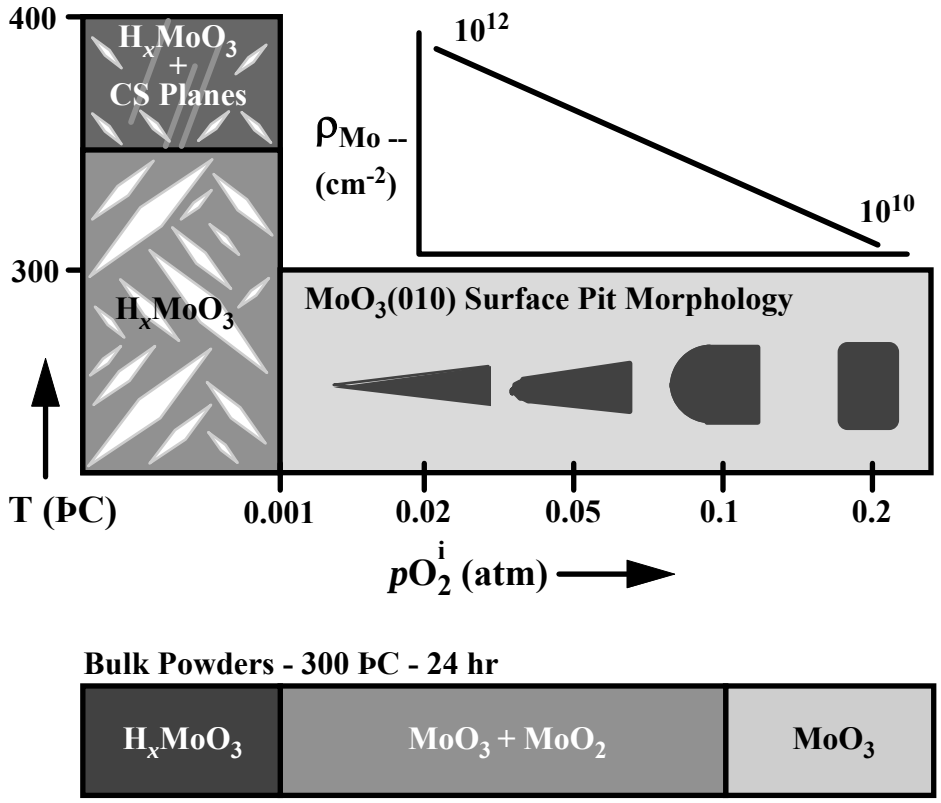

Figure 9.2 (top) The structure of the MoO_3(010) surface during reactions with air-N_2-MeOH mixtures. In this diagram, the modifications introduced to the MoO_3(010) surface within the first 3 hours of reactions with MeOH are depicted as a function of the temperature and the initial pO_2 of the feed mixture. This diagram applies to reactions at atmospheric pressure with pMeOH ≈ 0.04 atm and pN_2 (atm) ≈ 1 - pO_2 - pMeOH. At oxygen partial pressures less than approximately $1x10^{-3}$ atm, H_xMoO_3 forms at the (010) surface. At higher oxygen pressures, surface morphology is altered by the continuous nucleation and growth of 7 Å deep pits as the surface volatilizes in a nearly layer-by-layer fashion. The density and morphology of these pits depend on the oxygen partial pressure. The density of undercoordinated surface Mo sites, ρ_{Mo--}, introduced to (010) as a result of surface volatilization is shown schematically above the pit morphologies. It has been assumed that there is a linear relationship. (bottom) Phase composition of bulk MoO_3 powders which have been reacted with MeOH for 24 h at 300 ˚C with different air-N_2-MeOH mixtures.

MoO_3 protonates during reactions with alcohols ($300 \leq T \leq 400$ ˚C). During reactions with alcohols, MoO_3 intercalates H liberated from the alcohol during dissociative chemisorption. Protonation leads to the nucleation and growth of acicular H_xMoO_3 ($0.23 \leq x \leq 0.40$) precipitates at the (010) surface [7]. Identical precipitates form during reactions with atomic H at lower reaction temperatures ($T \leq 200$ ˚C).

MoO_3{h0l} facets dominate MeOH chemisorption at 300 ˚C. H_xMoO_3 precipitation and MeOH chemisorption during reactions with MeOH are favored at the undercoordinated surface Mo sites exposed on nonbasal facets. This result had previously been reported for room temperature reactions with MeOH [8,9]. In Chapter 7, it was demonstrated that these sites are also active at typical reactor temperatures. Basal surfaces with large populations of {h0l} sites intercalate more H than relatively flat cleavage surfaces and H_xMoO_3 precipitation is favored at {h0l} sites.

The morphology of the MoO_3(010) surface evolves during the partial oxidation of MeOH and is dependent on the reactor environment. At reactor temperatures greater than 250 ˚C, closed step loops, bounded by undercoordinated surface Mo sites, nucleate and grow as the (010) surface volatilizes in a nearly layer-by-layer fashion. The density and crystallography of these new sites depends on the composition of the gas mixture in the reactor. During this process, the observed linear step density on (010) can increase from 1×10^3/cm to greater than 1×10^5/cm. Because the concentration of undercoordinated sites is still small in comparison to what is found on the lateral edges of typical particulate catalysts, this process does not explain the observation that increasing the relative area of the {010} facets in a catalyst increases the yield of CH_2O.

9.3 Status of Structure-Reactivity Relationships for MoO_3

In this thesis, a reliable description of the structure of the MoO_3(010) surface which exists during the partial oxidation of MeOH has been developed. While this has not conclusively reconciled the discrepancies between previous TPD [8,9] and reactor [10] studies, we can confidently describe the density of undercoordinated surface Mo under a variety of conditions. In light of these results, we must now consider the possibility that a site on an isolated step on the (010) surface might be different from a site on a lateral facet of the crystal in its geometric configuration, energy, and selectivity for specific products. The possibility of testing these differences experimentally is addressed in the next section. The fact that the morphology of the MoO_3(010) surface is modified at reaction temperatures as low as 250 ˚C illustrates why it has been difficult to

establish structure-reactivity relationships based on gross particle shape or ideal models of bulk terminated surfaces.

9.4 Future Work

Clearly, more work will be necessary to establish structure-reactivity relationships for alcohol oxidation on MoO_3. My first recommendation is to measure conversions over MoO_3 particles with very different surface characteristics. For example, as discussed in 8.4, by testing samples with different $\rho_{\{010\}}/\rho_{\{h0l\}}$ ratios it will be possible to assess the relative selectivity and activity of sites on basal plane steps and lateral facets. Such model particles can be produced by sublimation ($\rho_{\{010\}}/\rho_{\{h0l\}} \approx 1$) and the oxidation of Mo foil ($\rho_{\{010\}}/\rho_{\{h0l\}} << 1$) [11]. An alternate way to address this same issue is with TPD spectroscopy studies on single crystal surfaces with different $\rho_{\{010\}}/\rho_{\{h0l\}}$ ratios. This can be done by performing TPD before and after crystals have been exposed to realistic reaction conditions (under which 7 Å pits form) or by introducing {h0l} sites to the {010} facets with thermal treatments, as discussed in Chapters 5 and 7.

My second recommendation is to determine the chemical identity of the vapor phase species responsible for volatilization during MeOH oxidation and to relate the rate of volatilization to the catalyst's activity. If the catalyst volatilizes as an oxide-methoxide, formaldehyde formation may not occur at the MoO_3 surface. Instead, it could be formed in the gas phase above the catalyst or during the condensation and decomposition of the Mo oxide-methoxide species. If the catalyst volatilizes as an oxide-hydroxide, such as $MoO_2(OH)_2$, oxidation could also occur homogeneously in the gas phase. If either of these processes are responsible for product formation, the reported structure sensitivity of MeOH oxidation on MoO_3 may depend on the rate at which different volatile species are formed at different crystalline facets rather than the static structure of these facets.

The techniques used in this study should be applicable to other transition metal oxide catalysts for which flat, single crystal surfaces can be prepared. Furthermore, other types of model catalysts can also be studied. Supported catalysts can be modeled by depositing the oxide on single crystal substrates. Model catalysts could also be prepared by conventional ceramic pellet processing. In this case, orientation imaging microscopy (OIM) could be used to determine the orientation of individual grains while SPM is used to study the evolution of the surfaces of the grains. Finally, measuring conversions over the same samples which are studied with SPM could prove to be the most efficient and

powerful way to establish the groundwork necessary for the development of surface structure-property relationships for partial oxidation catalysts.

9.5 References

[1.] G. S. Rohrer, W. Lu, R. L. Smith, A. Hutchinson, *Surf. Sci.* **292** (1993) 261.

[2.] R.L. Smith and G.S. Rohrer, *J. of Solid State Chem.* **124** (1996) 104.

[3.] R. L. Smith, W. Lu, G. S. Rohrer, *Surf. Sci.* **322** (1995) 293.

[4.] R.L. Smith, G.S. Rohrer, K.S. Lee, D.-K. Seo and M.-H. Whangbo, *Surf. Sci.* **367** (1996) 87.

[5.] R.L. Smith and G.S. Rohrer, *J.of Catal.* **163** (1996) 12.

[6.] R.L. Smith and G.S. Rohrer, *in* "Catalyst Materials for High Temperature Processes", edited by K.S. Ramesh, M. Misono, and P.L. Gai, Ceramic Transactions **73**, American Ceramic Society, Westerville, OH (1997) p. 139.

[7.] R.L. Smith and G.S. Rohrer, *J.of Catal.* **173** (1998) 219.

[8.] W.E. Farneth, F. Ohuchi, R.H. Staley, U. Chowdhry, and A.W. Sleight, *J. Phys. Chem.* **89** (1985) 2493.

[9.] W.E. Farneth, R.H. Staley, and A.W. Sleight, *J. Am. Chem. Soc.* **108** (1986) 2327.

[10.] J.M. Tatibouët and J.E. Germain, *J. of Catal.* **72** (1981) 375.

[11.] B. Mingot, N. Floquet, O. Bertrand, M. Treilleux, J.J. Heixmann, J. Massardier, and M. Abon, *J. Catal.* **118** (1989) 424.